

Combined Chemical–Electric Propulsion Design and Hybrid Trajectories for Stand-Alone Deep-Space CubeSats

Karthik Venkatesh Mani

Doctor of Philosophy Thesis



POLITECNICO DI MILANO

Dipartimento di Scienze e Tecnologie Aerospaziali



POLITECNICO DI MILANO
DEPARTMENT OF AEROSPACE SCIENCE AND TECHNOLOGY
DOCTORAL PROGRAMME IN AEROSPACE ENGINEERING

COMBINED CHEMICAL–ELECTRIC PROPULSION DESIGN
AND HYBRID TRAJECTORIES FOR STAND-ALONE
DEEP-SPACE CUBESATS

Doctoral Dissertation of:
Karthik Venkatesh Mani

Supervisor:
Prof. Francesco Topputo

Tutor:
Prof. Luciano Galfetti

The Chair of the Doctoral Program:
Prof. Pierangelo Masarati



POLITECNICO DI MILANO

Copyright © Department of Aerospace Science and Technology (DAER)
All rights reserved.

Abstract

Interplanetary CubeSats enable universities and small-spacecraft consortia to pursue low-cost, high-risk and high-gain Solar System exploration missions, especially Mars missions. Cost-effective, reliable, and flexible space systems need to be developed for CubeSats to embark on interplanetary missions. Primary propulsion systems become an integral part of interplanetary CubeSats since orbital manoeuvring and control become indispensable. CubeSat missions can be accomplished by a) in-situ deployment by a mother ship, and b) highly flexible stand-alone Cubesats on deep-space cruise. Stand-alone CubeSats have a high degree of flexibility and autonomy which widen the launch windows and introduce new paradigms in autonomous guidance, navigation and control.

The current work focuses on design and performance characterisation of combined chemical–electric propulsion systems that shall enable a stand-alone 16U CubeSat mission on hybrid high-thrust–low-thrust trajectories from Earth to Mars. The emphasis is on *combined* propulsion since they are two separate systems in the same spacecraft that are used in different mission phases. Hybrid transfer solutions that utilise chemical–electric propulsion achieve a balance between system mass and transfer time. The application case is the Mars Atmospheric Radiation Imaging Orbiter (MARIO), a 32 kg 16U CubeSat mission that shall demonstrate the capabilities to escape Earth, perform autonomous deep-space cruise, achieve ballistic capture, and be emplaced on an operational orbit about Mars.

Chemical propulsion design is based on the ΔV requirement of 445 m/s for Earth escape and Mars capture orbit stabilisation, thrust constraint of 3 N, and combined propulsion system mass constraint of 50% of the initial wet mass. The system utilises non-toxic green monopropellant, an Ammonium Dinitramide (ADN)-blend called FLP-106, to improve safety and performance over conventional propellants such as Hydrazine. The thruster operates at 2 MPa combustion pressure. The nozzle throat diameter is 0.75 mm, the expansion area ratio is 200 and an expansion half angle of 15° . Two thrusters are used and the total thrust yield is 3.072 N and the I_{sp} yield is 241.2 seconds. High-thrust trajectory analysis is performed to calculate the propellant consumption for the shortest time for Earth escape. The high-thrust trajectory is executed in multiple burns to raise the orbit and each thruster burn is split equally before and after the perigee. The overall flight time, including powered and ballistic flight, until reaching eccentricity $e = 1$ is ~ 33.03 days. The total propellant mass is 5.725 kg for the required ΔV . Four elliptical dome ended cylindrical tanks, with a total volume of 4640.4 cm³, are used to accommodate the propellant. The tanks are designed for a burst pressure of 3.9 MPa and a nominal feed pressure of 2.2 MPa. A pressuriser tank with a volume of 492 cm³ containing gaseous nitrogen at 28 MPa is designed to maintain the propellant tank pressure. The total feed system volume is 8U. The overall mass of the chemical propulsion system is 6.91 kg, which is 21.59% of the wet mass (32 kg).

Electric propulsion is utilised in executing low-thrust autonomous heliocentric transfer, achieving ballistic capture, and circularising the spacecraft trajectory to an operational orbit about Mars. The design is based on the requirements placed on maximum transfer time and maximum power consumption as well as the constraint on the combined propulsion system mass. A performance model of an iodine-propelled inductively coupled miniature radiofrequency ion thruster is implemented to calculate the variation of thrust, specific impulse and efficiency with input power. The thruster size is 2.5 cm. The initial mass flow rate is maintained at 48 $\mu\text{g/s}$ and the grids are maintained at 2000 V potential difference for ion acceleration. The maximum thrust yield is 1.492 mN and the maximum I_{sp} is 3168 seconds, considering the maximum input power of 67 W. The thrust and I_{sp} increase/decrease with increasing/decreasing input power, which in turn depends upon the Sun-spacecraft distance. A power constrained low-thrust trajectory optimisation utilising the thruster performance model is pursued to calculate the transfer time, ΔV and the required propellant mass for fuel-optimal and time-optimal transfers. Low-thrust circularization is then performed to complete the mission design and to size the system. For the time-optimal transfer, the total time of flight is 1250 days with a continuous thrusting period of 1186.83 days. The cumulative ΔV is 5.837 km/s. The total propellant mass amounts to 5.87 kg for a time-optimal heliocentric transfer and low-thrust circularization. A thermoplastic propellant tank with dimensions of 20 cm \times 10 cm \times 6.5 cm is used to store the propellant. Including the PPCU and the feed system, the overall volume amounts to 3U. The overall system mass is 6.57 kg, which is 20.53% of the launch mass.

Preliminary systems design of MARIO is presented to provide an overview of the mission and the context for the research. The system architecture and flight systems design that includes information on subsystems such as power, communications etc. are presented. The configuration of the MARIO spacecraft and the system budgets are also presented. Reflectarrays along with high-gain antennas are utilised to establish long-distance low-bandwidth X-band communication link with the Earth. Two deployable solar arrays with a drive mechanism are utilised for continuous power generation. The spacecraft uses a modified 16U structure with aluminium shielding. A customised VIS and IR range camera is used along with a high-capacity processor for observation and on-board processing.

Concurrent optimisation of low-thrust trajectory and electric thruster operations is performed to achieve comprehensive optimal solutions for heliocentric transfers. Thruster control parameters such as input grid voltage, mass flow rate, and RF coil power along with trajectory control parameters such as azimuth and elevation thrusting angles in spacecraft body centred frame are concurrently optimised to achieve transfers with minimum flight time. The definition of this framework paves the way for autonomous and responsive thruster operations along the trajectory for achieving efficient transfers without human intervention. This shall enable a comprehensive design of autonomous interplanetary CubeSats.

Combined chemical-electric propulsion could lead to a major paradigm shift in solar system exploration efforts using CubeSats at high science-to-investment ratio.

Sommario

I CubeSat interplanetari consentono alle università e ai consorzi di piccoli satelliti di compiere missioni di esplorazione del sistema solare a basso costo, ad alto rischio e ad alto impatto, in particolare verso Marte. Sistemi spaziali economici, affidabili e flessibili devono essere sviluppati affinché i CubeSat possano intraprendere missioni interplanetarie. I sistemi di propulsione primaria diventano parte integrante dei CubeSat interplanetari poiché sono indispensabili per le manovre e il controllo orbitale. Le missioni CubeSat possono essere caratterizzate (a) da un posizionamento in-situ effettuato da un satellite madre o (b) da CubeSat autonomi e altamente flessibili, in grado di compiere una crociera nello spazio profondo. Un alto grado di flessibilità e indipendenza permette ai CubeSat autonomi di allargare le finestre di lancio e introdurre nuovi paradigmi nella guida, navigazione e controllo autonomi.

Il presente lavoro si concentra sulla progettazione e la caratterizzazione delle prestazioni di sistemi di propulsione combinati chimico-elettrici per consentire missioni di CubeSat 16U autonomi su traiettorie ibride ad alta/bassa spinta, dalla Terra a Marte. L'enfasi è sulla *propulsione combinata*, che consiste in due sistemi separati nello stesso satellite, i quali vengono utilizzati in diverse fasi della missione. Le soluzioni di trasferimento ibrido che utilizzano la propulsione chimico-elettrica permettono un compromesso tra la massa del sistema e il tempo di trasferimento. Il caso di studio è la missione Mars Atmospheric Radiation Imaging Orbiter (MARIO), una missione che prevede l'impiego di un CubeSat di 16U da 32 kg, il quale deve essere in grado di sfuggire dalla Terra, eseguire una crociera autonoma nello spazio profondo, realizzare la cattura balistica ed essere collocato in un'orbita operativa attorno a Marte.

Il design della propulsione chimica si basa su un requisito di ΔV , corrispondente a 445 m/s, per sfuggire dalla Terra e stabilizzare l'orbita di cattura attorno a Marte, su un vincolo di spinta di 3 N e su un vincolo di massa del sistema di propulsione combinata del 50% della massa iniziale al lancio. Il sistema utilizza un monopropellente green non tossico, nello specifico, una miscela di ammonio dinitramide (ADN) denominata FLP-106, il quale è più sicuro e performante rispetto ad altri propellenti (e.g. idrazina). La pressione in camera di combustione del propulsore è di 2 MPa. Il diametro di gola dell'ugello è pari a 0.75 mm, il rapporto delle aree è pari a 200 ed il semi-angolo di espansione è pari a 15°. Vengono impiegati due propulsori in grado di fornire una spinta totale di 3.072 N ed un impulso specifico di 241.2 s. È stato eseguita un'analisi di traiettoria ad alta spinta per calcolare la quantità di propellente necessaria da garantire un fuga dalla Terra nel minor tempo possibile. La traiettoria ad alta spinta viene eseguita tramite manovre multiple per allargare l'orbita ed ogni manovra viene suddivisa in parti uguali prima e dopo il perigeo. Il tempo di volo totale, alimentato e balistico, fino al raggiungimento di un eccentricità $e = 1$ è pari a ~ 33.03 giorni. Per il ΔV richiesto, la massa di propellente necessaria è di 5.725 kg. Quattro serbatoi di forma cilindrica con estremità ellissoidali, per un volume totale di 4640.4 cm³, sono utilizzati per lo stoccaggio del propellente. I serbatoi sono progettati per resistere ad una pressione di scoppio di 3.9 MPa e ad una pressione di alimentazione nominale pari a 2.2 MPa. Per mantenere i serbatoi del propellente in pressione, è stato progettato un serbatoio pressurizzato, di volume pari a 492 cm³, contenente azoto gassoso inizialmente alla pressione di 28 MPa. La massa totale del sistema di propulsione chimica è 6.91 kg, corrispondente al 21.59% della massa iniziale al lancio (32 kg).

La propulsione elettrica viene utilizzata per eseguire il trasferimento eliocentrico autonomo a bassa spinta, per realizzare la cattura balistica e per la circolarizzazione della traiettoria del satellite in un'orbita operativa attorno a Marte. Il design si basa sui requisiti posti sul tempo di trasferimento massimo, sul massimo consumo di potenza e sul vincolo della massa del sistema di propulsione combinata. Inoltre, è stato implementato un modello di prestazioni di un propulsore ionico in miniatura, basato sullo iodio, attivato tramite radiofrequenza e accoppiato induttivamente. Tale modello è utilizzato per calcolare la variazione di spinta, l'impulso specifico e l'efficienza in funzione della potenza in ingresso. La dimensione caratteristica di tale propulsore è 2.5 cm. La portata massica è mantenuta a 48 $\mu\text{g/s}$, mentre, per garantire l'accelerazione degli ioni la differenza di potenziale delle griglie è mantenuta a 2000 V. Considerando il caso in cui viene fornita la potenza massima, pari a 67 W, la spinta massima è di 1.492 mN e il massimo I_{sp} è di 3168 s. La spinta e l' I_{sp} crescono/diminuiscono con la crescita/diminuzione della potenza fornita, la quale a sua volta dipende dalla distanza dal Sole. Un'ottimizzazione di traiettoria a bassa spinta, basata sul modello di prestazioni del propulsore e vincolata dalla potenza, è effettuata per calcolare il tempo di trasferimento, il ΔV e la massa di propellente richiesta per trasferimenti a tempo minimo e trasferimenti ottimi in termini di propellente. Viene quindi eseguita una circolarizzazione a bassa spinta della traiettoria per completare il design della missione e dimensionare il sistema. Considerando il caso di trasferimento a tempo minimo, il tempo totale di volo è 1250 giorni, incluso un periodo di spinta continua pari a 1186.83 giorni. Il ΔV cumulativo è pari a 5.837 km/s. Nel caso di trasferimento eliocentrico a tempo minimo e circolarizzazione a bassa spinta, la massa totale di propellente ammonta a 5.87 kg. Un serbatoio termoplastico di dimensione 20 cm \times 10 cm \times 6.5 cm viene utilizzato per lo stoccaggio del propellente. Includendo il PPCU e il sistema di alimentazione, il volume totale ammonta a 3U. La massa totale del sistema propulsivo elettrico è pari a 6.57 kg, corrispondente al 20.53% della massa iniziale al lancio.

Viene presentata la progettazione preliminare dei sistemi di MARIO per fornire una panoramica della missione e dello scopo della ricerca. Vengono presentate l'architettura del sistema e la progettazione dei sistemi di volo che includono informazioni sui sottosistemi quali quello elettrico, delle telecomunicazioni, ecc. Vengono inoltre presentati la configurazione di MARIO e i budget del sistema. Reticolari ed antenne ad alto guadagno sono utilizzate per stabilire una connessione con la Terra a lunga distanza e bassa banda nell'intervallo di frequenze X-band. Per la generazione continua della potenza vengono utilizzati due pannelli solari dispiegabili, equipaggiati con un meccanismo di rotazione. Il CubeSat utilizza una struttura 16U ad hoc e schermata in alluminio. È inoltre previsto l'utilizzo di una camera VIS & IR e di un processore ad alte prestazioni per l'osservazione e l'elaborazione di bordo.

L'ottimizzazione simultanea della traiettoria a bassa spinta con le operazioni del propulsore elettrico viene sfruttata per ottenere soluzioni ottimali dei trasferimenti eliocentrici. I parametri di controllo del propulsore, come il voltaggio della griglia, la portata massica e la potenza della bobina RF, insieme ai parametri di controllo della traiettoria, ovvero gli angoli di azimut e di altezza della spinta, sono contemporaneamente ottimizzati per ottenere trasferimenti con tempo di volo minimo. La definizione di questa metodologia apre la strada a operazioni autonome del sistema propulsivo lungo la traiettoria in modo da effettuare trasferimenti efficienti senza intervento umano. Ciò consentirà una progettazione completa di CubeSat interplanetari autonomi.

La propulsione chimico-elettrica combinata potrebbe portare ad un grande cambiamento di paradigma negli sforzi di esplorazione del sistema solare usando CubeSat ad alto rapporto fra ritorno scientifico e investimento.

Acknowledgement

ஈன்று பொழுதின் பெரிதுவக்கும் தன்மகனைச்
சான்றோன் எனக்கேட்ட தாய்

*The mother who hears her son called 'a wise man'
will rejoice more than she did at his birth*

- Thiruvalluvar, Classical Tamil Poet

I would like to thank my mother Mrs. Umamaheswari Mani and my father Dr. Manibharathi for their unconditional love and immeasurable faith that they have in me. Mom and Dad, I could have never been the person who I am now without you. There aren't enough words to thank you.

I would like to thank Prof. Francesco Topputo, my PhD advisor. He gave me the opportunity to come to Milan in 2016 as a researcher and believed in me to pursue a doctorate. I learned a lot from him. This entire research would not have been possible without his vision. He not only helped me grow as an independent researcher but also gave me wonderful insights to multiple problems and guided me whenever I had questions. His support has been insurmountable and I shall forever be grateful to him. I would also like to thank Prof. Angelo Cervone, with whom I have been associated since my days in TU Delft, for his contributions, support, encouragement and insight into this research work.

I would like to expressly thank Alvaro Sanz Casado, a brilliant guy with whom I teamed up to create the extremely ambitious stand-alone CubeSat mission - the Mars Atmospheric Radiation Imaging Orbiter (MARIO). His dedication and his contribution has been immensely helpful in cementing this whole mission and creating a vision for the future. In addition to this, I thank Vittorio Franzese, Jose Gutierrez, Gonçalo Aguiar, Fernando Soler Lanagrán, Jose Enrique Ruiz Sarrío and Stefano Boccelli for their help and contributions at various times of these research. I am indeed honoured to have worked with Alvaro, Vittorio, Fernando and Jose Enrique during their master thesis research. They are extremely ambitious, intelligent and diligent. They have contributed a lot to the building blocks of MARIO design. Without their support, this research on interplanetary CubeSats would have never materialised.

Speaking about friendships, over these years in Milan, I have formed some very strong and deep friendships with many wonderful people. I couldn't have done a good work without the support of my friends. I would like to acknowledge my friends at work Stefan, Ioannis, Mirko, Narcis, Myles, Rita, Carmine, Yang Wang (Ugo), Vincenzo and many others with whom life at Politecnico became immensely fun. I would like to thank my friends Paula, Elena, Sava,

Beata, Javi, Danilo, Praveen, Giulia, Dartta etc. for all the memorable moments that they gave me. Of course, the amazing people I met in Delft have stood by me all the way: Laura, Enrico, Marco, Andreas, Chris, Ajay, Chabely etc. I kindly ask for forgiveness if I had missed any names. I am confident that my friends know how much they mean to me.

A special thanks needs to be said to the people my favourite place to eat: Centoventicinque (125). Alesssandro and crew have the hands of an angel with which they have fed me some of the best pasta I have ever had over these years at Politecnico. Ale, ti ringrazio mille volte per i pizzoccheri e i paccheri. Ogni giorno mi hai dato la gioia di mangiare il tuo cibo e in modo indiretto hai contribuito alla mia ricerca di dottorato.

Contents

1	Introduction	1
1-1	Interplanetary CubeSat Missions	1
1-2	Need for Primary Propulsion	4
1-3	Motivation and objectives	5
1-4	MARIO application case definition	6
1-5	Research questions and hypotheses	8
1-5-1	Main research questions	8
1-5-2	Sub-questions based on chemical propulsion	9
1-5-3	Sub-questions based on electric propulsion	10
1-6	Structure of the document	10
2	Chemical propulsion	11
2-1	Chemical propulsion principles	11
2-2	CubeSat chemical propulsion system state-of-the-art	12
2-2-1	Cold gas	13
2-2-2	Solid rocket motors	14
2-2-3	Liquid monopropellant engines	15
2-2-4	Liquid bipropellant engines	18
2-3	System design strategy and trade-off	20
2-4	Propellant properties and analysis	24
2-4-1	ADN-blends vs HAN-blends	24
2-5	Thruster performance and design	26
2-6	High-thrust trajectory analysis	30
2-7	Feed system design and system sizing	32
3	Electric propulsion	37
3-1	Electric propulsion principles	37
3-1-1	Power constraint	41
3-2	CubeSat electric propulsion state-of-the-art	43
3-2-1	Gridded ion thrusters	45

3-2-2	Hall thrusters	48
3-2-3	Field emission electric propulsion	51
3-2-4	Pulsed plasma thrusters	53
3-2-5	Helicon thrusters	55
3-3	Multimode propulsion	56
3-4	Systems design strategy and trade-off	58
3-5	Propellant analysis	61
3-5-1	Xenon vs Iodine	61
3-6	Radiofrequency ion thruster principles and performance model	62
3-6-1	Plasma generation and acceleration	63
3-6-2	Performance	66
3-7	Low-thrust trajectory optimisation	70
3-7-1	Statement of the problem	70
3-7-2	Optimal control problem	72
3-7-3	Numerical scheme and solver	76
3-7-4	Heliocentric trajectory	77
3-7-5	Ballistic capture and circularization	78
3-8	Systems design and sizing	83
4	MARIO Systems Design	85
4-1	Systems architecture	86
4-2	Flight system design	87
4-2-1	Combined propulsion	87
4-2-2	Power	87
4-2-3	Communications	89
4-2-4	Other subsystems	92
4-3	Structure and system configuration	93
4-3-1	Mass Budget	96
5	Concurrent propulsion–trajectory optimisation	99
5-1	Thruster performance envelope	99
5-2	Statement of the problem	102
5-2-1	Spacecraft dynamics	102
5-2-2	Boundary conditions	104
5-2-3	Constraints and objective	104
5-3	Numerical simulation	105
6	Closure	109

6-1	Summary	109
6-2	Conclusion	111
6-2-1	On the combined chemical–electric propulsion design and hybrid trajectory	111
6-2-2	On the concurrent systems–trajectory design framework	113
6-2-3	Recommendations to spacecraft designers	115
6-3	Reflections of the author	116
	Glossary	119
	List of Acronyms	119
	List of Symbols	120
	Bibliography	123

List of Figures

1-1	CubeSat Missions beyond Low-Earth Orbit	3
1-2	Qualitative comparison of chemical, electric and combined propulsion systems for missions to Mars	6
1-3	MARIO Mission Phases	7
2-1	Cold gas systems state-of-the-art	14
2-2	Solid rocket motors state-of-the-art	16
2-3	Liquid monopropellant engines state-of-the-art	18
2-4	Bipropellant system state-of-the-art	19
2-5	Chemical propulsion system design strategy	20
2-6	Ideal and estimated thrust and specific impulse variation with area ratio	28
2-7	MARIO orbit raising and escape trajectory	32
2-8	Propellant tank shape and assembly	33
2-9	Schematic of the monopropellant thruster system	35
3-1	Propellant mass and power supply mass vs I_{sp}	42
3-2	Gridded Ion Thruster Schematic	46
3-3	Gridded ion thruster state-of-the-art	48
3-4	Hall Effect Thruster types	49
3-5	Hall effect thruster state-of-the-art	51
3-6	Field Emission Electric Propulsion concept	52
3-7	Field Emission Electric Propulsion state-of-the-art	53
3-8	Pulsed plasma thruster schematic	54
3-9	Pulsed Plasma Thruster state-of-the-art	55
3-10	Helicon plasma thruster schematic	56
3-11	Helicon plasma thruster state-of-the-art	57
3-12	Multimode space propulsion systems	57
3-13	Electric propulsion system design strategy	59
3-14	Power variation with the Sun-spacecraft distance for MARIO mission	60
3-15	Particle densities and electron temperature	67
3-16	Thrust, I_{sp} and efficiencies vs total power	69
3-17	Reference frames	72
3-18	Hypothetical low-thrust trajectory and ballistic capture	74
3-19	Spacecraft heliocentric trajectory for time-topimal and fuel-optimal solutions	78
3-20	Thrust and I_{sp} variations over time for time-optimal and fuel-optimal solutions of heliocentric transfer	79
3-21	Variation of state variables with time for time-optimal and fuel-optimal solutions	80
3-22	Circularization orbits after time-optimal and fuel-optimal heliocentric transfers	83
3-23	Schematic of the electric propulsion system	84
4-1	MARIO mission at Mars	85
4-2	MARIO system physical and functional architecture	86
4-3	MARIO electrical interface	90
4-4	Maximum data rate transmission as a function of distance and feed input power	92
4-5	MARIO internal configuration	95
4-6	MARIO external configuration w/o shielding	95
4-7	MARIO external configuration Detail	96

4-8	Relative contribution of different subsystems to MARIO CubeSat dry mass	97
5-1	Relationship between control parameters and performance	100
5-2	Thrust, I_{sp} and total power variations with grid voltage, mass flow rate, and RF power	101
5-3	Thrust and I_{sp} variation with mass flow rate and RF power for a single grid voltage	102
5-4	Thrust and I_{sp} vs P_{tot} at a specific V_{grid}	102
5-5	Concurrent thruster–trajectory optimisation	108
6-1	Overall combined chemical–electric propulsion system design strategy	114

List of Tables

1-1	MARIO Overall System Requirements	8
2-1	Summary of cold gas propulsion state-of-the-art	14
2-2	Summary of solid propulsion state-of-the-art	16
2-3	Summary of liquid monopropellant state-of-the-art	18
2-4	Chemical Propulsion System Requirements	21
2-5	Comparison of chemical propulsion systems	24
2-6	Green propellant comparison	25
2-7	Properties of FLP-106 and ideal performance prediction using NASA CEA	27
2-8	Estimated thruster performance for $\varepsilon = 200$ using NASA CEA	28
2-9	Monopropellant thruster design parameters	30
2-10	Mission parameters for orbit raising and escape	32
2-11	Monopropellant system design parameters	35
3-1	Summary of gridded ion thruster state-of-the-art	48
3-2	Summary of gridded ion thruster state-of-the-art	51
3-3	Summary of Field Emission Electric Propulsion state-of-the-art	53
3-4	Summary of Pulsed Plasma Thruster state-of-the-art	55
3-5	Electric propulsion requirements	58
3-6	Comparison of electric propulsion options	61
3-7	RF thruster performance model parameters	62
3-8	RF thruster performance at maximum power	68
3-9	Comparison of time-optimal and fuel-optimal heliocentric transfers	77
3-10	Parameters at Mars after ballistic capture	79
3-11	Circularization parameters after time-optimal and fuel-optimal heliocentric transfers	83
3-12	Electric propulsion design parameters	84
4-1	Combined propulsion characteristics	87
4-2	Power system requirements	88
4-3	MARIO subsystems power consumption	88
4-4	MARIO power operational modes	89
4-5	Communications system requirements	90
4-6	HGA link budget from 1.5AU	91
4-7	Overall system characteristics	94
4-8	Mass Budget of MARIO including unit and system margins	97

Chapter 1

Introduction

1-1 Interplanetary CubeSat Missions

“Imagine... Imagine sending an object the size of a shoebox from Earth all the way to Mars, cruising through 100 million kilometres all by itself.”

That is the context of this work. The object the size of a shoebox is a CubeSat and the title of this work reflects this quote : *Combined chemical–electric propulsion and hybrid trajectories for stand-alone deep-space CubeSats.*

A CubeSat is a small spacecraft consisting of single or multiple cubic units, each with dimensions $10 \times 10 \times 10 \text{ cm}^3$. According to the standard developed at California Polytechnic State University and Stanford University [1, 2], along with the said dimensions, each unit should weigh 1.33 kg. However, further research, development and building of new CubeSats has contributed to the relaxation of mass requirements per unit. CubeSats utilise Commercial off-the-shelf (COTS) products related to electronics, materials, small propulsion units, satellite bus etc. Most of these equipment are not space tested and have a medium/medium-high Technology Readiness Level (TRL).

CubeSats have been in usage for Earth-based missions since the turn of the century. These CubeSats, pioneered by CalPoly and Stanford University, have been under development in universities and other private satellite companies. They carry usually one or two scientific or communications payload. Apart from that, the existing standard satellite technologies are miniaturised and manufactured to satisfy CubeSat dimensional and functional constraints. Such CubeSats have sizes nominally ranging from 1U to 6U. While lacking a propulsion system and some other critical systems, these CubeSats are designed to maximise the payload capacity and operate for a shorter duration. They have multifarious mission capabilities, including Earth observation and remote sensing [3, 4], climate assessment [4–6], lower thermosphere characterisation [7], biological research [8] etc.

To expand the horizons, interplanetary CubeSats development will be a necessary step for increasing the solar system exploration efforts at high science-to-investment ratio. Interplanetary CubeSats design and development shall push the frontiers of engineering and technology

by the means of miniaturising and simultaneously increasing the functionality of critical space systems.

Interplanetary CubeSats require several improvements over the existing Low-Earth Orbit (LEO) CubeSat design. They have much research potential, especially in the fields of long-distance communications, deep-space autonomous navigation, propulsion, power generation and management, optimised trajectory guidance, thermal control, robust light-weight structures, accurate attitude determination and control, high-speed low-power computing and processing, on-board data processing, radiation shielding etc. CubeSat missions are *high-risk high-gain missions*, which shall transform the future of robotic exploration paradigm.

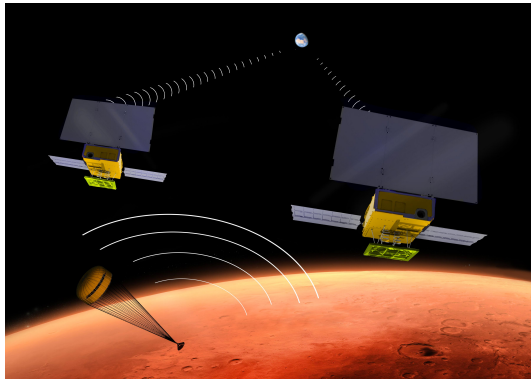
1. *Long-distance communication*: required to establish critical payload data downlink and TC/TM uplink from distances upto 1.5 AU [9, 10].
2. *Autonomous navigation*: critical capability that allows determining the spacecraft state in autonomy during deep-space cruise. The regular radiometric tracking technique could be resource consuming [11, 12].
3. *On-board propulsion*: critical capability that demonstrates orbital manoeuvring and trajectory control, in addition to Earth-escape capabilities in case a launch opportunity into the interplanetary space is unavailable [13, 14].
4. *Power management*: low solar irradiance means low power generation capabilities. Acquisition, storage, and distribution of power is critical for the operational capability of the CubeSats [15].
5. *Durable electronics and subsystems*: they have to endure the harsh environment in the interplanetary space, especially radiation endurance [16, 17].
6. *Trajectory optimisation*: mission analysis and trajectory optimisation is critical for minimising the energy requirements and ensuring spacecraft survivability. Additionally, this serves as the guidance for the navigation system [18].
7. *Thermal control*: spacecraft operation in the near Martian thermal environment requires active / semi-active thermal control system. Capabilities to maintain subsystems in operation and survival temperatures in the Martian environment need to be improved upon.
8. *Attitude determination and control*: owing to the significantly varying pointing requirements during the multiple mission phases for navigation and payload operation, as well as the absence of magnetic fields, highly accurate attitude determination and control are required [19].
9. *High-speed low-power computing and on-board data processing*: to maximise the communication uplink/downlink utility, improve autonomy and to save valuable power, on-board data processing is required to sort out useful science and navigation data for transmission. High processing speeds are required while consuming low power [20].

The increased systems capability and improvement in design would lead to an increased size, between 12U to 16U, depending upon the mission requirements and launch scenarios. Also,

there needs to be a useful payload contained within this size. A 1–1.5U size payload would satisfy limited but significant science requirements.

NASA Jet Propulsion Laboratory (JPL)'s Mars Cube One (MarCO) mission consists of two 6U CubeSats launched as secondary payloads alongside the InSight lander mission to Mars is the only interplanetary CubeSat in existence [21]. The two 6U CubeSats successfully performed a Mars flyby and provided communications relay between the Deep Space Network and the InSight lander during its Mars atmospheric entry, descent, and landing phases. The mission launched in May 2018 using the Atlas V launcher and ejected on a flyby trajectory near Mars [22]. Figure 1-1a depicts the MarCO mission.

Stand-alone CubeSats to near-Earth objects are shown to be feasible, such as the Miniaturised - Asteroid Remote Geophysical Observer (M-ARGO) mission study by the European Space Agency (ESA) depicted in Figure 1-1b [23]. The M-ARGO study has revealed that the limit region reachable by a CubeSat can be fixed at 1.2–1.3 AU. Improvements to communication, power, and propulsion systems could push the envelope to 1.5 AU, thereby making a stand-alone Mars CubeSat feasible.



(a) MarCO (NASA-JPL)



(b) M-ARGO (ESA)

Figure 1-1: CubeSats Mission beyond Low-Earth Orbit: Mars Cube One (MarCO) by NASA JPL and Miniaturised Asteroid Remote Geophysical Observer (M-ARGO) by ESA

A mission to Mars, in the current epoch, is the holy grail for CubeSat exploration. Owing to the relative simplicity and low-costs of CubeSat development, they can be pursued by universities and small spacecraft consortia.

The National Aeronautics and Space Administration (NASA) has funded¹ studies to assess the science mission capabilities achievable by small satellites. These include AEOLUS - study of thermal and wind environments of Mars [24]; Mars Aerosol Tracker (MAT); Mars Ion and Sputtering Escape Network (MISEN); and other missions to Moons of Mars. The European Space Agency has also expressed its interest in pursuing further Mars missions in the following decade.

Possible mission scenarios at Mars include [21, 25]:

- Solar Wind interaction with Ionosphere of Mars.

¹<http://www.lpi.usra.edu/sbag/meetings/jun2017/presentations/Mercer.pdf>. Last accessed: 20-Sep-2019

- ▶ Thermal characterisation of upper atmosphere and analysis of its dynamics by measuring neutral gas velocities.
- ▶ Detection of mini-magnetospheres and their reconnection at Mars.
- ▶ Mars communication relay network setup

These missions could be achieved, albeit with subtle variations, using CubeSats. Typical costs of such a Mission could range from €20–30 million. This represents a significant reduction in cost compared to the existing large spacecraft missions without such a significant reduction in science capabilities. For example, ESA’s ExoMars mission cost is approximately €1.3 billion² while NASA’s MAVEN mission cost \$670 million.

1-2 Need for Primary Propulsion

Interplanetary missions are usually carried out by large spacecrafts that utilise propulsion system for orbital manoeuvring. In such missions, the large spacecraft is the primary payload. The insertion occurs at deep space directly or at an Earth orbit and the spacecraft executes orbit raising and trans-martian injection manoeuvres using large and reliable chemical propulsion systems.

CubeSats are ill-equipped to house a large propulsion system due to their structural and functional constraints. Large thrusters exerting high thrusts could destabilise and damage the structure due to strong vibrations. Moreover, the dimensions of CubeSats impose volume and mass constraints on the propulsion system, which in turn will drastically reduce its capability. Additionally, CubeSats are severely power limited and therefore they cannot accommodate high-power electric propulsion systems.

Until now, Earth-based CubeSat missions have lacked primary propulsion units for orbital change manoeuvres. The propulsion units designed and tested for CubeSats carry out functions such as attitude control, station keeping, formation control/maintenance etc., thus requiring low ΔV and therefore low mass [14]. Additionally, CubeSats are secondary payloads and their release orbits are often restricted by the launch provider and the primary launch payload’s final trajectory. Since the CubeSat design philosophy has revolved around increasing the payload capacity, improving orbital manoeuvrability has been deemed excessive.

Interplanetary CubeSat missions shall eventually have to carry on-board propulsion systems for trajectory and orbit control. The number of large payload missions to Mars are low and occur mostly in a two month launch window every two years. Also, the final destinations of the Mars missions place a constraint on the operational orbits of the secondary payloads, i.e., CubeSats, which may not be fully desirable.

There are two possible ways to accomplish a CubeSat mission at Mars. The first involves an *in-situ* deployment of the CubeSat by a mother ship and the second foresees instead a highly flexible stand-alone CubeSat on deep-space cruise. The stand-alone CubeSat is an appealing option because,

²http://www.esa.int/Science_Exploration/Human_and_Robotic_Exploration/Exploration/ExoMars/ExoMars_frequently_asked_questions. Last accessed: 20-Sep-2019

- ▶ It does not require a primary Mars mission (mother ship), which is rare.
- ▶ The launch could be shared with any primary payload that is bound for a high-energy Earth orbit, drastically increasing the launch options.
- ▶ It has much more flexibility and autonomy, the space segment being stand alone.
- ▶ It would pave the way for novel paradigms in autonomous guidance-navigation-control and operations, so allowing a significant downscaling of the mission costs.

In this approach, the on-board propulsion system becomes inevitable since the CubeSat has to be manoeuvred through the interplanetary space to reach Mars from Earth.

1-3 Motivation and objectives

The primary motivation for the research is to provide design solutions of primary propulsion systems on CubeSats that enable them to explore the interplanetary space while being stand-alone. As mentioned in section 1-2, the primary propulsion systems are indispensable for interplanetary CubeSats.

A successful design, implementation, and proof of concept of an on-board propulsion system shall revolutionise the future of interplanetary small spacecraft travel. The capabilities of CubeSats to perform critical missions beyond LEO will drastically increase. The presence of on-board propulsion systems also broadens the launch windows for interplanetary CubeSat missions since orbital manoeuvrability is enabled. Thus, a launch could be shared with any primary payload that is bound towards a high-energy Earth orbit.

A key concept here is the *combined* chemical–electric propulsion system. For stand-alone CubeSat missions that voyage from Earth orbit to Mars, the spacecraft has to escape Earth and pursue a heliocentric transfer to reach Mars. In the combined chemical–electric propulsion, the CubeSat shall escape Earth within a short timeframe using high-thrust chemical propulsion and perform a deep-space cruise using low-thrust electric propulsion. Fully-chemical transfers are fast but lead to an excessive system mass. Fully-electric transfers save mass but have untenable escape times. Hybrid transfer solutions that utilise chemical–electric propulsion achieve a balance between system mass and transfer time. The emphasis is on the word *combined*, since chemical and electric propulsion are *separate systems present in the same spacecraft*, and are operated alternatively. A qualitative illustration is shown in Figure. 1-2.

The objectives of this research are:

1. **Provide design solutions for combined chemical–electric propulsion systems that enable stand-alone CubeSat missions on a deep-space cruise.**
2. **Develop a methodology for concurrent systems–trajectory design and establish an overall design framework for an interplanetary CubeSat mission.**
3. **To transpose the knowledge of combined propulsion design, concomitant with optimal trajectories for future interplanetary CubeSat designers and propulsion system developers to enhance solar system exploration efforts at high science-to-investment ratio.**

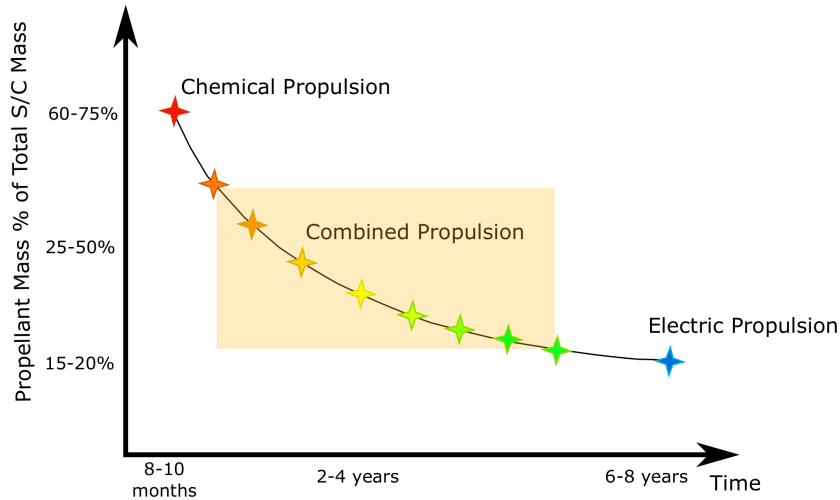


Figure 1-2: Qualitative comparison of fully chemical, fully electric and combined propulsion systems for missions to Mars

1-4 MARIO application case definition

As an application case, a stand-alone CubeSat mission to Mars, called the Mars Atmospheric Radiation Imaging Orbiter (MARIO) is envisaged. The mission statement reads,

The Mars Atmospheric Radiation Imaging Orbiter (MARIO) is a stand-alone CubeSat exploration mission to Mars that shall demonstrate the capabilities of CubeSats to escape Earth, perform autonomous deep-space cruise, achieve ballistic capture, and enter an operational orbit at Mars. It shall utilise combined chemical–electric propulsion, concomitant with hybrid high-thrust–low-thrust trajectories and autonomous guidance–navigation–control. The MARIO mission shall conduct thermal imaging to characterise the temperature in the Mars upper atmosphere. The mission shall serve as a pioneer for interplanetary CubeSat missions with high launch flexibility and cost efficiency.

MARIO is a 32 kg 16U stand-alone CubeSat exploration mission to Mars that shall demonstrate the capabilities of CubeSats to perform a) orbit raising & Earth escape, b) low-thrust deep-space cruise c) ballistic capture at Mars and d) acquisition of the final operating orbit. These are the 4 key phases of this mission.

The injection orbit is a highly-eccentric SSGTO with a perigee of 295 km and an apogee of 90,000 km. Such injection orbits are commonplace for contemporary geostationary satellite missions that utilize electric propulsion for apogee reduction and circularization to GEO; e.g. Falcon 9 v1.1 rocket launched Thaicom 6 in January 2014 into this orbit and Thaicom 8 in May 2017 into a 350 km × 90226 km orbit³. Owing to the higher number of communication satellite launches (> 5 per year) compared to deep-space launches (~1 per year), this orbit is

³Space Launch Report - Falcon 9
<http://www.spacelaunchreport.com/falcon9ft.html> and <https://www.spacex.com/missions>. Last visited: 10-Mar-2019

selected to (a) improve the launch opportunities and widen the launch window, (b) reduce the ΔV required for Earth escape, and (c) provide more flexibility and autonomy to the CubeSat mission by diminishing its dependence on larger interplanetary spacecraft.

Swift escape is required to avoid excessive radiation damage since the spacecraft crosses the Van Allen radiation belts. A high-thrust chemical propulsion system is required to provide high ΔV within a short duration. A low-thrust electric propulsion system instead will drastically increase the residence time of the spacecraft in the radiation belts. The maneuvers are split and multiple orbit raisings are pursued to effectively distribute the ΔV and achieve Earth escape within a short timeframe while controlling gravity losses. Figure 1-3a illustrates the orbit raising and escape using chemical propulsion.

Once Earth escape is achieved, the deep-space cruise or heliocentric transfer to Mars is executed using low-thrust high-specific impulse electric propulsion (Figure 1-3b). Two strategies are investigated: a) time-optimal continuous thrusting and b) fuel-optimal bang-bang thrusting control. The critical resource for the electric propulsion system is the available power, and the specific impulse and thrust depend on it.

At the end of the cruise, the spacecraft experiences a *ballistic capture* (Figure 1-3c). This is a phenomenon through which the spacecraft is *captured* into a temporary stable orbit about Mars, only by virtue of the natural attractions of Mars and the Sun [18]. The orbit acquired by the spacecraft after ballistic capture is highly irregular, and thus unusable for continuous observation missions. A high-thrust maneuver is performed to reduce the initial eccentricity and stabilise the orbit. The circularization to 60,000 km orbit is completed through low-thrust propulsion (Figure 1-3d). At this orbit, the planned thermal camera payload will characterise the temperature in the Mars upper atmosphere.

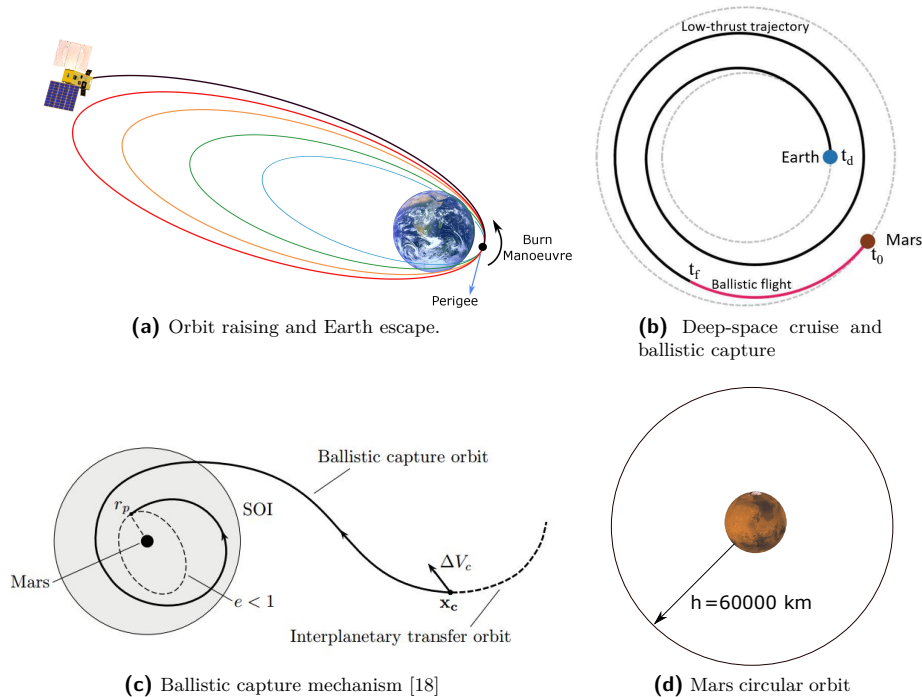


Figure 1-3: MARIO Mission Phases

The overall requirements of the MARIO spacecraft are defined in Table 1-1. Currently, the largest CubeSat structure available in the market has a 12U form factor. The Lunar Meteoroid Impact Observer (LUMIO) mission [26] and the Miniaturised-Asteroid Remote Geophysical Observer (M-ARGO) [23] have this structure and a total maximum mass of 24 kg. Considering the stand-alone nature of MARIO and its voyage from an Earth orbit to Mars orbit, a direct scaling was done and the maximum size requirements, OVRSYS-01 and OVRSYS-02, were set as 32 kg with a 16U form factor. OVRSYS-04 sets the minimum operation time as 6 years considering the long duration low-thrust cruise to Mars, acquisition of the operational orbit, and then 6-8 months of scientific observation.

Table 1-1: MARIO Overall System Requirements

ID	Requirement
OVRSYS-01	The mass of the spacecraft shall be no greater than 32 kg
OVRSYS-02	The spacecraft volume shall not exceed the configuration of a 16U CubeSat
OVRSYS-03	The system shall establish long-distance communication with Earth up to a range of 1.5 AU
OVRSYS-04	The system shall be operational for a minimum of 6 years

1-5 Research questions and hypotheses

This section highlights the primary research questions and corresponding hypothesis that are instrumental in achieving the objectives.

1-5-1 Main research questions

1. What is the design strategy for combined chemical–electric propulsion for a stand-alone CubeSat to Mars?
 - ▶ Hypothesis: The design strategy shall be to define the mission characteristics first and the general system. The state-of-the-art propulsion system concepts must be explored and design requirements must be set based on the mission context. A trade-off analysis must be performed to select the suitable system for further design. Propellant analysis and selection should then be done. Initial design characteristics must be predicted and the thruster performance must be modelled. The design must be iterated until the required performance is achieved. Trajectory simulation must be done by incorporating the thruster performance and the sizing parameters must be obtained. Key parameters which interface the chemical and electric propulsion system design must be identified and incorporated to find an overall design solution.
2. What are the design and performance characteristics for combined chemical–electric propulsion that enable stand-alone deep-space CubeSats to Mars?
 - ▶ Hypothesis: The design characteristics of the propulsion systems are heavily mission dependent. Apriori assessment is that the chemical propulsion system utilised

for Earth escape from a high energy orbit will have an overall mass of 20-25% of the initial system mass and a volume of 50–52% of the initial spacecraft volume. This is due to many factors including specific impulse, propellant density, combustion characteristics etc. The maximum thrust is limited to a certain value, $\sim 2 - 3$ N, in order to avoid structural damage and irrecoverable destabilisation of the CubeSat. The specific impulse shall be between 220–260 seconds. The electric propulsion system shall have a high lifetime and a high specific impulse. Owing to the long duration of the flight to Mars after Earth escape, the system will accrue a large ΔV , which in-turn affects the propellant mass. The overall system mass would be 20-25% of the initial mass. The electric propulsion system volume depends upon the propellant density and specific impulse. The performance characteristics would be 1-1.8 mN thrust and ~ 3000 seconds specific impulse.

3. What are the trajectory characteristics of a stand-alone CubeSat mission to Mars?

- ▶ Hypothesis: The trajectory of a stand-alone CubeSat mission to Mars depends upon the injection orbit. If we are to assume that the mission is injected into a high-energy Earth orbit, the spacecraft orbit needs to be raised and a final escape manoeuvre executed using high-thrust propulsion. The primary reason for this is to achieve a escape within a short duration to minimize damage due to the radiation accumulated through multiple Van Allen belt crossings. Additionally, there needs to be an effective distribution of the ΔV required for escape over multiple manoeuvres to avoid gravity losses. Once the Earth escape is achieved, a low-thrust deep-space cruise should be executed to reach Mars. Utilising high-specific impulse low-thrust propulsion ensures higher control authority and greater mass savings. The natural phenomenon called *Ballistic capture* needs to be exploited for zero ΔV capture and insertion into a Mars orbit. Additional circularization is required to acquire an operational orbit.

4. How can the low-thrust propulsion system and trajectory be concurrently optimised?

- ▶ Hypothesis: by creating a framework in which the thruster and trajectory control parameters are concurrently optimised to achieve the designated target point from a given initial point within the shortest timeframe. The thruster performance envelope needs to be defined and it must be incorporated in the orbit propagation equations. Throughout the optimisation scheme, the critical system and trajectory constraints need to be satisfied.

1-5-2 Sub-questions based on chemical propulsion

1. What are the state-of-the-art CubeSat chemical propulsion systems and what is the best choice for the current application?
2. What are the limiting factors and constraints in interplanetary CubeSat chemical propulsion systems design?
3. What are the desired performance and design metrics for a chemical thruster on-board a stand-alone CubeSat mission to Mars?

1-5-3 Sub-questions based on electric propulsion

1. What are the state-of-the-art CubeSat electric propulsion systems and what is the best choice for the current application?
2. What are the limiting factors and constraints in interplanetary CubeSat electric propulsion systems design?
3. What are the desired performance and design metrics for the electric propulsion system?

1-6 Structure of the document

Until now, we have established the need, motivation, objectives, application case and the important research questions. The document is primarily divided into five chapters.

Chapter 2 deals with the chemical propulsion system and the high-thrust trajectory. The state-of-the-art chemical propulsion systems applicable for CubeSats is explored. A system design strategy is defined and a trade-off analysis is performed to select the suitable system. The propellants are analysed and a performance analysis is performed. Thruster design and performance are characterised and high-thrust trajectory analysis is done. Overall system design and sizing are then presented.

Chapter 3 deals with the electric propulsion system and the low-thrust trajectory. The state-of-the-art of electric propulsion technology applicable for CubeSats is explored. Propellant analysis and comparison is presented. A thruster performance model is defined and the low-thrust trajectory optimisation is pursued.

Chapter 4 presents the overall system design of MARIO. A preliminary design that provides an overview of the mission and the context for the research is presented.

Chapter 5 deals with the concurrent propulsion–trajectory optimisation. Thruster performance envelope is defined and a novel framework is established to incorporate thruster control parameters into trajectory optimisation.

The research work is summarised in chapter 6 and conclusions are drawn. The answers to the research questions are presented along with some recommendations for future work.

Chapter 2

Chemical propulsion

2-1 Chemical propulsion principles

Chemical Propulsion (CP) systems enable high-thrust manoeuvres which are critical in quick and effective orbital changes. The thrust-to-power ratio of chemical propulsion systems is much higher compared to other types of rocket propulsion systems. They are the basic type of thermal rocket propulsion systems and they do not require any external medium or oxidant for the burning fuel. They are heat engines that convert the heat energy produced by the combustion of the propellants, fuel and oxidiser, in the combustion chamber into kinetic energy of the exhaust gas by accelerating it through a convergent-divergent nozzle. The reaction force of this action onto the nozzle structure is the thrust force, which when applied over a time period results in a change in momentum of the rocket or the spacecraft.

The main performance parameters for the chemical propulsion system are thrust (T), specific impulse (I_{sp}), exhaust velocity (v_e), and Delta V (ΔV). Thrust is obtained using the mass flow rate \dot{m} of the propellant, exhaust velocity v_e , pressure at the nozzle exit P_e and the ambient pressure P_a , and the exit area of the nozzle A_e , as shown in equation (2-1). The specific impulse I_{sp} is the thrust produced per unit weight of propellant consumed (equation (2-2)).

$$T = \dot{m} v_e + (P_e - P_a) A_e \quad (2-1)$$

$$I_{sp} = \frac{T}{\dot{m} g_0} \quad (2-2)$$

$$(2-3)$$

In equation (2-1), the first term is the linear momentum thrust represented by the product of \dot{m} and v_e . The second term is the pressure thrust which is the product of the nozzle exit area A_e and the difference between the nozzle exit pressure P_e and the ambient pressure P_a . Rocket nozzle is designed to have the P_e equal to or greater than P_a to have a net positive

pressure thrust contribution. When $P_e = P_a$, the nozzle has optimum expansion ratio [27]. For propulsion in space, the ambient pressure $P_a = 0$ due to the vacuum conditions. The effective exhaust velocity $v_{e,eff}$ applies to all rocket systems that use thermodynamic expansion of hot gasses in the nozzle.

$$v_{e,eff} = v_e + \frac{(P_e - P_a) A_e}{\dot{m}} \quad (2-4)$$

Under optimum expansion, where $P_e = P_a$, the effective exhaust velocity is equal to the actual nozzle exhaust velocity, i.e. $v_{e,eff} = v_e$. However, when $P_e \neq P_a$, then $v_{e,eff} \neq v_e$. Different chemical propulsion systems can be compared using the parameter characteristic velocity c^* . It is defined in equation (2-5).

$$c^* = \frac{P_c A_t}{\dot{m}} \quad (2-5)$$

Here, P_c is the combustion chamber pressure and A_t is the nozzle throat area. Another critical parameter that influences the performance of a chemical propulsion system is the nozzle expansion area ratio ε which is A_e/A_t . The specific impulse I_{sp} and the effective exhaust velocity $v_{e,eff}$ are functions of nozzle geometry, particularly A_e/A_t .

Finally, the change in velocity, i.e., ΔV imparted to the spacecraft is expressed using the famous Tsiolkovsky Rocket Equation, shown in equation (2-6). It depends upon v_e , initial mass m_0 and final mass m_f of the spacecraft. The consumed propellant mass m_p is the product of \dot{m} and the burntime t_b .

$$\Delta V = v_e \ln \left(\frac{m_0}{m_f} \right) \implies I_{sp} g_0 \ln \left(\frac{m_0}{m_0 - m_p} \right) \quad (2-6)$$

Chemical propulsion systems can be classified by the type of propellant they use and working mechanism by which they produce the thrust: Solid Rocket Motor (SRM), Liquid Rocket Engine (LRE), Hybrid Rocket Engine (HRE), and Cold Gas (CG) systems [27]. They can be further classified by complexity which greatly varies among different systems depending upon the application and size. In the current context, only the chemical propulsion systems applicable to CubeSats and small spacecraft are analysed. The content presented in this chapter is partially based on the published work of the author: Mani et al *Combined Chemical–Electric Propulsion for a Stand-Alone Mars CubeSat* [28], Mani et al *Dual chemical-electric propulsion systems design for interplanetary cubesats* [29], and Mani et al *Chemical Propulsion System Design for a 16U Interplanetary CubeSat* [30].

2-2 CubeSat chemical propulsion system state-of-the-art

For the sake of brevity, the chemical propulsion systems will be analysed based on the major stand-alone Mars CubeSat mission requirements. This contextual approach will narrow down the search and paint a clear picture regarding the design flow. The analysis is not limited to commercial off-the-shelf (COTS) equipment that satisfy the requirements and includes also the thruster technologies that can be adapted to deliver the desired performance for a successful execution of the mission. Emphasis is placed on the capability of the propulsion

system to deliver sufficient thrust and specific impulse for major orbital manoeuvres, thereby acting as a primary propulsion system rather than the capabilities regarding attitude control, station keeping and formation control.

This section is further organised as follows: the state-of-the-art of the chemical propulsion system types such as CG, SRMs, and LREs are delineated. The basic working principles, advantages and disadvantages, design considerations, and performance ranges of these propulsion systems are expounded. Some important review works on the state-of-the-art of small satellite propulsion systems can be found in Mueller et al [13], Lemmer [14], Tummala and Dutta [31], and the NASA technical report - *Small Satellite Technology State of the Art 2018* [32]. Other innovative concepts include dual mode thrusters that have a high-thrust chemical mode and a high- I_{sp} electric mode [33]. However, this has not been assessed in this work as part of the state-of-the-art.

2-2-1 Cold gas

Gaseous rocket propellant engines use a high-pressure gas such as nitrogen, helium or air that is stored in a tank and then discharged through a supersonic nozzle to produce the thrust. The gas is either cold or warm and they contain lower energy compared to the hot gases produced by liquid rocket engine combustion.

In the case of Cold Gas (CG) systems, the source of energy is the stored enthalpy of the gas and there is no combustion or heat addition [14]. A CG system consists of a pressurised propellant tank, valves, feed pipes, and the nozzle. Power is required to control the valves and keep the propellant temperature at the required level. Additionally, the gaseous propellant should be rid of any moisture before being accelerated through the nozzle.

CG systems are the simplest of all propulsion systems. They have an excellent flight heritage and have a high degree of reliability. Spacecraft contamination is negligible or non-existent if CG systems are used. They can be operated over thousands thrust cycles without loss of thruster performance. Traditionally, CG thrusters are used in large spacecraft for attitude control since they have low impulse-bit.

Performance wise, CG systems have a much lower I_{sp} and deliver less ΔV for the same spacecraft mass since the gas enthalpy alone is insufficient to provide equivalent performance to that of other systems since the energy of the chemical bonds is not used [14]. The thrusting capacity of CG systems applicable for small satellites and CubeSat ranges from a few mN to 2.36 N. Typical I_{sp} values range from 40–75 seconds [13, 14].

One major advantage of the CG system is that it is compatible with a very wide range of propellants. Common propellants used are nitrogen, xenon, argon, R134a etc. Given the low I_{sp} and since the gases have to be stored at high pressure, the mass fraction of the system is very large. The propellant mass is large and the tanks required to store the propellants need to have thick walls made of heavy materials. The high storage pressure also increases the risk of leak in the feed system. The CG systems usually operate in blow-down mode and the thrust decreases with the decrease in storage pressure.

Several CG thrusters for small satellite applications have been developed. Cold Gas Micro-Thruster developed by Marotta provides a maximum thrust of 2.36 N while having an $I_{sp} \sim 65$ s. Moog Inc has developed two CG thrusters, models 058-118 and 58E163A. The former

provides a thrust of 3.6 N @15.7 bar of gaseous nitrogen (GN_2). The latter is configurable to use xenon, GN_2 , and gaseous Argon. 58E163A provides 1.3 N @ 90 bar xenon inlet and 0.9 N @ 90 bar GN_2 and GAr inlet. Surrey Space Technology Ltd (SSTL) has developed a butane based system in which they include a resistojet thruster that utilises electrical power to heat the gas such that the I_{sp} is improved [34]. Several MEMS cold gas thrusters have been developed for precision manoeuvres that require very low-impulse bit and thrusts. CG thrusters providing thrusts in the millinewton range are manufactured by companies like VACCO and Aerospace Corporation [14, 32, 35, 36]. The state-of-the-art of CG systems are listed in Table 2-1.

Table 2-1: Summary of cold gas propulsion state-of-the-art

System	Manufacturer	Propellant	Avg. Thrust [N]	I_{sp} [s]	TRL
Cold Gas Micro-thruster	Marotta Controls Inc.	GN_2	0.05–2.36	65	9
Cold Gas 58E163A	Moog Inc.	xenon	1.3	21	6
		GN_2	0.9	70	6
		GAr	0.9	54	6
		GN_2	3.6	57	9
Cold Gas 058-118	Moog Inc.	GN_2	3.6	57	9
Butane Propulsion Sys.	SSTL	butane	0.5	80	9
MEMS thruster	Aerospace Corp.	xenon	0.1	30	9
MEPSI MiPS	VACCO	isobutane	0.053	65	7
MarCO MiPS	VACCO	R236fa	0.025	40	9

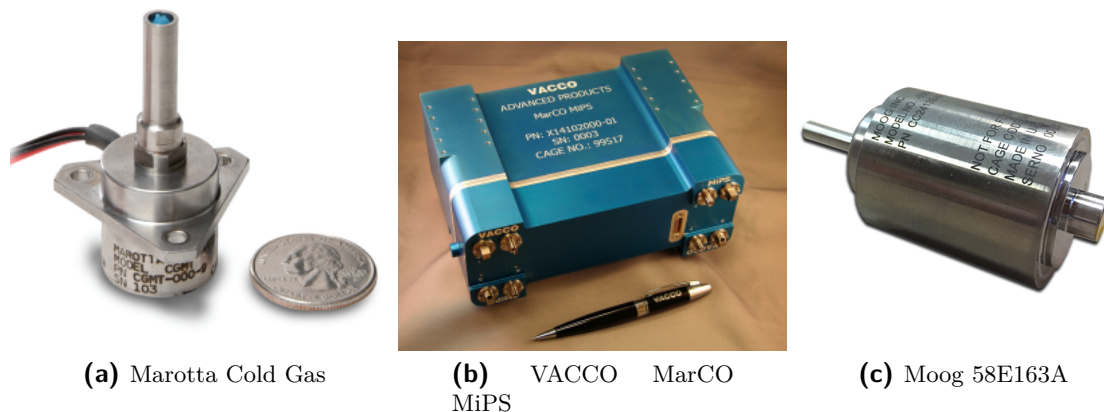


Figure 2-1: Cold gas systems state-of-the-art. Cold gas micro-thruster by Marotta Controls Inc. (image retrieved from brochure [37]), MarCO MiPS by VACCO (image retrieved from datasheet [35]), and Moog Inc 58163A (image retrieved from datasheet [38])

2-2-2 Solid rocket motors

Solid rocket motors in CubeSats can be used for orbit raising, trajectory insertions and rapid de-orbiting [13]. An SRM consists of a combustion chamber in which the fuel and the oxidiser are premixed in a solid form. The solid mix, which includes a binder resin to keep it intact as well as other chemical components, is called the *grain*. The most common propellant mix used in SRMs consist of Hydroxyl-terminated polybutadiene (HTPB), aluminium powder as fuel additive and ammonium perchlorate (NH_4ClO_4). The grain consists of approximately

82–94% of the total motor mass [27]. The grain can be cast in different shapes and it is ignited to burn along a particular exposed inner surface to produce hot combustion gases, which in turn are accelerated through the nozzle. The rate of burn is predetermined since the grain also contains a specific amount of inhibitors or accelerators that control it.

Since all the propellants are stored in the motor case, no dedicated feed and storage system is required. Additionally, they do not have any moving parts except, in special cases, where there are movable nozzles for thrust vectoring. Given that even small SRMs have a specific impulse in the range of 180–260 seconds, this allows for very tight packaging and an easy integration into the CubeSat structure. Solid propellants can be stored for very long periods in vacuum conditions without significant degradation in performance if the propellant casting process is good enough to ensure the avoidance of bubbles, cavities and gaps.

SRMs burn continuously and once started, they cannot be stopped. They do not have restart capabilities. The thrust variation is predetermined based on the grain composition and it cannot be adjusted during flight, thus yielding no real-time control capability. The thrust magnitudes are high, and this results in large vehicle accelerations which may destabilise the spacecraft [32]. Additionally, even high performance SRMs have a thrust misalignment between 0.15° – 0.25° and smaller SRMs would have double this value [39, 40]. This necessitates the inclusion of a robust attitude control system or a thrust vector control for proper steering during acceleration, which increases the system cost. Owing to their "one-time-fire" nature and their vulnerability towards misfires arising from ignition issues, the reliability of SRM performance is lower than that of other system types. Although the mechanical and thermal properties are not affected by vacuum conditions, the gamma ray irradiation (especially during solar flares) severely deteriorates the mechanical properties and exacerbates thermal decomposition [41].

One way to overcome the issue of single-shot burn is to design SRMs with multiple solid propellant micro-thrusters to form a pack. Each of these unit shall be equipped with a micro-nozzle through which the combusted propellant is accelerated. Additionally, thrust can be varied by firing a combination of these micro-thrusters, either simultaneously or sequentially [42–44]. Another alternative technology is the digital solid state propulsion in which the solid propellant is ignited when electric current is passed through it. This allows for better thrust control since the combustion is sustained only through continuous supply of electricity.

The current state-of-the-art SRMs applicable for CubeSats and small spacecraft include ISP 30 sec motor by Industrial Solid Propulsion, Northrop Grumman Innovation Systems (NGIS - previously Orbital ATK) STAR 4G and STAR 5A, and Digital Solid State Propulsion (DSSP)'s CubeSat Agile Propulsion System (CAPS) and CubeSat Delta-v Motor (CDM). They are summarised in Table 2-2 [13, 31, 32, 40]. It has to be noted that most of the SRMs developed for CubeSat applications were done for fast de-orbiting operations to avoid the accumulation of uncooperative objects in LEO.

2-2-3 Liquid monopropellant engines

The liquid chemical propulsion system consists of a combustion chamber, a convergent-divergent nozzle, an injector head, propellant storage tanks, and feed lines and pipes that deliver the propellant from tanks to the chamber. The propellants are fed under pressure and they can be further classified as pressure-fed or pump-fed systems. Pressure-fed systems

Table 2-2: Summary of solid propulsion state-of-the-art

Motor	Manufacturer	Avg. Thrust [N]	I_{sp} [s]	TRL
ISP 30 sec	Industrial Solid Propulsion	37	187	6
STAR 4G	Northrop Grumman Innovation Systems	258	269.4	6
STAR 5A	Northrop Grumman Innovation Systems	170	251	6
CAPS-3	Digital Solid State Propulsion	0.3	8	
CDM-1	Digital Solid State Propulsion	76	226	6

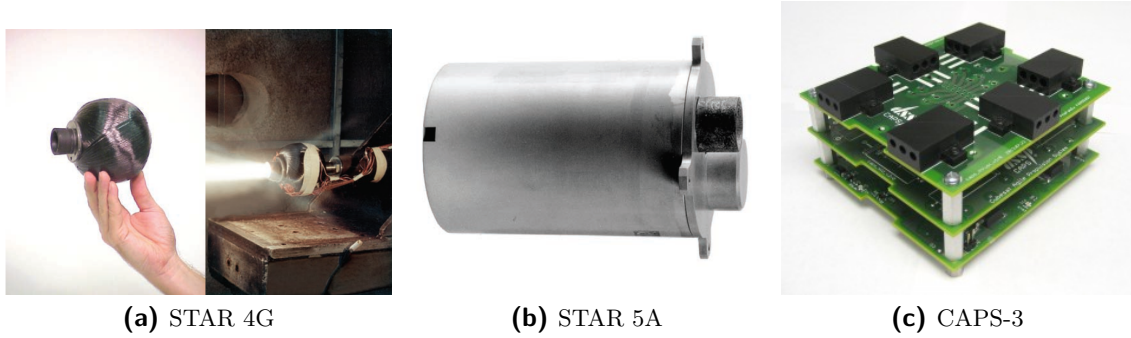


Figure 2-2: Solid rocket motors state-of-the-art. STAR 4G and STAR 5A by Northrop Grumman Innovation Systems (images retrieved from catalog [45]) and CAPS-3 by Digital Solid State Propulsion (image retrieved from brochure [46])

are typically used in satellite applications where the thrust and total energy requirements are low. Pump-fed engines are used where larger thrusts are required and amount of propellants are very high. Pump-fed systems are inherently more complicated than pressure-fed systems due to the presence of multiple moving parts.

LREs have restart capability and can be operated through many cycles. The thrust can be controlled with precision using flow control valves and can be varied along the performance envelope to suit mission needs. LREs on average have a higher I_{sp} than SRMs and a significantly higher I_{sp} than CG systems. Thrusting capability is flexible and the systems can deliver a wide range of impulse bits.

Monopropellant propulsion systems are liquid rocket engines that use a single propellant which is either exothermically decomposed using a catalyst bed or thermally ignited to form hot high-pressure gases and reaction products that are accelerated through the nozzle. The decomposition of the propellant results in the break of chemical bonds and a subsequent release of energy. Owing to energy conservation, the exhaust gas temperature increases and subsequently the gas velocity also increases.

In a pressure-fed system, the propellant stored in a pressurised tank is delivered to the thrust chamber comprising either a catalyst bed or an ignition system. Valves are used to actuate the flow between the storage tanks and the thruster. The two types of pressure-fed system include a blow-down system and a regulated system. The pressure in the propellant tank operated in blow-down mode keeps reducing as the thruster is operated. The pressure regulated system

uses a separate pressurant gas that is used to keep the propellant tank pressure at the desired level. Valves are utilised to regulate and control the flow from the tanks to the thrust chamber.

Common propellants used in monopropellant systems include hydrazine (N_2H_4), hydrogen peroxide (H_2O_2) as well as green propellants such as blends of Ammonium dinitramide (ADN) and Hydroxylammonium nitrate (HAN). Hydrazine based monopropellant systems have a rich flight heritage and have been used in attitude control systems for large satellites. Hydrazine offers a moderately high I_{sp} , 200–230 s, and has a high liquid phase density of 1004 kg/m^3 [47]. However, hydrazine is toxic and carcinogenic, and alternative propellants that are less harmful are required [48, 49]. The toxicity of hydrazine makes it prohibitively expensive to deal with since extraordinary precautions need to be taken in the case of CubeSat applications to satisfy the stringent safety requirements [50].

Concentrated hydrogen peroxide, known as "high-test peroxide", is also used in monopropellant systems. Typical concentrations range from 80%–95%. It decomposes slowly over time and the rate of decomposition depends upon the ambient conditions, concentration, and the purity of H_2O_2 [51]. The density of 87.5% H_2O_2 solution is $\sim 1380 \text{ kg/m}^3$ at 20°C . The I_{sp} yield of H_2O_2 is 140–180 seconds [52].

Green monopropellants are non-toxic alternative to hydrazine and comparatively have very low volatility and vapour pressures at atmospheric conditions [14, 47]. *Green* refers to the property of the propellants being less flammable, therefore requiring fewer safety requirements in terms of handling, storage, and operation [32]. Accidental combustion of hydrazine is a serious risk and green propellants do not combust easily. Additionally, leakage of hydrazine is considered a catastrophic risk while green propellants do not contaminate or corrode other components when leaked. Propellants such as blends of ADN and HAN are utilised in green monopropellant systems. ADN blends used are propellants LMP-103S [53] and FLP-106 [54] both developed by Swedish Space Corporation. HAN blend widely in use is AF-315ME developed by the United States Air Force Research Laboratory [55]. ADN and HAN based green propellants have higher densities, ~ 1238 – 1470 kg/m^3 , and higher I_{sp} , ~ 230 – 260 s , compared to hydrazine [56].

Monopropellant thrusters available on the market have a thrust range of 0.5–1.5 N. MPS-120 developed by Aerojet Rocketdyne that uses hydrazine has a thrust of 1 N and an I_{sp} of 225 s [14, 50]. MONARC-1 thruster developed by Moog Inc has a steady state thrust of 1 N and an I_{sp} of 230 s [38]. Hydrogen peroxide based thrusters are under development at the Austrian Institute of Technology (previously Austrian Research Centers GmbH) and at the Forschungs-und Technologietransfer GmbH (FOTEC) [52].

High performance green propulsion (HPGP) thrusters developed by Bradford ECAPS using LMP-103S propellant, a blend of ADN, has successfully flown aboard the PRISMA satellites [53]. Thrusters using FLP-106 are currently under development [49, 54]. VACCO partnered with ECAPS to design an ADN based thruster for Lunar Flashlight mission [32]. NASA's Green Propulsion Infusion Mission (GPIM) is a technology demonstration project that used AF-M315E propellant, a blend of HAN, to test the applicability of green chemical propellant to CubeSats. The mission used GR-1 and GR-22 thrusters developed by Aerojet Rocketdyne [55, 57, 58]. Aerojet Rocketdyne adapted its MPS-120 thruster for HAN-based propellant [59]. Busek Company Inc developed the HAN based BGT-X5 and BGT-1X thrusters that provide thrusts of 0.5 N and 0.1 N, respectively. Some of the state-of-the-art monopropellant systems are summarised in Table 2-3.

Table 2-3: Summary of liquid monopropellant state-of-the-art

System	Manufacturer	Propellant	Avg. Thrust	I_{sp} [s]	TRL
MPS-120	Aerojet Rocketdyne	Hydrazine	1 N	225 s	6
MPS-130	Aerojet Rocketdyne	HAN	1 N	244 s	6
1N HPGP	Bradford ECAPS	LMP-103S (ADN)	0.25–1 N	204–235 s	9
GR-1	Aerojet Rocketdyne	HAN	0.26–1.42 N	231 s	9
BGT-X5	Busek Company Inc.	HAN	0.5	220 s	5
MONARC-1	Moog Company Inc.	Hydrazine	1	227.5 s	9

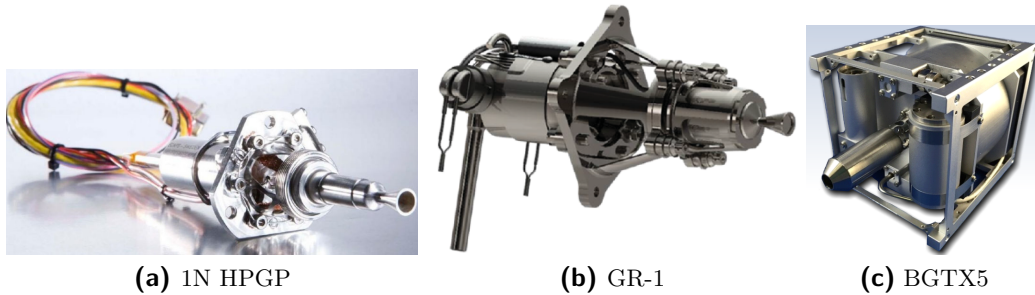


Figure 2-3: Liquid monopropellant engines state-of-the-art. 1N HPGP thruster by Bradford ECAPS (image retrieved from brochure [60]), GR-1 thruster by Aerojet Rocketdyne (image retrieved from Mclean et al [55]), and BGT-X5 by Busek Company Inc. (image retrieved from brochure [61])

2-2-4 Liquid bipropellant engines

Liquid bipropellant engines use a fuel and an oxidiser stored in separate tanks. The propellants are delivered at the required pressure and mixture ratio into the combustion chamber using a complex feed system. The bipropellant system nominally requires two separate feed systems for the fuel and the oxidiser since the mass flow rate and pressure of each must be independently controlled. The system can be either pressure-fed or can use micro-turbopumps [52]. However, turbopumps are not generally used in spacecraft applications due to low-thrust requirements, high-speed rotating parts causing instabilities, and increased risk of malfunction. The propellants can be injected as liquids, gases or even super critical fluids [62]. A lot depends upon the type and design of the injectors as that has a direct implication on the mixing process. Propellants in liquid states are atomised, vaporised, mixed and then combusted. Ignition of the propellants is achieved using an active ignition system or by allowing the propellants to auto-ignite upon contact (hypergolic).

The traditional bipropellant system can be operated in different cycles: expander cycle, gas generator cycle, and the staged combustion cycle. Cryogenic engines utilise the expander cycle, in which a cryogenic propellant is fed through the cooling jackets around the combustion chamber exchanging heat, then the heated propellant gas is passed through the turbine and finally fed into the combustion chamber. The gas generator cycle uses a separate chamber in which a smaller amount of the propellants are combusted to generate hot gases which then run the turbine. This gas is then dumped overboard. In the staged combustion cycle, the hot

gases from the gas generation chamber are directly fed into the main combustion chamber. This cycle yields the highest I_{sp} .

Common propellant combinations for bipropellant thrusters applicable for small spacecraft include ethanol & kerosene, gaseous hydrogen & oxygen, and ethanol & hydrogen peroxide [14, 52]. Hypergolic propellants such as unsymmetrical dimethylhydrazine (UDMH), dinitrogen tetroxide (N_2O_4), monomethyl hydrazine (MMH) etc. are not used for small satellite applications since the risks relating to accidental ignition, explosion, leakage and contamination are immense. Hydrogen peroxide used in bipropellant systems needs to be fed through a catalyst bed such that it decomposes into water and oxygen [52].

Bipropellant engines do not have a lot of maturity in terms of CubeSat applications. They are inherently much more complex than liquid monopropellant systems. The main advantage of bipropellant systems is that they offer much higher I_{sp} and thrusting capability than any other chemical propulsion system. They are utilised for high- ΔV missions. The traditional operation cycles that use turbopumps are not applicable to CubeSats since the primary principles of design are simplicity and lower costs. Therefore, the system must utilise propellants with similar fluid properties thereby avoiding complex feed system. Designs involving non-toxic propellants such as nitrous oxide (N_2O) and dimethyl ether (DME), yielding a thrust of 0.4 N and an I_{sp} of 290 s are proposed [63]. Another design is the HYDROS thruster proposed by Tethers Unlimited Inc., in which water is converted into hydrogen and oxygen through electrolysis and the two gases are combusted in the thrust chamber [14]. Some bipropellant MEMS devices have been developed which could be applicable to small satellites. They integrate the valves, pumps, thrust chamber and nozzle into a single microfabricated chip. Marcu et al [64] proposed a design that could deliver 13–45 N thrust with an I_{sp} of ~ 300 s (shown in Figure 2-4). FOTEC developed a bipropellant thruster that utilises ethanol and H_2O_2 yielding a performance of 1 N thrust and ~ 300 –315 s I_{sp} [52, 65]. The thrusting performance could be extended upto ~ 1.5 N by adjusting the thruster geometry.

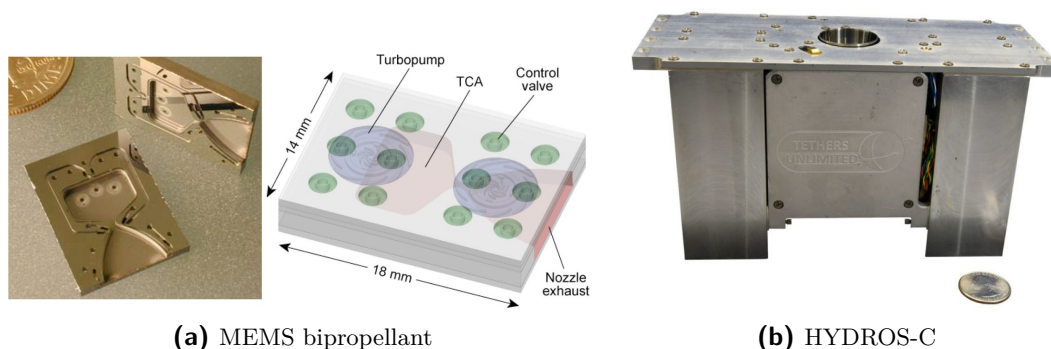


Figure 2-4: Bipropellant system state-of-the-art. MEMS bipropellant thruster design (image retrieved from Marcu et al [64]) and HYDROS-C by Tethers Unlimited (image retrieved from datasheet [66])

2-3 System design strategy and trade-off

The design strategy is illustrated in Figure 2-5. The top-level mission characteristics are defined in section 1-4.

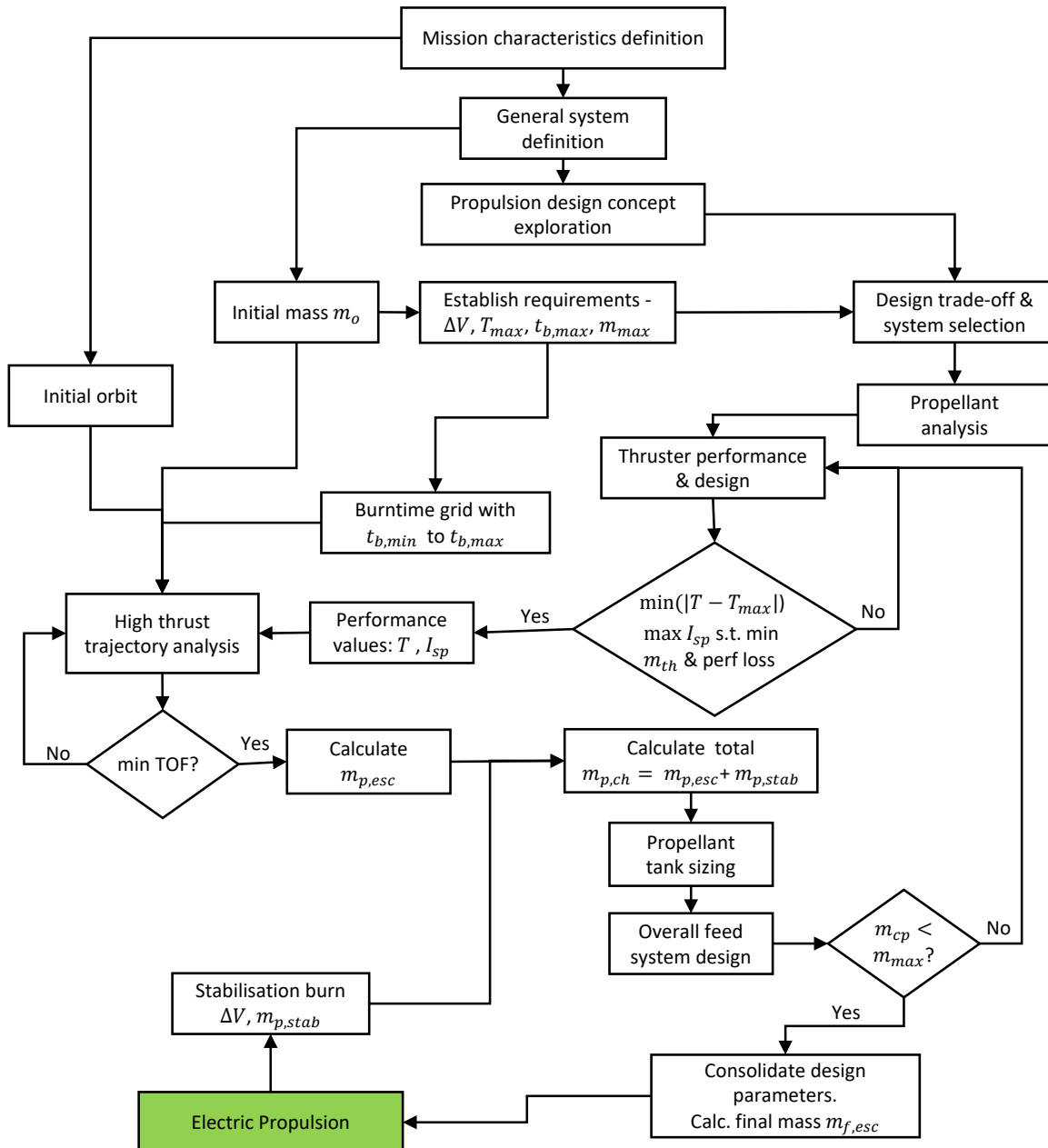


Figure 2-5: Chemical propulsion system design strategy

The MARIO mission pursues a hybrid high-thrust–low-thrust trajectory to perform escape Earth, low-thrust deep-space cruise, ballistic capture at Mars, and acquisition of an operational orbit. The chemical propulsion system is used in the high-thrust trajectory phase

where orbit raising and Earth escape is pursued. It is also used for orbit stabilisation at Mars immediately after ballistic capture.

The state-of-the-art of the chemical propulsion systems applicable to CubeSats and small satellites was explored in section 2-2. Additionally, some of the most crucial design concepts were realized. One of the objectives of this work is to provide a design solution for the chemical propulsion system that shall enable the MARIO mission. The exploration of the state-of-the-art and the corresponding concepts guides the design approach such that a pertinent solution for the particular mission application can be achieved. It has to be noted that the design of the chemical propulsion system strongly depends upon the requirements and constraints pertaining to the design and performance.

The chemical propulsion system requirements are established in this section. They are established based on the ΔV needed for the orbital manoeuvres performed using the chemical propulsion system, the maximum thrust that shall be imparted to the spacecraft, the maximum duration of burn, the maximum mass of the system as a design constraint, and the safety measures for the system. The propulsion system concepts are traded off based on the system performance and design requirements, and a suitable propulsion system type is selected for further design.

The applicable propellants are analysed, the thruster design is pursued, and the corresponding thruster performance analysis is done until the performance requirements are delivered. A high-thrust trajectory analysis is carried out using the calculated thruster performance. The goal of the high-thrust trajectory analysis is to calculate the trajectory parameters and the required propellant mass that corresponds to the shortest flight time to escape Earth. Once the propellant mass is calculated, the feed system design is pursued and the overall system sizes are established. Iteration of the thruster design and the propulsion system design is done until the overall MARIO system design constraints and requirements are met. The final design is then established.

The chemical propulsion system requirements are listed in Table 2-4.

Table 2-4: Chemical Propulsion System Requirements

ID	Requirement
CP-01	The system shall provide a minimum $\Delta V = 445$ m/s for orbital transfer and Mars orbit stabilization maneuvers.
CP-02	The system shall have a maximum thrust of 3 N
CP-03	The maximum thrusting time shall be 600 seconds per orbital manoeuvre
CP-04	The total mass of the chemical-electric propulsion systems shall be no more than 16 kg
CP-05	The system shall utilize non-toxic propellants

The rationale for CP-01 comes from the ΔV required for Earth escape and initial stabilization at Mars. The initial insertion orbit parameters are $\{a, e, i, \Omega, \omega, \theta\} = \{51526 \text{ km}, 0.8705, 0.01^\circ, 0^\circ, 0^\circ, 0^\circ\}$. The velocity at perigee is 10.57 km/s and the corresponding escape velocity is 10.93 km/s. Thus, the ΔV for escape is ~ 360 m/s, considering a theoretical impulsive maneuver. A 10% margin on ΔV is considered to include for gravity losses and other miscellaneous operational errors, thereby yielding a margined $\Delta V_{esc,mg}$ of 396 m/s. The

deceleration maneuver for initial stabilization after ballistic capture requires a ΔV_{stab} of 45 m/s. An additional $\sim 10\%$ margin is placed and the $\Delta V_{stab,mg}$ is 49 m/s.

Performance requirement CP-02 establishes a limitation on thrust and CP-03 establishes the maximum burn time. For a 32 kg spacecraft, this combination effectively distributes the ΔV required to escape Earth into multiple maneuvers for transfer time reduction and gravity loss control. A single burn maneuver to escape leads to a gravity loss of $\sim 23\%$, which is unacceptable in terms of operations and systems design (leads to a drastic increase of mass). A 1 mm thrust misalignment is considered, which is similar to LUMIO - a 12U lunar CubeSat mission [67]. The disturbance torque is 3 mNm with the maximum thrust. Reaction wheels sets with high maximum torque and momentum storage are utilised to compensate for the disturbance [68]. Thrust vectoring is also essential for controlling the momentum build-up. Additionally, maximum burntime limit is fixed to avoid excessive heat build-up in the thruster. The maximum mass requirement, CP-04, is constrained at 50% of the overall spacecraft mass for the combined chemical–electric propulsion system. Usage of green non-toxic propellants is required (CP-05) because the CubeSat is assumed to be a secondary payload and any damage to the primary spacecraft as well as any self-damage must be avoided. In addition to these, waivers on some of the traditional CubeSat requirements, like maximum pressure of 7 bar [14], are needed for executing the mission.

Chemical propulsion system selection is crucial since it has to be compatible with the MARIO mission. The design options explored are cold gas systems, solid rocket motors, liquid mono-propellant and bipropellant engines (section 2-2). A trade-off analysis is carried out to select the most pertinent system for MARIO application. The main criteria for trade-off are: thrust level, specific impulse, system mass, system complexity, control capabilities, reliability, and technology readiness level.

The thrust level provided by the propulsion system must meet CP-02 and the minimum value must be high enough to expedite Earth escape. Individual systems providing lower thrusts than 3 N can also be aggregated to provide a cumulative thrust that satisfies CP-02. Another option is to explore the possibility of controlling or limiting the thrust provided by some systems that have larger thrust capabilities. The specific impulse I_{sp} is another key trade-off criterion, since higher I_{sp} directly contributes to mass savings. The I_{sp} depends upon multiple factors such as propellant enthalpy, combustion characteristics, and thruster geometry. The system mass is influenced by the thrust, I_{sp} , and the materials in constructing the system. The complexity of the systems needs to be analysed since the CubeSat design philosophy has always focused on simplifying the system to reduce cost. The system must be easy to design, assemble, integrate and operate. The system must also have less modes of failure and must have a high degree of operational reliability. Multiple factors influence reliability and usually the more the components, the more is the risk of failure. Owing to mass savings, the MARIO mission follows a zero-redundancy policy and thus the propulsion system must operate with precision and without failure. Finally, since CubeSat design has traditionally involved the use of commercial off-the-shelf equipment, the technology readiness level (TRL) of the system type is also important. the TRL of the system plays an important role in highlighting the reliability by throwing light on the qualification status for space operations.

Table 2-5 illustrates the propulsion trade-off. Considering the systems discussed in section 2-2, the cold gas system is capable of producing the required thrust when aggregated. The I_{sp} is very low (< 80 s), which will lead to a very high system mass. Taking into account the

required ΔV and the I_{sp} , the system mass will be excessive for cold gas systems. They are however simple in architecture and have a very high degree of reliability. Additionally, they have a very rich flight heritage.

Solid rocket motors have very high thrust capabilities that result in large vehicle accelerations that may damage the structure. Apart from some digital solid microthruster arrays, there are no solid rocket motors that provide thrusts that are compatible with CP-02. The I_{sp} yield of solid rocket motors are moderately high (180–270 s). The higher end of the I_{sp} yield (270 s) corresponds to thrusters having ~ 250 N thrust. These systems can be packed compactly and the system mass is only partially compatible considering the ΔV requirements and the I_{sp} yield of systems with lower thrusting capability. The system architecture is fairly simple and does not involve any complex moving parts. Solid rocket motors do not have any start-stop capability and they burn continuously. Thus, for the MARIO application, multiple small scale systems should have to be installed and this increases the system mass and introduces operational complexities. All solid motors have unspecified inherent thrust misalignment due to the uncertainty in burn characteristics. Thus, the controllability and throttability of solid motors are extremely complicated.

Liquid monopropellant systems are capable of providing thrusts in the range of 0.3–1.5 N. This is highly suitable for MARIO applications since two thrusters could be aggregated to provide the required thrust. The I_{sp} yield of monopropellant thrusters that use non-toxic green propellants is high enough such that the propellant consumption for the required ΔV is compatible with the system mass requirements. Since the monopropellant systems are operated in either blow-down or pressure-regulated mode, there are check valves and flow control valves present in the feed system. Thus, they are relatively complicated in comparison with cold gas and solid motors. Owing to this complexity, the controllability of monopropellant systems has some uncertainties and requires some improvement for precise operations. Liquid monopropellant systems based on hydrazine and green propellants have flight heritage and have a high degree of reliability [53].

Liquid bipropellant systems also provide thrusts that are suitable for MARIO applications. Bipropellant systems that use highly concentrated H_2O_2 with ethanol/kerosene are capable of providing 1–1.5 N thrust [52, 65]. Other thrusters like HYDROS-C are capable of providing 0.4 N thrust [66]. Depending upon the individual thrust capabilities, a number of thrusters could be aggregated to provide the required overall thrust. Bipropellant systems have a very high I_{sp} yield, ~ 290 –315 s, and have excellent performance that leads to high mass savings. These performances make them compatible in terms of system mass for the required ΔV . However, bipropellant systems are incredibly complex to operate. In the case of pressure-fed bipropellant system, the pressures of oxidiser and the fuel need to be precisely controlled and maintained in order to achieve the optimal mixture ratios for efficient combustion and consequently for optimal performance. In cases where microturbopumps are used, the presence of the moving parts induces a high degree of uncertainty and increases the risk of failure manifold. Bipropellant feed system design and integration is extremely complicated for CubeSat applications and requires years of further development. The maturation of bipropellant systems for small satellite missions is very low and they are prone to valve failures and improper propellant mixing, thus posing an unacceptable risk to the mission.

Thus, the choice of the propulsion system is clear. The liquid monopropellant systems that utilise non-toxic green propellants have several advantages over the rest of the systems in terms

of thrust, I_{sp} , system mass, complexity, controllability, reliability, and technology readiness level. Additionally, the use of green propellants satisfies the non-toxicity requirement CP-05.

Table 2-5: Comparison of chemical propulsion systems

Criteria Options	Thrust level	I_{sp}	Mass	Complex- ity	Control	Reliabil- ity	TRL
Cold gas	<u>green</u> OK 0.9–2.36 N	<u>red</u> Very low <80 s	<u>red</u> Not compatible with required ΔV	<u>green</u> Simple system	<u>orange</u> Long duration burn difficult.	<u>blue</u> High	<u>green</u> 9
Solid	<u>red</u> Very high >35 N	<u>orange</u> Moderate 180–270 s	<u>orange</u> Partially compatible with required ΔV	<u>green</u> Simple system	<u>red</u> No start-stop capability. Unspecified thrust misalignment	<u>red</u> Prone to misfires	<u>orange</u> 6
Monopropellant	<u>green</u> OK 0.3–1.5 N	<u>green</u> High 220–250 s	<u>green</u> Compatible with required ΔV	<u>orange</u> Relatively complicated system	<u>orange</u> Pressure-feed control needs improvement.	<u>green</u> Good	<u>green</u> 9
Bipropellant	<u>green</u> OK 0.4–1.5 N	<u>blue</u> Very high 290–315 s	<u>green</u> Compatible with required ΔV	<u>red</u> Extremely complicated system	<u>red</u> Feed system development requires huge effort.	<u>red</u> Prone to failures in feed system	<u>orange</u> 4–5

blue Exceeds requirements green Meets requirements orange Correctable deficiencies red Unacceptable

2-4 Propellant properties and analysis

2-4-1 ADN-blends vs HAN-blends

The choice of propellant is extremely crucial to ensure high performance of the propulsion system. The most common propellant used in liquid monopropellant engine is hydrazine. Flight heritage of such systems is good and they have a high degree of reliability. However, most of the hydrazine propelled monopropellant systems have been used for attitude control applications in large satellites. These large satellite systems have high budgets and are rigorously designed with several safety checks. The handling of hydrazine propellant is done by several experts using advanced equipment. Hydrazine is highly toxic, corrosive, and probably carcinogenic [69]. Hydrazine is classified within hazard 1 class explosive materials and has restrictions on transportation.

CubeSat applications require non-toxic propellants due to several reasons. Firstly, CubeSats are secondary payloads and have different, often lenient, safety and design requirements compared to traditional large spacecraft. Such spacecraft shall be the primary payload and no primary contractor would want to give a ride to a secondary payload carrying corrosive propellant such as hydrazine, especially provided that there is a higher risk of leak. Secondly, the handling of non-toxic and low-volatile chemicals is easier, safer, and cheaper. Since CubeSats are developed by universities and small spacecraft consortia, the handling will be done by personnel with lesser experience. Thus, it is paramount to reduce health risks to those personnel. Finally, the recent developments in green propellants has shown that they have higher densities and lower environmental sensitivities compared to hydrazine. Hydrazine has

a density of 1.004 kg/m^3 at room temperature while the green propellants have densities in the range of 1238 to 1470 kg/m^3 . Since CubeSats are severely size constrained, higher density propellants are better suited to enhance storage capabilities [49].

To this extent, the propellants under consideration are blends of ADN - Ammonium dinitramide ($\text{NH}_4[\text{N}(\text{NO}_2)_2]$) and HAN - Hydroxylammonium nitrate (NH_3OHNO_3). Another possible consideration is the HTP - high test peroxide which is 87.5% H_2O_2 in water. However, in comparison with the ADN and HAN based propellants, the HTP is more volatile and less stable. ADN is a solid white salt with ammonia cation (NH_4^+) and dinitramide anion ($\text{N}(\text{NO}_2)_2^-$) which is readily soluble in water and other polar solvents [47]. HAN is an inorganic compound derived from hydroxylamine and nitric acid.

The blends of ADN considered are FLP-106 and LMP-103S while the blend of HAN considered is the AF-M315E. FLP-106 consists of 64.6% ADN, 23.9 % water and 11.5% Monomethylformamide - MMF ($\text{C}_2\text{H}_5\text{NO}$) [70]. LMP-103S consists of 63% ADN, 13.95% water, 18.4% Methanol, and 4.65% Aqueous Ammonia (25%), which is similar to FLP-106 [70]. The composition of AF-M315E remains classified as it was developed by the Air Force Research Laboratory (AFRL) of the United States Air Force. Some of the properties of these propellants are summarised in Table 2-6.

Table 2-6: Green propellant comparison

Property	LMP-103S	FLP-106	AF-M315E
Liquid phase density, ρ [kg/m^3]	1238	1357	1470
Specific impulse, I_{sp} [s]	251.5 ^a	258.2 ^a	257 ^b
Combustion temperature, \mathcal{T}_c [K]	1864.57 ^a	2133.4 ^a	2173 ^b
Saturation temperature, \mathcal{T}_s [K]	266.15	273.15	193.15
Acute Toxicity LD ₅₀ [mg/kg]	750	1270	550
Skin irritation	None	None	Slight
Corrosivity	None	None	Medium
pH Level	~7	~7	3.7–4
TRL	9	7	9
Export control	None	None	ITAR

^a Specific impulse and combustion temperature of LMP-103S and FLP-106 are calculated using NASA CEA with $P_c = 20\text{MPa}$ and $\varepsilon = 50$ (frozen).

^b AF-M315E properties are obtained from Werling et al [56] and Spores et al [57]. I_{sp} and \mathcal{T}_c could depend strongly upon the simulated conditions.

AF-M315E has the highest density (1470 kg/m^3) among the considered propellants, followed by FLP-106 (1357 kg/m^3) and LMP-103S (1238 kg/m^3) [49, 56]. In terms of I_{sp} , FLP-106 has the highest yield [56]. The calculations are performed for LMP-103S and FLP-106 using the NASA Chemical Equilibrium Analysis (CEA) code [71]. Chamber pressure P_c was set at 2 MPa and the nozzle expansion area ratio ε was set at 50 with frozen flow conditions at the nozzle exit. AF-M315E also has a significant I_{sp} yield while LMP-103S yields the lowest of the three. The compositions of LMP-103S and FLP-106 play a significant role in the determination of \mathcal{T}_c and I_{sp} . The values for AF-M315E are obtained from Werling et al [56] and Spores et al [57].

The saturation temperature of LMP-103S and FLP-106 are -7°C and 0°C , respectively. This is due to the water content in these blends. AF-M315E does not freeze but crystals are formed

at -80°C . The acute toxicity by the measure of LD_{50} (oral) - the mean lethal dose to kill half the members of a tested population - of LMP-103S, FLP-106 and AF-M315E are 750 mg/kg, 1270 mg/kg and 550 mg/kg, respectively; which signifies that AF-M315E has the highest toxicity among the considered green propellants [49, 72]. However, AF-M315E causes slight skin irritation upon contact and is acidic with a pH level of 3.7–4 [72]. AF-M315E is also corrosive and the main component HAN is unstable to acids, isocyanates, ketones etc. Also, HAN decomposition will be triggered if a prolonged contact is maintained with metals such as copper, iron, nickel and some other transition metals [72]. Thus, long term storage of AF-M315E is complicated and only a select set of materials can be used. Regarding the technology readiness level, LMP-103S already has flight heritage [53]. FLP-106 is yet to be flown but due to the similarity with LMP-103S, the TRL level is sufficiently high. Extensive testing of FLP-106 propellant has been pursued at the Deutsches Zentrum für Luft-und Raumfahrt, Lampoldshausen [54, 70, 73]. AF-M315E was used in the GR-1 and GR-22 propulsion systems flown on-board the Green Propulsion Infusion Mission (GPIM) ¹.

Considering the different properties, FLP-106 is chosen as the propellant for the chemical propulsion system for MARIO mission application. LMP-103S, although having flight heritage, has a lower density than FLP-106. Thus, FLP-106 can be stored in smaller propellant tanks, which is advantageous due to CubeSat size constraints. Additionally, FLP-106 is presumed to reach a high degree of maturation by 2024 [54, 74]. The I_{sp} yield of FLP-106 is higher than that of LMP-103S and AF-M315E, which leads to lower propellant mass for the required ΔV . The combustion temperature \mathcal{T}_c of AF-M315E is higher than that of FLP-106, which makes the design of the thrust chamber very expensive or even impossible since very few materials can withstand such heat. FLP-106 is much safer to handle due to its very low sensitivity, volatility, and neutral nature [47]. AF-M315E, due to its corrosive and acidic nature, will possibly decompose on prolonged contact with the feed pipes and valves which are usually made of steel, copper or nickel. FLP-106 is non-reactive to these metals. Finally, FLP-106 is not export controlled substance and is accessible unlike AF-M315E which is ITAR-restricted.

Thermochemical analysis of FLP-106 using the NASA Chemical Equilibrium Analysis (CEA) code is pursued to obtain the propellant performance [71]. As mentioned, FLP-106 consists of 64.6% ADN, 23.9 % water and 11.5% Monomethylformamide - MMF ($\text{C}_2\text{H}_5\text{NO}$) [70]. In the condensed phase, the heats of formation are: MMF $\Delta H_f^0 = -247.4$ kJ/mol [75], ADN $\Delta H_f^0 = -134.6$ kJ/mol [76], and Water $\Delta H_f^0 = -285.8$ [77]. At $P_c = 2$ MPa and area ratio $\varepsilon = 50$ with frozen flow conditions at the exit, the analysis yields an ideal vacuum specific impulse $I_{sp,vac} = 258.2$ s. Some key properties of FLP-106 and its performance are listed in Table 2-7.

2-5 Thruster performance and design

The thruster design is pursued with a target thrust of 3 N (CP-01). ADN-based thrusters providing 1 to 1.5 N thrust are currently under development [49, 53]. To provide the necessary thrust, two 1.5 N thrusters can be utilised.

¹Green Propellant Infusion Mission Fires Thrusters for the First Time https://www.nasa.gov/directorates/spacetech/home/tam/gpim_fires_thrusters_for_first_time. Last accessed: 10-Oct-2019

Table 2-7: Properties of FLP-106 and ideal performance prediction using NASA CEA at $P_c = 2$ MPa and $\varepsilon = 50$ (frozen)

Property	Value	Property	Value
Molecular mass, \mathfrak{M}	22.8 kg/kmol	Characteristic velocity, c^*	1361.7 m/s
Liquid phase Density, ρ	1357 kg/m ³	Thrust coefficient, C_F	1.7985
Saturation temperature, T_s	273.15 K	Ideal specific impulse, I_{sp}	258.2 s
Vapour pressure, P_{vap}	<21 mPa	Combustion temperature, \mathcal{T}_c	2133.4 K

The method of ignition and the ignition characteristics of the propellant play an important role in propulsion system design. Some studies utilize a hot catalytic bed for the decomposition of ADN [54]. The catalyst bed design is a complicated process and its analysis is out of the scope of this work. Wilhelm et al [73] have found that thermal ignition using a glowplug yields a stable flame and an acceptable ignition time for FLP-106 propellant. An exothermic reaction that corresponds to ADN decomposition starts at 150°C [78]. The ignition temperature of FLP-106 is between 150°C to 200°C.

The real performance of the thruster is calculated by first performing a thermochemical analysis using NASA CEA and then by including the necessary nozzle and combustion efficiencies. Thruster design is iterated until the required performance values are achieved. The chamber pressure, P_c , is maintained at 2 MPa, which yields a similar thrust performance to the HPGP thruster on-board PRISMA satellite [53].

In the set-up of the analysis in NASA CEA, first the P_c is set followed by the nozzle contraction area ratio ($\varepsilon_c = 50$) for a finite combustion chamber area and different nozzle expansion area ratios ($\varepsilon = 50, 100, 150, 200, 250, 300$) for a parametric analysis. The reactants and are defined and their corresponding amounts and formation enthalpies are specified. FLP-106 monopropellant is defined with the reactants ADN - 64.6%, Water - 23.9% and Monomethylformamide - 11.5%.

The important performance parameters calculated by CEA are combustion temperature \mathcal{T}_c , molecular mass of the combustion gas \mathfrak{M} , the specific heat ratio k , density of the combustion gas ρ_g , gas velocity v_g , ideal characteristic velocity c_{ideal}^* , ideal thrust coefficient $C_{F,ideal}$, and vacuum specific impulse I_{sp} [71]. The specific gas constant R_{gas} is calculated using the molecular mass \mathfrak{M} and the universal gas constant R .

A conical nozzle with a throat diameter, D_t , of 0.75 mm is utilised. From CEA calculations, the Reynolds number (Re) at the throat is ~ 15000 . For such Re values, the average nozzle efficiency η_n is 0.92 [27]. The combustion efficiency η_c is 0.95–0.99 for a well designed combustion chamber [27]. An average value of $\eta_c = 0.98$ is used. For $\varepsilon = 50$, application of these quality factors yields an I_{sp} of 232.8 s, which is considered low since it leads to a large propellant mass for the required ΔV . Thus, it is necessary to increase the ε to improve the performance.

The variations of I_{sp} and T with respect to the area ratio ε are studied to obtain the required performance and design parameters for the monopropellant thruster. The mass flow rate \dot{m} and subsequently the thrust are calculated using Eqs.(2-7)–(2-10) [27].

$$\dot{m} = \frac{A_t \cdot P_c \cdot k}{\sqrt{(k \cdot R_{gas} \cdot \mathcal{T}_c)}} \cdot \sqrt{\left(\frac{2}{k+1}\right)^{(k+1)/(k-1)}} \quad (2-7)$$

$$T = \dot{m} c^* C_F \quad (2-8)$$

$$C_F = \eta_n C_{F,ideal} \quad (2-9)$$

$$c^* = \eta_c c_{ideal}^* \quad (2-10)$$

The thrust and the specific impulse increase with the increase in area ratio, as illustrated in Figure 2-6. The value of $\varepsilon = 200$ is chosen for the design. The rationale being that the corresponding performance values satisfy thruster requirements and higher ε values yield only a small increase in performance while leading to higher material usage and thruster mass. Additionally, very high ε values could lead to higher divergence losses, thereby reducing nozzle efficiency [27]. Thruster performance parameters for $\varepsilon = 200$ are listed in Table 2-8.

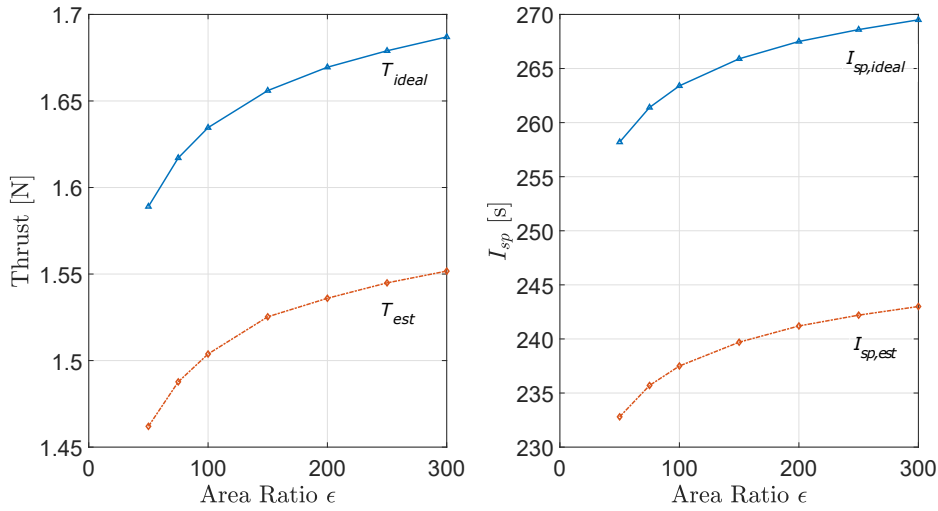


Figure 2-6: Ideal and estimated thrust T and specific impulse I_{sp} variation with area ratio (ε). Total efficiency $\eta_{tot} = 0.9016$

Table 2-8: Estimated thruster performance for $\varepsilon = 200$ using NASA CEA

Property	Value	Property	Value
Combustion efficiency, η_c	0.98	Characteristic velocity, c^*	1334.47 m/s
Nozzle efficiency, η_n	0.92	Thrust coefficient, C_F	1.7383
Max Thrust (per thruster)	1.536 N	Mass flow rate (per thruster), \dot{m}	0.673 g/s
Specific Impulse, I_{sp}	241.2 s	Exhaust velocity, v_e	2366.17 m/s
Chamber temperature, \mathcal{T}_c	2133.4 K		

A finite area combustion chamber with a nozzle contraction ratio ε_c of 50 is used. It is the ratio between the combustion chamber cross sectional area A_c and the nozzle throat area A_t .

and the constriction length $L_{con} = 1.5$ mm is chosen as a preliminary design value to achieve a 45° constriction angle. Since $A_t = \pi D_t^2/4$, and D_t is already known, the combustion chamber diameter D_c is directly calculated using ε_c .

Combustion chamber volume V_c is calculated in several steps. First, the specific volume at the throat $V_{s,t}$ is calculated using equation (2-11).

$$V_{s,t} = \frac{A_t \sqrt{k R_{gas} \mathcal{T}_c}}{\dot{m}} \quad (2-11)$$

Here, $\sqrt{k R_{gas} \mathcal{T}_c}$ corresponds to the sonic velocity at the throat, v_t . The mass flow rate \dot{m} is obtained from equation (2-7) and the combustion temperature \mathcal{T}_c is obtained from the thermochemical analysis. Then, with $V_{s,t}$, the specific volume at the combustion chamber is calculated using equation (2-12)

$$V_{s,c} = \frac{V_{s,t}}{\left(\frac{k+1}{2}\right)^{\left(\frac{1}{k-1}\right)}} = \frac{A_t \sqrt{k R_{gas} \mathcal{T}_c}}{\dot{m}} \left(\frac{2}{k+1}\right)^{\left(\frac{1}{k-1}\right)} \quad (2-12)$$

Now, the characteristic length L^* and the chamber residence time t_s are defined using equations (2-13) and (2-14)

$$L^* = \frac{V_c}{A_t} \quad (2-13)$$

$$t_s = \frac{V_c}{\dot{m} V_{s,c}} \quad (2-14)$$

Now, combining equations (2-12), (2-13) and (2-14), we get an expression for the total combustion chamber volume that is expressed using equation (2-15) [27].

$$V_c = t_s \dot{m} V_{s,c} = t_s A_t \sqrt{k R_{gas} \mathcal{T}_c} \left(\frac{2}{k+1}\right)^{1/(k-1)} \quad (2-15)$$

$$(2-16)$$

The total combustion chamber volume is the sum of the volumes of the cylindrical part and the contraction frustum (equation (2-17)).

$$V_c = A_c L_c + A_c L_{con} \left(1 + \sqrt{\frac{A_t}{A_c}} + \frac{A_t}{A_c}\right) \quad (2-17)$$

Here, A_c is the combustion chamber cross sectional area. The second term on the right is the volume of the frustum. Since V_c is calculated using equation (2-15), the combustion chamber length is calculated by rearranging equation (2-17) into equation (2-18).

$$L_c = \frac{V_c}{A_c} - L_{con} \left(1 + \sqrt{\frac{A_t}{A_c} + \frac{A_t}{A_c}} \right) \quad (2-18)$$

Characteristic length $L^* = 1.5$ m is used which in turn yields the maximum combustion performance [54, 73]. The corresponding residence time $t_s = 0.0026$ s. The nozzle is designed by assuming a $\alpha_d = 15^\circ$ half expansion angle. The length of the divergent part of the nozzle L_N is calculated using equation (2-19).

$$L_N = \frac{(\sqrt{\varepsilon} - 1) \cdot \frac{D_t}{2} + R_u \cdot \left(\frac{1}{\cos \alpha} - 1 \right)}{\tan \alpha_d} \quad (2-19)$$

Here, R_u is the throat longitudinal radius which is $\sim 1.5 \times R_t$ [79]. The chamber and nozzle design parameters are listed in Table 2-9. The thrusters are placed outside the 16U spacecraft structure.

Table 2-9: Monopropellant thruster design parameters

Parameter	Value	Parameter	Value
Thrusters	2	Throat diameter, D_t	0.75 mm
Chamber pressure, P_c	2 MPa	Contraction ratio, A_c/A_t	50
Chamber volume, V_c	662.7 mm ³	Expansion area ratio, ε	200
Chamber diameter, D_c	5.3 mm	Expansion half angle, α	15°
Chamber residence time, t_s	0.0026 s	Nozzle length (divergent), L_N	18.47 mm
Chamber length, L_c	28.26 mm	Thruster mass (total), $m_{thruster}$	0.4 kg ^a

^a Value assumed based on state-of-the-art 1N monopropellant thrusters without valves Ariane Group - <http://www.space-propulsion.com/brochures/hydrazine-thrusters/hydrazine-thrusters.pdf> Last accessed: 04-April-2019

2-6 High-thrust trajectory analysis

Spacecraft trajectory is calculated by assuming a 2-body problem, discarding perturbations, and integrating the equations of motion with the calculated thruster performance and the injection orbit as input. The goal of the trajectory analysis is to find a) required burntime (t_b) for each maneuver, b) total number of maneuvers required to achieve Earth escape with the lowest flight time, c) the overall ΔV imparted to the spacecraft, and d) the overall propellant mass consumed.

The injection orbit has a perigee altitude of 295 km and an apogee altitude of 90000 km. Thus, the eccentricity of the orbit is 0.87. The assumed initial orbital parameters are $\{a, e, i, \Omega, \omega, \theta\} = \{51526 \text{ km}, 0.8705, 0.01^\circ, 0^\circ, 0^\circ, 0^\circ\}$. The orbit raising and Earth escape trajectory is split into two parts, the powered flight and the ballistic flight. The powered flight is when the thrust is applied over a specific value of the burntime t_b and the ballistic flight is when no thrust is applied. The burn manoeuvres are performed near perigee for efficient and swift orbit raising. The t_b remains constant for all manoeuvres and the thrust is initiated at $t_b/2$ before perigee and ends at $t_b/2$ after perigee. This is done so because it is prudent to perform

the burn manoeuvres closest to the perigee point. Since the manoeuvres are real rather than impulsive, the burn should begin just before perigee and end just after perigee. This also reduces the gravity losses.

The thruster performance values of $T = 3$ N (CP-01) and $I_{sp} = 241.2$ s are utilised. The total time until escape depends upon the thrust and burntime. A grid search is done to calculate the t_b for each maneuver based on the lowest overall flight time (powered and ballistic) until Earth escape. The sampled values of t_b for each maneuver range from 400 to 600 seconds. Each successive burn increases the apogee and the integration of equations of motion is performed until Earth escape ($e = 1$) is achieved. They are expressed in equations (2-20)– (2-22).

$$\frac{d\vec{r}}{dt} + \frac{\mu}{r^3}\vec{r} = \frac{\vec{T}}{m} \quad (2-20)$$

$$\frac{dm}{dt} = -\frac{|T|}{I_{sp} g_0} \quad (2-21)$$

$$\vec{T} = u T_{max} \frac{\vec{v}}{\|\vec{v}\|} \quad (2-22)$$

Here, r is the radius vector, μ is the gravitational parameter of Earth, and m is the spacecraft mass. In equation (2-22), the quantity u denotes the throttle control, which is either 1 or 0 depending whether the thrust is applied or not. The quantity $v/\|v\|$ indicates the direction of thrust along the velocity vector. The maximum thrust $T_{max} = 3$ N.

The calculated t_b for each maneuver is 598.6 s such that overall flight time is kept to the minimum. The minimum total flight time $P = 792.73$ hours (~ 33.03 days) . This flight time is counted as the Earth orbiting time until eccentricity $e = 1$, and not the time to reach the Earth sphere of influence. The total number of maneuvers is 6 and the escape is achieved at the 7th orbit. The number of Van Allen belt crossings amount to 13. The orbital raising is illustrated in Figure 2-7. An additional ~ 30 days coasting period could be considered for reaching the Earth sphere of influence.

The calculated cumulative ΔV_{esc} of the orbit raising and escape maneuvers is 363.14 m/s, which is ~ 3 m/s higher than the ideal ΔV for escape. This difference corresponds to the accumulated gravity losses ($\Delta V_{gl} \sim 1\%$). A 10% margin is placed on the ideal ΔV for contingency and $\Delta V_{esc,mg}$ is 396 m/s. Using equation (2-6), the propellant mass is calculated. The propellant mass ($m_{p,mg}$) pertaining to $\Delta V_{esc,mg}$ is 4.993 kg while the m_p for ΔV_{esc} is 4.553 kg.

The stabilization manoeuvre is executed after low-thrust heliocentric transfer and ballistic capture. The $\Delta V_{stab} = 45$ m/s and a 10% margin is again placed for contingency, thus making $\Delta V_{stab,mg} = 49$ m/s. The propellant mass $m_{p,stab} = 0.418$ kg and the margined value $m_{p,stab,mg} = 0.459$ kg. A 5% margin is placed on the cumulative margined propellant masses for Earth escape and Mars stabilization to account for the RCS thruster operations, i.e., $m_{p,rsc} = 0.05 \times (m_{p,mg} + m_{p,stab,mg})$. Thus, the overall chemical propellant mass is 5.725 kg.

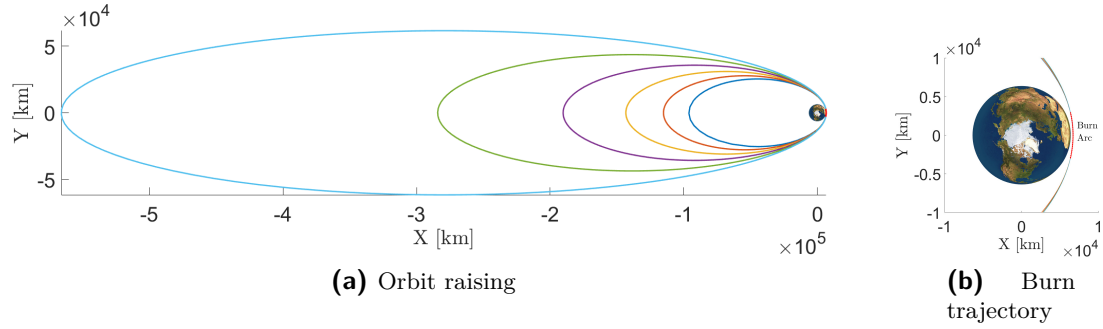


Figure 2-7: MARIO orbit raising and escape - ballistic and burn trajectories

Table 2-10: Mission parameters for orbit raising and escape

Parameter	Value	Parameter	Value
Initial Mass, m_i	32 kg	Propellant mass (real), m_p	4.553 kg
Thrust, T	3 N	Propellant mass (margin), $m_{p,mg}$	4.993 kg
Specific Impulse, I_{sp}	241.2 s	Final mass at Earth escape, $m_{f,esc}$	27.447 kg ^a
Burn Time per maneuver, t_b	598.6 s	Mars stabilization ΔV_{stab}	45 m/s
Orbit raising maneuvers	6	Margined $\Delta V_{stab,mg}$ ($\sim 10\%$)	49 m/s
Ideal ΔV_{esc}	359.66 m/s	Propellant mass for ΔV_{stab}	0.418 kg
Real ΔV_{esc}	363.14 m/s	Propellant mass for $\Delta V_{stab,mg}$	0.459 kg
Margined $\Delta V_{esc,mg}$ (10% margin)	396 m/s	Propellant mass for RCS, $m_{p,rCS}$	0.273 kg
		Overall propellant mass, $m_{p,mg,ovr}$	5.725 kg

^a Calculated based on the real m_p and not the margin.

2-7 Feed system design and system sizing

The feed system consists of the storage tanks, valves, flow lines, and the tank pressurization system. The overall margin propellant mass $m_{p,mg,ovr} = 5.725$ kg for the monopropellant system with an $I_{sp} = 241.2$ s. Considering the liquid phase density of FLP-106 at room temperature (see Table 2-7), the total propellant volume is 4218.6 cm^3 , which in terms of CubeSat units is ~ 4.2 U.

A regulated pressure-fed system is utilised as the thrust must be precise and constant [80]. Gaseous nitrogen GN_2 is used as the pressurant. A pressurized propellant tank requires a spherical shape or a cylindrical shape with spherical or ellipsoid dome ends to be safe as the pressure is effectively distributed without causing severe stress points along the structure. However, for a 4218.6 cm^3 tank, the radius of the spherical tank will be ~ 9.62 cm, which leads to spatial accommodation issues in a 16U CubeSat. Thus, cylindrical tanks with spherical or ellipsoid dome ends are considered.

Most common type of ellipsoid is the *oblate ellipsoid*. It looks like a standard spherical dome with a circular base but it looks like it is 'squashed' a little from the top, i.e., the sides are more vertical and the top is flatter compared to a spherical dome. Eventhough there is a minor increase in stress along the walls, the main advantage of ellipsoid dome over a spherical dome is that for the same volume, there is more headroom along the vertical axis. This directly contributes to space saving and allows for easier accommodation within the CubeSat structure.

The propellant tank consists of the cylindrical part and the ellipsoid dome. The volume of the oblate ellipsoid dome is calculated using equation (2-23) and the volume of the cylindrical part is given by equation (2-24)

$$V_{dome} = \frac{4}{3} \pi b a^2 \quad (2-23)$$

$$V_{cyl} = \pi r^2 h \quad (2-24)$$

$$V_{tank} = V_{cyl} + V_{dome} \quad (2-25)$$

Here, the quantities a and b are semi-major and semi-minor axes, respectively. The semi-major axis a corresponds directly to the radius of the cylindrical part r and the semi-minor axis is adjustable. The quantity h represents the height of the cylindrical part. The total tank volume V_{tank} must accommodate the total propellant volume V_{prop} and also include an ullage volume for gas pressurisation. The tank diameter and height are iterated until the required V_{tank} is achieved.

Assuming a $\sim 10\%$ ullage volume, one large tank with 17 cm diameter would have a height of 22.8 cm. To save space and to accommodate rest of the feed system components, four tanks each with a diameter of 9.4 cm are be used. This also helps in reducing the propellant sloshing that occurs with larger tanks. Each tank has a capacity of 1160.1 cm^3 a height of 18.05 cm, occupying $\sim 1.8\text{U}$ space. These tanks are similar to the storage cell designs by Eagle Picher Technologies [81]. The tanks shape and their assembly in the spacecraft structure are illustrated in Figure 2-8.

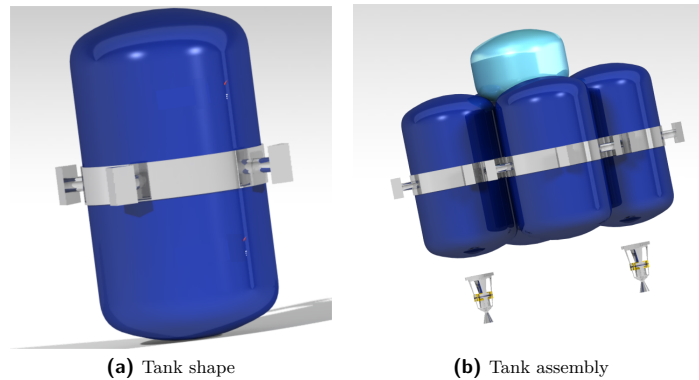


Figure 2-8: Propellant tank shape and assembly. The dark blue tanks hold the propellant and the light blue tank holds the pressurizer gas. The thrusters are placed outside the spacecraft structure.

The nominal feed pressure P_{feed} is set at 2.2 MPa and the Maximum Expected Operational Pressure (MEOP) is 2.6 MPa. The feed pressure value is similar to the one for a high-performance ADN-based monopropulsion system on-board PRISMA satellite [53]. A burst factor of 1.5 is applied on the MEOP to obtain the burst pressure, which is 3.9 MPa. The pressurant gas (GN_2) pressure P_{gas} is considered to be 28 MPa at 323 K, at which the

density $\rho_{gas} = 257.8 \text{ kg/m}^3$ [62]. The amount of pressurant gas required is calculated using equation (2-26).

$$m_{gas} = P_{feed} \left(\frac{N_{tank} V_{tank}}{R_{gas} T_{gas,low} - \frac{P_{feed}}{\rho_{gas}}} \right) \quad (2-26)$$

Here, N_{tank} is the number of propellant tanks, R_{gas} is the specific gas constant for GN_2 , and $T_{gas,low}$ is the lower limit for the temperature of the gas. The pressurant gas volume is calculated using equation (2-27). The internal volume of the pressurant gas tank is the same as the actual pressurant gas volume.

$$V_{gas,tank} = \frac{M_{gas}}{\rho_{gas}} \quad (2-27)$$

The pressurant gas tank is designed using the same formula used for the propellant tank design. The total gas tank volume $V_{gas,tank}$ is 492 cm^3 . The radius of the pressurant gas tank $r_{gas,tank}$ is 4.7 cm and the height $h_{gas,tank}$ is 7.76 cm.

The material used for the tank is Titanium alloy Ti-6Al-4V. Its yield strength is 880 MPa and density is 4430 kg/m^3 [82]. It has a very high corrosion resistance. The tank wall thickness is calculated for the burst pressure with a safety factor (SF_{ys}) of 1.2 applied on the yield strength [79]. An additional safety factor (SF_{th}) of 2 is applied on the thickness considering launch loads and vibration. The thickness of each tank is calculated using equation (2-28).

$$th = P_{burst} \frac{r}{\sigma_{yield}} SF_{th} SF_{ys} \quad (2-28)$$

The thickness of each propellant tank is 0.5 mm and that of the pressurant gas tank is 4.5 mm. Precision machining techniques applied on Ti-6Al-4V enable the manufacturing of tanks with small thicknesses [83]. The total mass of each tank is calculated by multiplying the material density ρ_{mat} with the difference between external and internal volumes of the tank. The external volume is calculated using equation (2-25) with the thickness added to the tank's internal radius. This is expressed in equation (2-29)

$$m_{tank} = \rho_{mat} (V_{tank,ext} - V_{tank}) \quad (2-29)$$

The design of valves, regulators, and filters are not presented in this work and is left for future research when the MARIO mission attains further maturity. The major components of the monopropellant thruster system are illustrated in Figure 2-9. The feed system design characteristics are listed in Table 2-11.

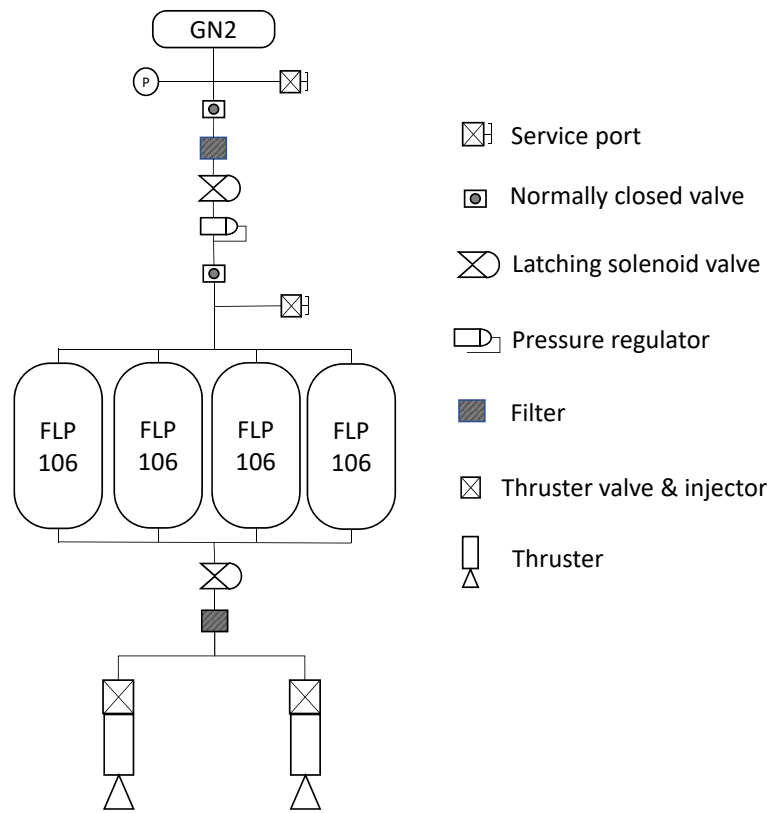


Figure 2-9: Schematic of the monopropellant thruster system

Table 2-11: Monopropellant system design parameters

Parameter	Value	Parameter	Value
Propellant tanks	4	Press. gas mass, m_{gas}	0.127 kg
Individual tank volume, V_{tank}	1160.1 cm ³	Press. tank volume, $V_{gas,tank}$	492 cm ³
Prop. feed pressure, P_{prop}	2.2 MPa	Press. tank radius, $r_{gas,tank}$	4.7 cm
Prop. tank burst pressure, $P_{prop,burst}$	3.9 MPa	Press. tank height, $h_{gas,tank}$	7.76 cm
Prop. tank radius, $r_{prop,tank}$	4.7 cm	Press. tank thickness, $th_{gas,tank}$	4.5 mm
Prop. tank height, $h_{prop,tank}$	18.05 cm	Press. tank mass, $m_{gas,tank}$	0.238 kg
Prop. tank thickness, $th_{prop,tank}$	0.50 mm	Feed pipes & valves mass, m_{fv}	0.20 kg
Total tank mass, m_{tank}	0.219 kg	Feed system total mass, m_{feed}	0.784 kg ^a
Press. gas pressure, P_{gas}	28 MPa	Feed system total volume	8U ^b
Overall propulsion system mass, $m_{cp,sys}$	6.91 kg ^c		
Overall volume, $V_{cp,sys}$	8U		

^a Feed system mass includes pressurant gas mass but not propellant mass

^b Includes volumes of propellant tank, pressurant gas tank, valves, and pipes. Thrusters are placed outside the spacecraft structure.

^c Overall propulsion mass includes the feed system mass, the thruster mass and the propellant mass (from Table 2-8).

Chapter 3

Electric propulsion

In this chapter, first the electric propulsion principles are discussed followed by a state-of-the-art review of electric propulsion systems applicable to CubeSats. Then, systems design strategy, propellant analysis, thruster performance model, low-thrust trajectory analysis, and systems design are presented. The content presented in this chapter is partially based on the published work of the author: Mani et al *Combined Chemical–Electric Propulsion for a Stand-Alone Mars CubeSat* [28], Mani et al *Dual chemical-electric propulsion systems design for interplanetary cubesats* [29], and Mani et al *Electric propulsion characterization for a stand-alone Mars CubeSat* [84].

3-1 Electric propulsion principles

Electric Propulsion (EP) Systems are high specific impulse systems that have high propellant mass utilisation efficiency to produce the required change in velocity, ΔV . Owing to this feature, they occupy a smaller volume and have lesser mass compared to the conventional Chemical Propulsion (CP) systems, thereby leaving room for improving the payload characteristics and other critical subsystems' features in space missions.

EP systems were first developed in the 1960s in the former Soviet Union when plasmas were discovered to be a valuable source for production of current and subsequently thrust force. The SERT-1 spacecraft, in 1964, carried on-board the first demonstrable EP system, an ion thruster, and the Zond-2 spacecraft carried a pulse plasma thruster (PPT) [85]. EP systems have seen a rapid development since then.

Interplanetary missions, especially during the deep-space cruise phase, require a large total impulse. The total impulse is given by $I_t = \int_{t_0}^{t_f} T dt$, where T is the thrust and dt represents the burning time. Specific impulse I_{sp} is the total impulse I_t divided by the propellant mass m_p . To satisfy the large total impulse requirements, there is a need to increase the I_{sp} rather than m_p . Otherwise, the initial mass fraction would be enormous.

The ideal motion of a spacecraft with on-board EP system is governed by momentum conservation principle. A spacecraft of mass m moving at a velocity \vec{v} and subject to an external force \vec{F} has an equation of motion (for variable mass):

$$\vec{F} + \frac{dm}{dt}\vec{v}_e = \vec{F} + \dot{m}\vec{v}_e = m\frac{d\vec{v}}{dt} \quad (3-1)$$

Here, \dot{m} is the rate of change of spacecraft mass which is equivalent to the rate of change in propellant mass \dot{m}_p , v_e is the exhaust velocity of the expelled propellant, and t represents time. The thrust, which is the force acting on the spacecraft due to the ejection of propellants, is given by

$$\vec{T} = \dot{m}_p\vec{v}_e \quad (3-2)$$

Assuming impulsive thrust, i.e., exhaustion of propellants in a negligible duration with a constant propellant exhaust velocity v_e and neglecting external forces, the equation of rocket / spacecraft motion becomes,

$$\Delta V = v_e \ln \left(\frac{m_o}{m_o - \dot{m}_p t_b} \right) \quad (3-3)$$

Equation (3-3) is famously known as Tsiolkovsky Rocket Equation. Here, m_o represents the initial mass, t_b is the burning time, and Δv is the total change in velocity. Also, $m_o - \dot{m}_p t_b$ is the final mass of the spacecraft after the exhaustion of propellants, m_f . Rearranging (3-3), we get

$$\frac{m_f}{m_o} = e^{-\Delta v/v_e} \quad (3-4)$$

The Δv for interplanetary missions are very high and the v_e needs to be similar to the Δv to have a significant amount of useful mass that is transportable. As the mission analysis includes more complex physics such as orbital perturbations, thrust vectoring, staging etc., during interplanetary travel, the requirement on Δv increases. This eventually leads to the a large v_e requirement.

We can obtain higher v_e values by combusting propellants with high calorific value (energy per unit mass) and then accelerating them through a nozzle or by applying high body forces on the propellant stream to accelerate them.

In CP systems, propellants are mixed, ignited (either using an ignitor or by hypergolic chemical reaction), combusted, and accelerated through a convergent-divergent nozzle to produce thrust. The exhaust velocities of CP systems are limited by the chemical energy of the combustible mixture, heat transfer to nozzle throat and/or combustion chamber, and frozen flow losses. The maximum theoretical v_e attainable using CP, which require the usage of very rare bi/tri-propellant mixtures, is 5500 m/s [86]. However, storage and handling of such propellants are very complicated. Another issue is the heat energy produced by the combustion of the propellants is sometimes much higher than the acceptable structural material limits. Additionally, the combustion products are extremely corrosive and pose a great danger to the satellite structure. Even the best performing CP systems might not provide sufficient v_e to support interplanetary missions.

The peculiar feature of EP systems is that a large amount of externally stored energy, e.g. solar energy, is transferred to the propellant and thus results in very high exhaust speeds and energy densities. For example, in one of the methods, solar energy is converted to electrical energy to either provide heat to the propellants or produce an electric field along the ionised propellant stream, which results in acceleration [87]. High exhaust velocities correspond to low propellant consumption. Thus, EP systems are the most effective propulsion systems to be utilised for long duration, high total impulse interplanetary transfer missions. The main drawback of EP systems is the low thrust level, which depends upon the power production capabilities.

Specific impulse is a figure of merit of a thruster's performance since it is a measure of its efficiency in terms of fuel consumption. It is defined as the ratio of thrust to the rate of propellant consumption. Alternatively, it is defined as the total impulse divided by the propellant mass.

The total impulse is the integral of the the thrust over the operating duration.

$$I = \int_{t_0}^{t_f} T(t) dt = \int_{t_0}^{t_f} \dot{m}_p v_e dt \quad (3-5)$$

The specific impulse, defined in terms of weight at the surface of the Earth, is then given by the formula,

$$I_{sp} = \frac{\int_{t_0}^{t_f} T(t) dt}{g_0 \int_{t_0}^{t_f} \dot{m}_p dt} = \frac{I}{g_0 m_p} = \frac{T}{g_0 \dot{m}_p} \quad (3-6)$$

From (3-6), it can be observed that the higher the I_{sp} , the lower is the propellant consumed to produce the same level of total impulse.

In electrostatic and electromagnetic EP devices, the atoms/molecules of the injected propellant, which is in solid, liquid or gaseous form, need to be converted into ions for them to be accelerated through. The fraction of stored propellant is transformed into ions, which eventually are accelerated to a high velocity to produce thrust. The thrust produced by a singly-charged ion beam is

$$T = \dot{m}_i v_i \quad (3-7)$$

where \dot{m}_i is the ion mass flow rate and v_i is the exhaust velocity of the ions. Since the energy is conserved and that each ion carries a charge, the ion beam velocity is expressed as

$$v_{beam,i} = \sqrt{\frac{2 q_e V_{grid}}{\mathfrak{M}}} \quad (3-8)$$

where V_{grid} is the voltage through which the ion beam is accelerated, q_e is the electron charge, and M is the propellant atomic mass. The ion mass flow rate, which is related to the beam current I_{beam} is given by,

$$\dot{m}_i = \frac{I_{beam} \mathfrak{M}}{q_e} \quad (3-9)$$

Thus, the thrust for singly-charged ions is represented in equation (3-7) becomes,

$$T = \sqrt{\frac{2\mathfrak{M}}{q_e}} I_{beam} \sqrt{V_{grid}} \quad (3-10)$$

The ionisation process of the injected propellant molecules, until now, is assumed to be full, i.e, all the injected molecules are ionised. However, that might not be the case in reality [88]. This leads to the definition of a parameter called the *mass utilisation efficiency*, η_m . The mass utilisation efficiency, which represents the fraction of ionised atoms/molecules to the injected amount is given by the equation (3-11)

$$\eta_m = \frac{\dot{m}_i}{\dot{m}_p} = \frac{I_{beam}}{q_e} \frac{\mathfrak{M}}{\dot{m}_p} \quad (3-11)$$

Here, \dot{m}_p is the injected propellant mass flow rate. These ions have an elementary charge $q_e = 1.602 \times 10^{-19}$ Coulomb. The expression for the specific impulse needs to take into account the mass utilisation efficiency η_m and the correction for multiple charging.

$$I_{sp} = \eta_m \frac{v_i}{g_0} = \frac{\eta_m}{g_0} \sqrt{\frac{2 q_e V_{grid}}{\mathfrak{M}}} \quad (3-12)$$

The mass utilisation efficiency is a fairly difficult parameter to measure and accurately determine. Thus, a more useful efficiency parameter is defined, called *thruster efficiency* which is a better representative of the thruster performance. It enables us to make comparisons among different EP systems. It is the ratio of jet power produced by the thruster and the total input electric power to the thruster.

$$\eta_{tot} = \frac{P_{jet}}{P_{t,elec}} = \frac{\dot{m}_p v_e^2}{2P_{t,elec}} = \frac{T^2}{2\dot{m}_p P_{t,elec}} \quad (3-13)$$

The thruster's input electrical power, input mass flow rate, and the thrust output need to be measured to calculate η_{tot} . The jet power, P_{jet} is the kinetic thrust power of the beam, equivalent to $\dot{m}_p v_e^2/2$ or $T^2/2\dot{m}_p$.

Since the ions need to be produced in the chamber using the input electrical power, an electrical efficiency term is also defined. The electrical efficiency of the thruster is the ratio of the beam power and the total input power. It is represented in equation (3-14).

$$\eta_e = \frac{P_{beam}}{P_{t,elec}} = \frac{I_{beam} V_{grid}}{I_{beam} V_{grid} + P_{other}} \quad (3-14)$$

where P_{other} represents the other power required to produce the beam. This includes the electrical power to produce ions, cathode heater, and grid currents in ion thrusters etc [88]. The beam voltage is represented by V_{grid} .

The total thruster efficiency η_{tot} is influenced by the electrical efficiency η_e and the mass utilisation efficiency η_m . The total thruster efficiency is accurately calculated, in the case of ion thrusters, from the electrical and gas flow input parameters (known). The ion thrusters

are nearly mono-energetic and their exhaust velocities are calculated from the net acceleration voltage supplied to the thruster, while the beam current is measured by the high voltage power supply.

The total thruster efficiency can be expressed in terms of electrical efficiency and mass utilisation efficiency.

$$\eta_T = \frac{\eta_m v_i T}{2 \dot{m}_i P_{t,elec}} = \eta_m \frac{I_{beam} V_{grid}}{P_{t,elec}} = \eta_m \eta_e \quad (3-15)$$

3-1-1 Power constraint

The limiting factor in electric propulsion is the power supply, which is a critical resource. The EP systems have a very low Thrust-to-Mass ratio, nominally in the order of $\approx 10^{-3}$ N/kg. The power production and supply system also has a mass that becomes critical. Ideally, the higher the power production the higher is the exhaust velocity of the EP system. However, designing an over-productive power system leads to a formidable increase in power system mass, which then commutates the mass savings that we obtain from using EP systems. The power production, conversion efficiency, system mass, v_e , I_{sp} , thrust etc. need to be carefully optimised to maximise the performance and satisfy the mission requirements.

The power requirement of the system directly influences the power system mass and consequently the I_{sp} . Assuming a linear variation between power and power system mass along with constant conversion efficiency (from electric power to thrust power), we get

$$m_{pow} = K P_{t,elec} = \frac{KT v_e}{2\eta_e} = \frac{K g_0 T I_{sp}}{2\eta_e} \quad (3-16)$$

where K is the powerplant specific mass, i.e., electric propulsion system mass \div thruster input power.

Figure 3-1 illustrates the dependence of propellant mass (m_{prop}) and power system mass (m_{pow}) on the specific impulse when a constant thrust is considered. There is a need to balance the power system and propellant masses that shall minimise the sum of those masses. A corresponding specific impulse for the minimised combined mass will be the optimal value. This optimal I_{sp} depends upon K , η , and duration of thrusting Δt . However, it is independent of the thrust.

$$\hat{I}_{sp} = \frac{1}{g_0} \left(\frac{2\eta_e}{K} \right)^{1/2} \quad (3-17)$$

A critical parameter is the thrust-to-input power ratio. It is expressed as,

$$\frac{T}{P_{t,elec}} = \frac{T \eta_e}{P_{beam}} \quad (3-18)$$

Since the beam power P_{beam} is the product of beam current I_{beam} and beam voltage V_{grid} , the equation (3-18) becomes,

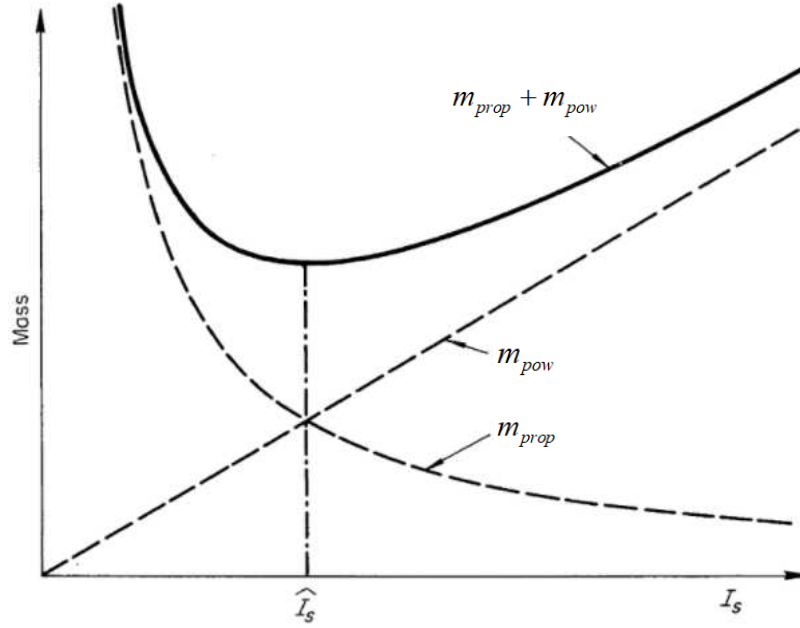


Figure 3-1: Dependence of propellant mass m_{prop} and power supply mass m_{pow} on specific impulse I_{sp} for a constant thrust mission. Image retrieved from Jahn [87]

$$\frac{T}{P_{t,elec}} = \frac{2\eta_m \eta_e}{g_0 I_{sp}} = \frac{2\eta_e}{g_0 I_{sp}} \quad (3-19)$$

With varying conversion efficiency, thrust, specific impulse, and external mass contributions, the optimisation procedure could broaden and become more detailed. Emphasis is placed on the influence of power supply system mass on the performance of electric propulsion system since it is one of the most critical parameters. Operating the thruster at too high or too low I_{sp} will reduce payload capacity. Development of power plants with low specific mass is as important as the development of thrusters with high specific impulse.

The power-to-mass ratio, ξ is the reciprocal of the powerplant specific mass, K . The exhaust velocity and the thrust depend upon the power-to-mass ratio [89]

$$T = \sqrt{\frac{2\eta_{tot} \xi m_p m_{pow}}{t_p}} \quad (3-20)$$

Here, m_p is the propellant mass, m_{pow} is the power plant mass, and t_p is the thrust duration. If the thrust needs to be increased, the power system mass also needs to be increased (since more power is required to be produced). The Tsiolkovsky's rocket equation is then altered to fit the narrative of the electric propulsion system to provide more robustness [90]

$$\Delta V = v_e \ln \left(1 + \frac{2 \eta_{tot} \xi t_p}{2 \eta_{tot} \xi t_p \left(\frac{m_s}{m_p} \right) + \eta_m^2 v_e^2} \right) \quad (3-21)$$

The quantity m_s refers to the structural mass of the entire satellite, including the payload and the exhaust velocity v_e is an independent variable.

$$\frac{m_{pow}}{m_p} = \frac{v_e^2}{2 \eta_m \xi t_p} \quad (3-22)$$

One very important factor to consider is the utility of the said power system after its utilisation by the electric propulsion system. It is prudent to pursue an power system design considering the power requirements of the rest of the subsystems in addition to the propulsion system such that we do not over-design it.

3-2 CubeSat electric propulsion state-of-the-art

Electric propulsion could be broadly classified into three main categories,

1. ***Electrothermal propulsion*** : heating of propellant gas and expansion through a nozzle.
2. ***Electrostatic propulsion*** : ionisation of propellant gas atoms and subsequent acceleration through application of electric body forces using an electric field.
3. ***Electromagnetic propulsion*** : acceleration of ionised propellant stream by the interactions of magnetic fields and with electric field applied orthogonally.

Electrothermal propulsion involves the heating of propellants to hot neutral or ionised gas in the thrust chamber and their subsequent acceleration through a convergent-divergent nozzle to produce thrust. The heat energy to the propellant is provided by the external power source. The means of supply of the energy are: a) passing the propellant over an electrically heated surface (*resistojet*), b) passing the propellant through an arc discharge (*arcjet*), and c) high frequency excitation of the propellant. The process is similar to chemical propulsion, however without any combustion. Thus the principles of gas dynamics apply to electrothermal thrusters for thrust production through high energy propellant gas acceleration.

To have a high exhaust velocity, the propellant gas accelerated through the nozzle needs to have a high temperature and pressure. This requires highly efficient heating of the gas. The area of contact between the heat source and the propellant gas needs to be increased for higher energy transmission. This can be achieved using multi-channel heat exchangers [90]. The exhaust velocity v_e is dependent on temperature and the specific heat capacity of the propellant gas ($1/2 v_e^2 \approx c_p \mathcal{T}_c$). The specific impulse $I_{sp} = v_e/g_0$. Thus, to increase the I_{sp} , a quadratic increase in chamber temperature is required. The temperature depends upon

the power input as well as the mass flow rate of the propellant. However, unlike chemical thrusters, the temperature is inversely proportional to the mass flow rate since a higher flow rate would mean lesser time for heating, thus a lower flow rate would mean a very high temperature.

Heating losses occur due to the poor thermal conductance of the gaseous propellant. The thermal and viscous boundary layers also influence the flow gradients. A part of the input electrical power, when converted to thermal energy, is lost in thermal radiation. The performance of electrothermal thrusters could be seriously impaired by the inability of the propellant gases to maintain their internal energy during nozzle expansion. The specific heat capacity strongly depends upon the temperature. These are called frozen flow losses. Thus, a prudent choice of propellant is required. Propellants with low molecular weight are very advantageous.

Electrostatic propulsion devices rely on Coulomb force to produce thrust by accelerating charged propellant particles. The classic examples are Gridded Ion Thruster (GIT), Hall Effect Thruster (HET), electrospray thrusters and Field Emission Electric Propulsion (FEEP) thrusters [88]. Operation of electrostatic devices occurs in near-vacuum conditions. The particles of the propellant need to be charged for the electrical force to have an effect, since the force depends only upon the charge. Additionally, the charged particles should have the same charge to move in one particular direction that is desired. Electrons, although easy to produce and accelerate, have a very small mass and are easily influenced by magnetic fields. Thus, they are not a viable for electric propulsion. A heavy molecular mass molecule is ionised and those positive ions are utilised for propulsion since they carry significant momentum, hence a useful amount of thrust can be generated.

In electron bombardment type electrostatic devices, the propellant gas which is in neutral state is injected into the chamber. The injection occurs very close to the cathode which is the source for electrons. These electrons traverse from cathode to anode. They bombard the neutral gas molecules which then leads to the production of positive ions. Enhancement of the electron bombardment of neutral particles is achieved by confining them using magnetic rings. The positively charged ions are then accelerated by the electric field by the action of Coulomb force [88].

Electrospray thrusters extract ions or charged droplets from conductive liquid propellants that are fed through small needles. They are then accelerated through high voltage static electric field. FEEP thrusters transport liquid metals such as indium or caesium along needles, extract the ions using field emission process, and accelerate them using an electric field [91, 92].

Desirable design characteristics of electrostatic thrusters include minimisation of energy input per charged particle, minimisation of sputtering and deterioration of acceleration electrodes due to ion collision damage, maximisation of propellant utilisation, stable and effective acceleration of uniformly charged particles, minimisation of plume reactivity with rest of the system, avoidance of hazardous propellants, and optimisation of thrust and specific impulse within the design envelope [27].

Electromagnetic thrusters utilise the Lorentz Force for plasma acceleration and thrust production. The propellant gas is heated to a plasma state, at which they readily conduct electricity. When a current carrying conductor is placed perpendicular to a magnetic field, a body force is exerted on the conductor in a direction that is perpendicular to both the direction of the current and the direction of the magnetic field.

In electromagnetic thrusters where there is no ionisation of the propellant, neutral exhaust beams are produced. Electromagnetic thrusters have a higher thrust density, i.e., thrust per unit area compared to gridded ion thrusters. Two main thrusting concepts in electromagnetic thrusters are continuous / steady-state thrusting and pulsed thrusting (intermittent).

The MARIO mission pursues a long duration low-thrust heliocentric transfer to reach Mars. This requires systems of high I_{sp} . Although electrothermal thrusters have a higher I_{sp} than chemical thrusters, the value is not adequate to satisfy the needs of the mission regarding system mass and transfer time. Thus, only electrostatic and electromagnetic systems are taken into consideration. In this section, the gridded ion thrusters, Hall effect thrusters, field emission electric propulsion systems, pulsed plasma thrusters, and helicon thrusters are explored.

3-2-1 Gridded ion thrusters

Gridded ion thrusters (GITs) are electron bombardment type electrostatic thrusters in which the ionisation and acceleration mechanisms are de-coupled in the sense that the ionisation occurs in the ionisation chamber and the acceleration occurs through an accelerator grid. The main components of the GIT are

- ▶ Plasma generator (discharge cathode, anode, magnetic ring, rf coil etc.)
- ▶ Accelerator grids (screen grid & acceleration grid)
- ▶ Neutralizer cathode

The gas is injected into the ionisation chamber, where the electrons bombard the neutral to form ions. This leads to a formation of a quasi-neutral plasma in which the number of positive ions and negative electrons are approximately the same. The ions produced traverse through the chamber and through the grids where a very strong electric field is present. The ion plume is then neutralised using an external neutraliser cathode that supplies electrons. Figure 3-2 presents a schematic of NSTAR gridded ion thruster on-board Deep Space 1 spacecraft. The discharge cathode, anode and the magnetic rings that confine the electrons form the plasma generator.

The plasma generator is at a high positive voltage compared to the spacecraft or space plasma. Thus, a *plasma screen* encloses it which is biased near the spacecraft potential to stop electron transfer from space plasma to the positively biased surfaces. The performance of the ion thruster depends upon the efficiency of the plasma generator [88].

The thrust ultimately depends upon the momentum transfer from the exhaust beam to the spacecraft. The two critical parameters that determine the thrust are the mass flow rate and the exhaust velocity. The exhaust velocity is calculated directly from the applied beam voltage, i.e., the voltage applied across the screen and acceleration grids. The potential difference across the grids imparts energy to the ions which is directly converted into exhaust velocity.

Mass flow rate is another critical parameter for thrust generation. Part of the input mass flow is ionised and the critical parameter is the current of ions flowing between the grids, which

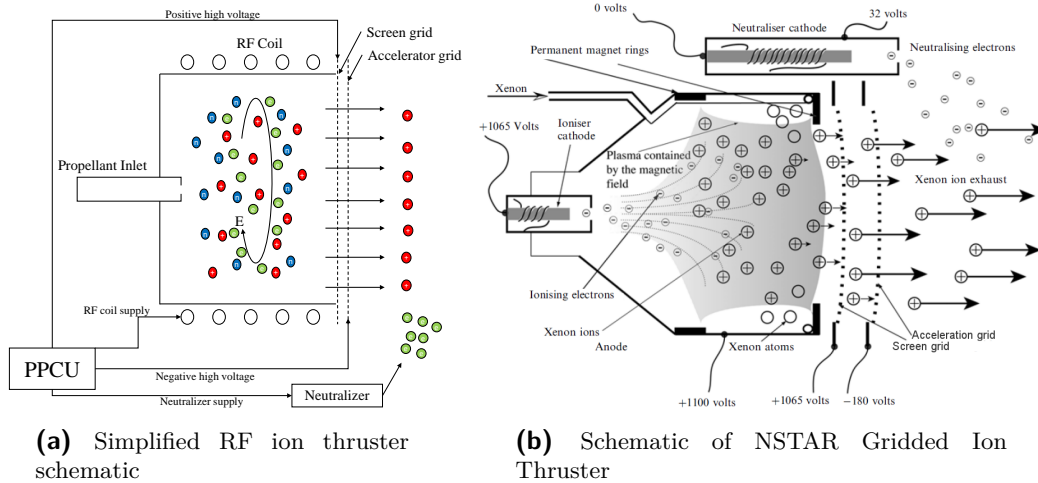


Figure 3-2: Simplified schematic of RF ion thrusters and the NSTAR Gridded Ion Thruster on-board Deep Space 1 (NSTAR image retrieved from Turner [90])

becomes the exhaust stream. Additionally, unionised neutral gas particles also contribute to the thrust, although they are not accelerated by the grids. Thrust is directly proportional to the ion current and to the mass-to-charge ratio of the charged particles. The current density j , electric current per unit area, has a saturation value depending upon the geometry and the electrical field [93]. The internal electric field associated with the ion cloud opposing the accelerating electric field is the cause for this limitation in current density. This occurs when excessive amount of likely charged particles try to pass through the accelerator grid.

The electric field present between the screen and acceleration grids is constant and dependent on the potential difference unless otherwise ions flow through. These ions alter the electric field and the screen grid is partially shielded by them. The acceleration field's profile depends upon the ion flow rate. If the current increases, the exhaust stream density increases. When the density reaches a certain value, the accelerating field at the screen grid drops to zero since the positive charge of the ions downstream of the flow (in the acceleration grid) effectively cancels the field in the screen grid. This value is called the *space charge limit*, which represents the maximum ion current that can flow. Although ion acceleration can still occur further into the cell, this limiting value of ion current prevents further ingress of ions from the chamber into the grid.

The ion velocity at the acceleration grid depends upon the beam voltage. Thus, the effect of space charge does not affect the ion exhaust velocity but only the ion mass flow rate. The saturation current can be derived for a plane-geometry electrode configuration.

Plasma generation is achieved by three mechanisms, a) Direct current (DC) electron discharge, b) Radio frequency (RF) discharge, c) Microwave discharge. A special type of DC electron discharge plasma generation based thruster called the Kaufmann ion thruster is widely used.

Plasma generation in DC Discharge ion thrusters is achieved using a hollow cathode as an electron source and an anode potential discharge chamber with magnetic multipole boundaries [88]. The electrons discharged into the chamber ionise the neutral gas through bombardment. They are confined in the ionisation chamber by the magnetic field that are applied, thereby

increasing their path and improving ionisation efficiency. The discharge electrons, the neutral gas, and the ionised gas form the plasma. This plasma discharge is then extracted by the accelerator grids to produce thrust. Discharge chamber (ionisation chamber) geometry plays a crucial role in plasma formation and sustenance.

The Kaufman type ion thrusters feature a strongly diverging magnetic field that shields a cylindrical anode located near the wall of the discharge chamber. The electron transport to the anode from the cathode is determined by cross-field diffusion. Kaufman type thruster is a type of a DC discharge thruster [88].

The radiofrequency ion thrusters utilise electromagnetic fields to heat the plasma electrons and in turn ionise the injected propellant gas. This is done to avoid power supply and instrument life issues that arise with hollow cathode and DC discharge power supply. An inductive plasma generation mechanism is used, which is called the radiofrequency plasma generator. A low frequency RF voltage is applied to an antenna structure around or in the plasma and the RF energy is coupled to the electrons. In its simple configuration, an RF coil is wrapped around an insulating chamber where the gas is fed. The chamber is connected to an accelerator grid for ion acceleration. The RF coil is connected to an RF power supply that serves as the power source for plasma generation. Compared to DC discharge thrusters, there is no need for an internal cathode as well as magnetic confinement in RF ion thrusters [94].

Microwave ion thrusters utilise electromagnetic field at microwave frequencies to generate the plasma. They differ from RF ion thrusters by the virtue of electromagnetic frequency utilised to generate the plasma and consequently heat it. The plasma density and the microwave frequency have to be balanced properly for the plasma to be conducive for microwave propagation. The microwave energy is coupled to the plasma by resonant heating of electrons in the magnetic field amid collisions. The pressure required to achieve sufficient collisions and the magnetic field required to achieve resonance are significant, leading to a penalty in performance or complexity in design [88].

GIT technology is well developed and has a high maturity. Several efforts have been undertaken to miniaturise the traditional GITs which are heavily power consuming. Miniaturised GITs have a high I_{sp} and a low power consumption. The most famous example is the Miniature Xenon Ion Thruster (MiXI) developed by Jet Propulsion Laboratory (JPL). Different configurations of the thruster exist based on the type of discharge: 3-Ring and Axial Ring-Cusp Hybrid (ARCH). The difference is that MiXI (ARCH) has a higher total efficiency and a lower power consumption compared to 3-Ring configuration. On the other hand, 3-Ring has a higher thrust and specific impulse, albeit with a slightly higher power consumption [95, 96]. MiXI yields a maximum thrust and I_{sp} of 1.55 mN and 3184 s, respectively. Miniature Radiofrequency Ion Thrusters (RIT) has been developed at the University of Gießen and Airbus Defense & Space GmbH (formerly EADS Astrium), with the RIT- μ X version yielding a nominal thrust of 500 μ N and consuming <50 W. This performance can be extended further upto 2 mN thrust and 3000 s I_{sp} [97]. Busek Company Inc developed the BIT-3 ion thruster, which has a size of 2.5 cm. The BIT-3 was designed for a CubeSat and consumes a peak power of 80 W while yielding 1.25 mN and 2300 s [98]. A miniature cathodeless ion thruster, NPT30, that is capable of utilising xenon and iodine has been developed by ThrustMe, France [99]. Some of the existing miniature ion thrusters are listed in Table 3-1 [14, 98, 99].

Table 3-1: Summary of gridded ion thruster state-of-the-art

Engine	Manufacturer	Thrust [mN]	I_{sp} [s]	Power [W]	TRL
MiXI (3-Ring)	JPL	0.1–1.55	1764–3184	14–50	6
MiXI (ARCH)	JPL	0.1–1.3	1700–3080	14–50	6
RIT- μ X	Uni. Gießen / Airbus D&S	0.05–0.5	360–2850	12.5–35	6
BIT-3	Busek	0.6–1.25	1200–2300	56–80	6
NPT30-I2	ThrustMe	0.4–1.1	700–1500	30–60	6

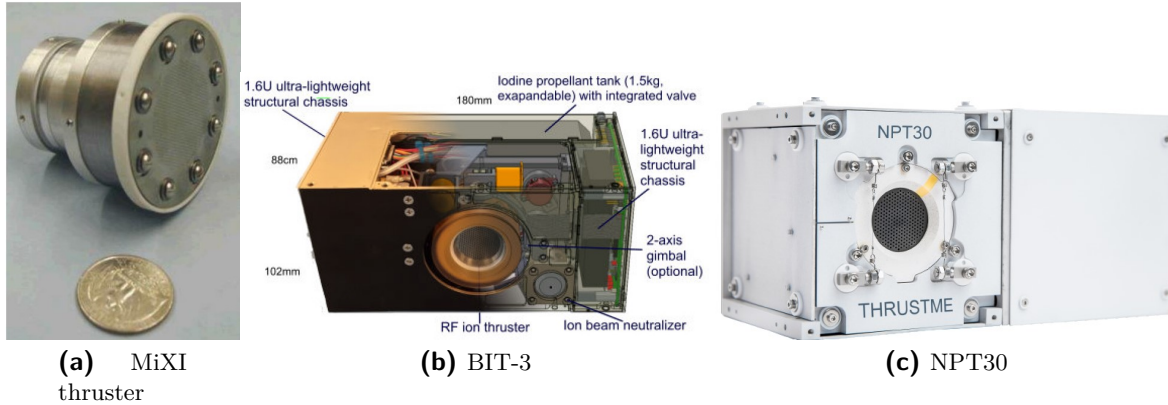


Figure 3-3: Gridded ion thruster state-of-the-art. MiXI thruster by JPL (image retrieved from Wirz et al [100]), BIT-3 by Busek Company Inc (image retrieved from datasheet [98]), and NPT-30 by ThrustMe (image retrieved from datasheet [101])

3-2-2 Hall thrusters

The principle of operation for a Hall Effect Thruster (HET) or Hall thruster is ionisation of the propellant gas and acceleration of the ionised propellant by an electric field. The ionisation of the neutral propellant gas is achieved by electron bombardment. A radial magnetic field is applied while the accelerating electric field is in the axial direction. The electron trapping is achieved using *Hall Effect* [102].

Hall effect is the production of a potential or a voltage across an electrical conductor that is placed in a traverse electric field and acted upon by a perpendicular magnetic field. The voltage produced is perpendicular to both the electric and the magnetic fields. In the case of Hall thrusters, the magnetic field is radial and the electric field is axial. Thus, the charge q placed in such a field will experience a drift in the azimuth direction.

The electrons are provided by a cathode that is placed outside the thrusting chamber. The electrons move towards the anode placed inside the chamber, near the propellant inlet. During the electron motion, the axial electric field and the radial magnetic field induce the azimuth drift, essentially trapping the electrons in a circular path. This increases the bombardment of electrons on the neutral propellant atoms, thereby increasing the ion production efficiency [27].

Hall thrusters do not have accelerator grids like GITs. Instead, the electrostatic acceleration occurs within the core of the discharge. The ions are accelerated due to high potential difference between the anode and the cathode. The thruster performance depends upon

the channel structure and magnetic field shape. Hall thrusters are also known sometimes as Stationary Plasma Thrusters, the devices that were invented in the Soviet Union. In comparison to the Ion thrusters, the Hall thrusters have lower efficiency and specific impulse. However, the thrust-to-power ratio is higher in Hall thrusters [88]. Additionally, fewer power supply sources are required to operate the Hall thrusters.

Two generic types of Hall thrusters are present,

1. Thrusters with dielectric insulating wall
2. Thrusters with anode layer (TAL)

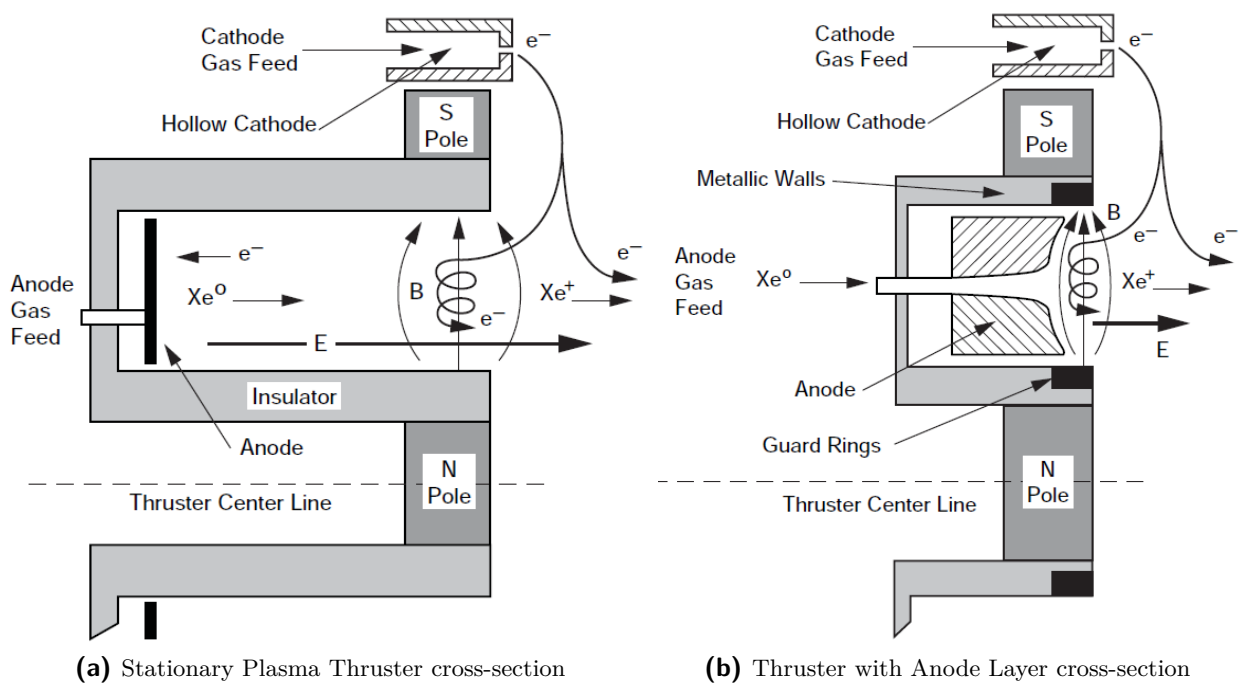


Figure 3-4: Types of Hall Effect Thrusters: Figure a shows the crossed electric and magnetic fields as well as the ion and electron paths in a stationary plasma thruster. Figure b shows the same for Thrusters with Anode Layer (Images retrieved from Goebel et al [88])

In Stationary Plasma Thrusters (SPT), the dielectric insulating wall is made of Boron Nitride (BN) or Borosil (BN-SiO₂) in flight thrusters. Some laboratory thrusters use Alumina (Al₂O₃). Sputtering, a process whereby particles are ejected from a solid target material due to bombardment of the target by energetic particles, is low in case of these dielectric materials. The anode in these thrusters are placed at the base of the chamber where the propellant gas is injected. The electrons produced by the external cathode travel through the chamber towards the anode, where, on the way, they are trapped by the magnetic field. These electrons move along the magnetic field lines and in the $\mathbf{E} \times \mathbf{B}$ azimuthal direction, around the channel. They diffuse by collisional processes and electrostatic fluctuations to the anode and channel walls. The plasma discharge created by the electrons ionises the neutral propellant gas. The life of the thruster is determined by the sputtering of the dielectric material caused by the ion and

electron bombardment of the dielectric wall. The reduced axial electron mobility produced by the transverse magnetic field permits the applied discharge voltage to be distributed along the channel axis in the quasi-neutral plasma, resulting in an axial electric field in the channel that accelerates the ions to form the thrust beam [103].

The GITs have a space-charge limit imposed by the grid spacing in the accelerator grids. However, owing to the absence of such grids in Hall Effect Thrusters and also owing to the fact that much of the acceleration occurs near channel exit, the space-charge is not an issue and also the ion current density as well as the thrust density can be considerably higher than that of the GITs. Additionally, the external hollow cathode produces electrons for two functions: Plasma production and plume neutralisation.

In Thrusters with Anode Layer (TAL), the dielectric insulating material is replaced by a conducting metallic wall. The name *Thruster with Anode Layer* is adapted from Russian literature [103], that corresponds to a narrow electric field region near the anode. This shortens the channel length by a significant margin but does not change the fundamental ion generation or acceleration mechanism. Owing to the conducting nature of the chamber wall, it becomes a part of the magnetic circuit. The wall is biased negatively to repel electrons such that they remain in the ionisation region and to sustain the ionisation rate. The schematic of the two types of Hall thrusters are illustrated in Figure 3-4.

The TAL operation is very similar to SPT operation. However, the primary difference is that the channel walls at the exit plane have metallic guard rings biased at cathode potential to reduce the electron loss. The life of TALs is determined by guard ring material since the ion bombardment cause erosion of the guard rings. The anode typically extends close to the thruster exit. The shape of the anode is curved and funnelled to constrain the neutral gas and the plasma to the centre of the channel, away from the guard rings, and not to intercept the magnetic field lines. The TALs have a channel width that is typically twice the channel length, including the anode placement.

Insofar, Hall thruster development has not been pursued for CubeSats since scaling down is a significant issue [13]. Hall thrusters with sizes similar to GITs have a higher thrust, higher power consumption, and a lower I_{sp} . In general, I_{sp} values range from 1500–2000 s [13]. Reduction in Hall thruster size directly affects the electron Larmor radius (radius of gyration of a charged particle), thus requiring much stronger magnetic fields to confine the electrons so as to avoid wall impingement and subsequent loss in efficiency. A miniature Hall thruster was developed by MIT which produced 1.8 mN thrust and 826 s I_{sp} while consuming 126 W of power [104]. Busek Company Inc has developed two classes of Hall thrusters, with average consumption of 100 W and 200 W, respectively. The 100 W BHT-100 thruster yields a thrusts of 6.5–8.3 mN and I_{sp} of 985–1274 s [105]. The 200 W BHT-200 has flight heritage and yields 4–13 mN thrust with I_{sp} of 1200–1500 s [106]. Princeton Plasma Physics Laboratory (PPPL) has developed a 100 W Cylindrical Hall Thruster that yields thrusts of 3–6 mN and I_{sp} of 1100–1650 s while consuming 90–185 W power [107]. SITAEL S.p.A have developed HT100 thruster, a 100 W class thruster that has a power range of 120–250 W yielding thrusts of 6–18 mN and I_{sp} of 1000–1600 s [108]. Table 3-2 summarises the Hall thruster state-of-the-art.

Table 3-2: Summary of gridded ion thruster state-of-the-art

Engine	Manufacturer	Thrust [mN]	I_{sp} [s]	Power [W]	TRL
BHT-100	Busek	6.5–8.3	985–1274	111–163	5
BHT-200	Busek	4–13	1200–1500	100–200	9
Mini HT	MIT	1.8	865	126	6
CHT 3.0	PPPL	3–6	90–185	6	
HT100	SITAEL	6–18	1000–1600	120–250	6

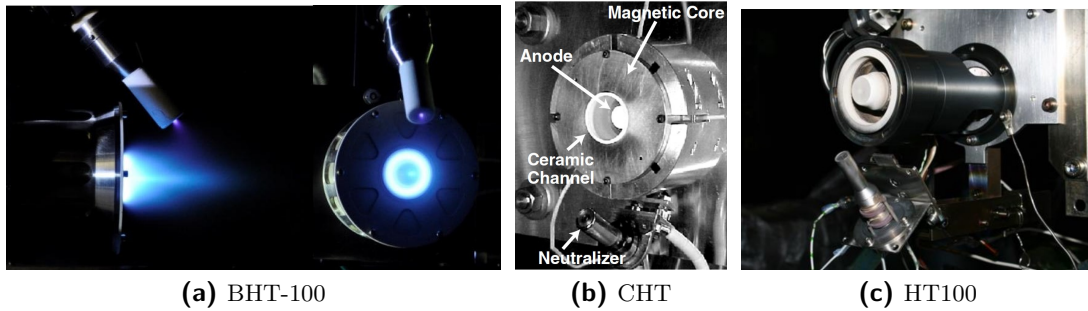


Figure 3-5: Hall effect thruster state-of-the-art. BHT-100 thruster by Busek Company Inc (image retrieved from Szabo et al [105]), CHT 3.0 by PPPL (image retrieved from Polzin et al [107]), and HT100 by Sitael (image retrieved from Misuri et al [108])

3-2-3 Field emission electric propulsion

Field Emission Electric Propulsion (FEEP) thruster is a type of electrostatic thruster in which a liquid metal is fed through a positively charged capillary tube or a porous needle (emitter), where it is ionised and the ions are extracted using an accelerator electrode. The potential difference between the emitter and the accelerator is in the order of 10 kV. This generates a strong electric field and at the tip of the capillary, and Taylor cones of the liquid metal are produced and the electric field is focused, which leads to the extraction of ions from the liquid and acceleration of such ions towards the cathode [91]. An external source of electrons need to be provided to neutralise the stream of ejected ions [109].

In FEEP emitters, the ions are extracted directly from the liquid. The common propellants are liquid metals such as Indium and Caesium which have high atomic weight, low ionisation potential, low melting point, and good wetting capabilities on the emitter substrate [91, 110]. Caesium is used in thrusters with internally wetted slit emitters while Indium is used in thrusters with porous needle emitters [13]. The specific impulse of FEEP thrusters range from 4000-10000 seconds. The thrust could be easily fine-tuned and pulse mode operation is enabled due to the instantaneous switching capability [102].

Thrust production is achieved by the acceleration of field evaporating ions into an exhaust beam. In Caesium propelled FEEP thrusters such as FEEP-5 developed by Centropazio (later Alta Space and now SITAEL S.p.A), the emitter consists of two metallic plates with a small propellant reservoir. On one side of each plate, a sharp blade is precisely machined and a thin layer of Nickel is sputter deposited on the other three sides of one of the plates. A thin channel of about $\sim 1\mu\text{m}$ diameter is machined to allow the flow of Caesium, forming

Centrosazio developed the FEEP-5 and FEEP-50 thrusters which have an I_{sp} of ~ 9000 s. The former yields a thrust of 0.04 mN while consuming 2.7 W and the latter yields 1.4 mN while consuming 93 W [13]. External PPCUs are required which add to the mass of the entire system. The IFM Nano Thruster has a thrusting range of 10 μ N to 0.4 mN with I_{sp} of 2000–6000 s. The system power consumption is 8–40 W [118]. Enpulsion has also developed the IFM Micro Thruster which has a thrust range of 75 μ N to 1.5 mN, I_{sp} of 1500–6000 s, and a power consumption of 20–100 W. Performance tests of the Indium FEEP thruster developed at Austrian Institute of Technology yielded 1.28 mN with $I_{sp} > 6000$ s and a power-to-thrust ratio of 80W/mN [112]. The FEEP thruster state-of-the-art are listed in Table 3-3.

Table 3-3: Summary of Field Emission Electric Propulsion state-of-the-art

Engine	Manufacturer	Thrust [mN]	I_{sp} [s]	Power [W]	TRL
FEEP-5	Centrosazio	0.04	9000	2.7	9
FEEP-50	Centrosazio	1.4	9000	93	9
IFM Nano	Enpulsion	0.001–0.4	2000–6000	8–40	9
IFM Micro	Enpulsion	0.075–1.5 mN	1500–6000	20–100	9



(a) FEEP-5



(b) IFM Nano

Figure 3-7: Field Emission Electric Propulsion state-of-the-art. FEEP-5 thruster by Centrosazio (image retrieved from Marcuccio et al [119]), IFM Nano Thruster by Enpulsion (image retrieved from datasheet [120])

3-2-4 Pulsed plasma thrusters

Pulsed plasma thruster, as the name suggests, is an electromagnetic thruster with a pulsed operating concept. It uses Lorentz Force for plasma acceleration and thrust production. In one of the common types of pulsed plasma thruster, which is a solid-Teflon micro pulsed plasma thruster, the solid propellant is fed using spring action while the capacitor is charged from a primary power supply and applies 1-2 kV across the exposed Teflon surface. The discharge is initiated by a spark plug, whose shape is formed by additional pulse-forming circuitry [89]. Additionally, the thermal flux, particle bombardment and surface reactions ablates, sublimates and partially ionises small amounts of solid material. The resulting partially

ionised gas is heated to a plasma state, at which it readily conduct electricity. This partially ionised gas enables an electrical contact between the two electrodes maintained at a high potential which were previously separated by a vacuum. The discharge formed between the two electrodes travels through the propellant and ionises it further.

Since the current, which occurs instantaneously, is very high ($\sim 10 - 20$ kA), there is a self-induced magnetic field and it is high enough to create a magnetic pressure comparable to the gas kinetic pressure in the thin ionised layer. The slug of gas is then accelerated by both the magnetic pressure and the gas kinetic pressure such that it reaches a velocity close to *critical Alfvén velocity*, at which the kinetic energy equals the ionisation energy [89]. The Alfvén wave is a fundamental physical phenomenon in all kinds of magnetised plasmas. Essentially, the magnetised plasmas behave like a wave on a string in tension. The pressure imparted by the magnetic field and the energy density of the plasma influence the plasma dynamics. The plasma behaves like air, except that it is affected by magnetic fields. The *Alfvén velocity* is equivalent to the *speed of sound* in the plasma.

The specific impulses of the PPTs are in the range of 500-1000 seconds, which is subject to increase with an increase in power. One of the primary advantages of the PPT technology is that it is very compact. It uses a non-toxic propellant feed system which is placed alongside the thruster in a single compact unit. Additionally, it is very flexible in terms of operation over a wide range of power or thrust by a simple variation of the repetition rate. Precision orbital control and attitude control could be achieved using the PPTs. The limiting factors of the thrust levels in PPTs are the power and the rate of capacitor recharge.

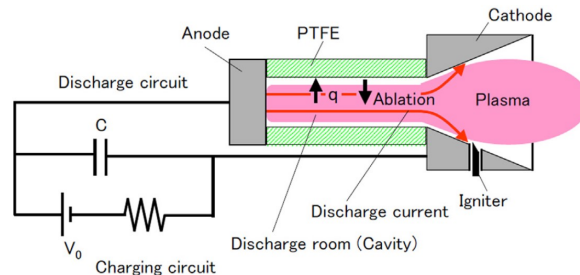


Figure 3-8: Pulsed plasma thruster schematic (image retrieved from Kisaki et al [121])

In addition to the solid PPTs, liquid and gas propellant PPTs can also be used. The latter give more flexibility compared to the solid PTFE based PPTs with regards to higher impulse bits [14]. However, liquid and gas propellants require more power per pulse than solid propellants. Also, liquid PPTs require precision valves to control the feed of liquid propellants, which are incredibly hard to design and operate. Despite their advantages, the efficiencies of PPTs that use solid propellants are $\sim 10\%$. Additionally, there is a possibility of thruster pulse failure when Teflon is used [13].

The thrust provided by the PPTs is in the range of a few μN . There have been many PPTs developed for CubeSat application. The Micro-Pulsed Plasma Thruster (μPPT) developed by Austrian Institute of Technology (formerly Austrian Research Centres GmbH) operates on PPT with an impulse bit of $10-20$ μN s and an I_{sp} of 1000 s [122]. Mars Space Ltd and Clyde Space developed PTFE PPTs called PPTCUP and Nanosat PPT. PPTCUP has an impulse bit of 45 μN -s and an I_{sp} of 650 s while consuming 2 W power. NanoSat PPT has a $90\mu\text{N}$ -s impulse bit, I_{sp} of 640 s, and a power consumption of 5 W. Busek Company Inc developed

the Micro Pulsed Plasma Attitude Control System - MPACS that provides $80\mu\text{N}\cdot\text{s}$ impulse bit with an I_{sp} of 826 s and consumes 10 W power. BmP-220 is another thruster by Busek that yields $0.02\text{ mN}\cdot\text{s}$ impulse bit with an I_{sp} of 536 s. The power consumption is 10 W. [32]. At Research Institute of Applied Mechanics and Electrodynamics (RIAME), several ablative PPTs for microsatellites have been developed [123].

Table 3-4: Summary of Pulsed Plasma Thruster state-of-the-art

Engine	Manufacturer	Impulse Bit [μNs]	I_{sp} [s]	Power [W]	TRL
μPPT	AIT	10–20	1000	0.5–4	6
PPTCUP	Mars Space & Clyde Space	40	655	2	6
NanoSat PPT	Mars Space & Clyde Space	90	640	5	5
MPACS	Busek	80	826	8–40	9
BmP-220	Busek	20	536	20–100	9
APPT-8	RIAME	110–220	530	10–20	6
APPT-120	RIAME	900	730	60	8

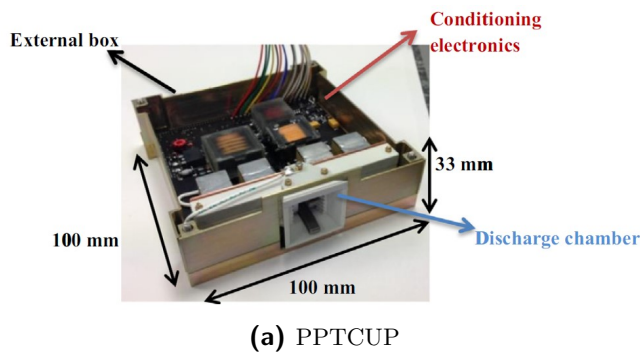


Figure 3-9: Pulsed Plasma Thruster state-of-the-art. PPTCUP thruster by Mars Space Ltd and Clyde Space (image retrieved from Ciaralli et al [124]), Bmp-220 Thruster by Busek (image retrieved from datasheet [125])

3-2-5 Helicon thrusters

Helicon plasma thruster (HPT) is a relatively new concept that is currently being extensively researched [126]. The helicon plasma thruster device consists of a helicon source to generate the plasma and heat it. The plasma is then accelerated using a magnetic nozzle. The components of an HPT are cylindrical dielectric chamber, a propellant injection system, and an external antenna wrapped around the chamber to generate radiofrequency waves at 1–26 MHz frequencies that propagate through the plasma [127–129]. Another set of permanent magnets or magnetic coils create longitudinal magnetic field.

Inside the chamber, the magnetic field is predominantly axial whereas it is divergent near the nozzle. This allows the rf waves to propagate inside the plasma layer like a helicon. The helicon waves pertain to a branch of whistler waves, where in a cold unbounded plasma, no other waves can propagate in that frequency range [130]. The typical hierarchy of frequency in a helicon source is $\nu_e, \omega_{lh} \ll \omega \ll \omega_{ce} \ll \omega_{pe}$ which are effective electron collision frequency

(ν_e), lower hybrid frequency, wave frequency, electron cyclotron frequency, and plasma frequency respectively. The chamber walls are screened by the magnetic field which leads to a drastic reduction of plasma losses at the walls [131]. The helicon wave energy is utilised in two parts: one part is spent on the electrons to ionise the propellant and the other part is converted in the magnetic nozzle into directed kinetic energy of ions [130, 132].

The divergent magnetic field creates a magnetic nozzle that accelerates the plasma up to supersonic speeds. This transforms the internal energy of the plasma to an axially directed one, thus producing thrust. This forms the basis of the helicon plasma thrusting mechanism. At some point, plasma detachment occurs at the nozzle [133–135] that causes the formation of a *double layer* structure [127, 136].

Helicon plasma sources vastly increase the ionisation efficiency and also the electron density than a typical inductively coupled plasma (ICP) thruster. In ICP thrusters, the plasma source is the energy supplied by electric currents that are produced by electromagnetic induction. The magnetic intensity is easily adjusted and there is no severe cut-off plasma density for wave propagation [137].

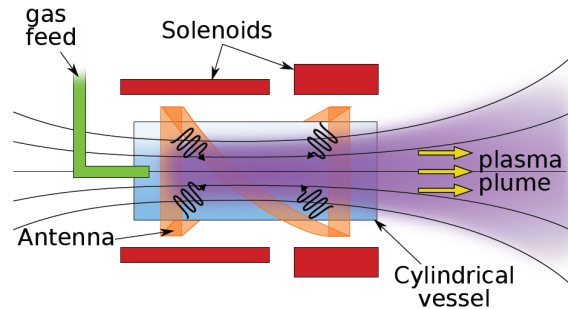


Figure 3-10: Helicon plasma thruster schematic (image retrieved from Navarro et al [138])

The advantage of the HPTs over other electromagnetic thrusters is that they lack electrodes. Thus, the lifetime of HPTs are generally longer due to the avoidance of thruster erosion. Additionally, the HPTs can operate with a wide range of propellants. They have high throttability since the capability to actuate magnetic nozzles and propellant injection is very high. The primary disadvantage of HPTs is that the thruster efficiencies are very low compared to existing plasma thrusters. Also, maturity of HPTs is low.

A proof of concept of a helicon double layer thruster has been performed at the Australian National University with some direct thrust measurements [139]. However, the most advanced work in helicon thruster design has been pursued at University of Padua, Italy where a 50 W helicon thruster was first designed [129]. A spin-off company named T4i - Technology for Propulsion and Innovation has commercialised a helicon thruster, called the REGULUS [140]. The thruster yields 0.3–0.9 mN thrust and has an I_{sp} of 900 s while consuming 60 W of power. It has a TRL of 6.

3-3 Multimode propulsion

Multimode propulsion integrates two or more propulsive modes into a unified propulsion system, e.g, the propulsion system includes chemical and electric modes of operation while



Figure 3-11: Helicon plasma thruster state-of-the-art. REGULUS by T4i - Technology for Propulsion and Innovation (image retrieved from datasheet [141])

using the same setup [33]. It provides flexibility in operating the spacecraft in high-thrust and low-thrust modes without having to resort to multiple systems and increased complexity. Rovey et al [33] clearly distinguish multimode, or dual-mode in case of only two types, from hybrid propulsion. In dual-mode propulsion, resources such as the propellant and feed system are shared between the chemical and electric modes. In hybrid propulsion, the chemical and electric propulsion are separate systems in the same spacecraft with no resource sharing. However, the terminology induces confusion since hybrid propulsion in rocketry generally refers to the usage of chemical propellants in different states, e.g., liquid oxidiser and solid fuel. In this work, the term hybrid is avoided and rather the term *combined* is used. This differs from the terminology used by Rovey et al [33]. Multimode propulsion system types are illustrated in Figure 3-12.

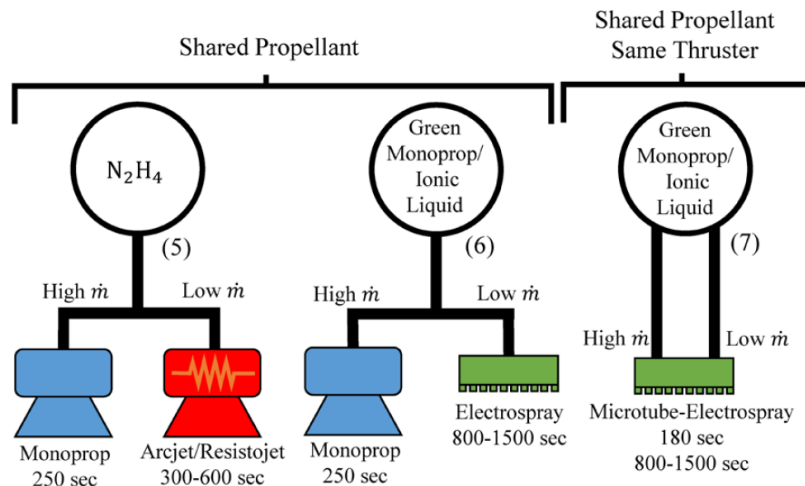


Figure 3-12: Multimode space propulsion system types that have shared resources such as propellant and/or the thruster (image retrieved from [33])

It can be observed that in the propulsion systems with shared propellant, two different thruster types exist. A high-thrust low- I_{sp} monopropellant system that expels hydrazine or a green propellant and a low-thrust high- I_{sp} electric propulsion system, usually electro spray, that

ionises and accelerates the propellant. In the shared propellant shared thruster system, a singular thruster is used. The propellant is either expelled in high-thrust mode by using the storage pressure or it is expelled in a low-thrust mode by activating the electrodes required to ionise the propellant and accelerate it using electrostatic force. The maximum specific impulse yield is 1500 seconds while the maximum thrust yield is in the range of 0.5–1.6 mN. The power consumption in the electric mode is 22–63 W.

Depending upon the mission characteristics, the usage of dual-mode propulsion can be highly advantageous as the mass savings are significant. The system is simple and avoids many failure points that are otherwise found in terms of separated propulsion systems. The limiting factors include the maximum thrust and I_{sp} yield combined with the ΔV .

3-4 Systems design strategy and trade-off

The full system strategy is illustrated in Figure 3-13.

The mission characteristics are established in section 1-4. Once Earth escape is achieved using the chemical propulsion system and the spacecraft reaches Earth's sphere of influence, the deep-space cruise phase starts. A high- I_{sp} electric propulsion system is utilised in this phase. The cruise lasts for ~ 3.5 –4.5 years and culminates in ballistic capture [18]. Transfer to Mars after Earth escape could be achieved either by thrusting continuously, thereby minimizing flight time (time-optimal), or by thrusting intermittently to minimize propellant consumption (fuel-optimal). Depending on the mission priority, one of the two techniques can be used.

The general system definition involves the detailing of rest of the subsystems on the spacecraft. Electric propulsion system needs the critical resource of power, which it shares with the rest of the subsystems. Thus, the power consumptions of these subsystems should be defined such that the electric propulsion consumption requirements can be set. The state-of-the-art of electric propulsion systems are explored in section 3-2. In this section, the main requirements of the electric propulsion system and the heliocentric transfer are listed in Table 3-5. The requirements pertain to the maximum transfer time, maximum power consumption and system mass.

Table 3-5: Electric propulsion requirements

ID	Requirement
EP-01	The maximum transfer time shall be 4.5 years for cruise and ballistic capture.
EP-02	The electric propulsion system shall have a maximum power consumption of 70 W
EP-03	The total mass of the chemical–electric propulsion systems shall be no more than 16 kg.

The rationale for EP-01 is to constrain the maximum transfer time such that valuable science products can be obtained before the end of the mission lifetime, ~ 6 years. Additionally, CubeSats have a lower endurance to deep-space conditions, thus limiting their lifetime. The science mission is scheduled for ~ 6 months and the circularization maneuvers to attain the orbit about Mars takes ~ 195 days (see Section 3-7-5). If the transfer is achieved earlier than the maximum requirement, the science mission can be prolonged, thereby increasing the scientific output.

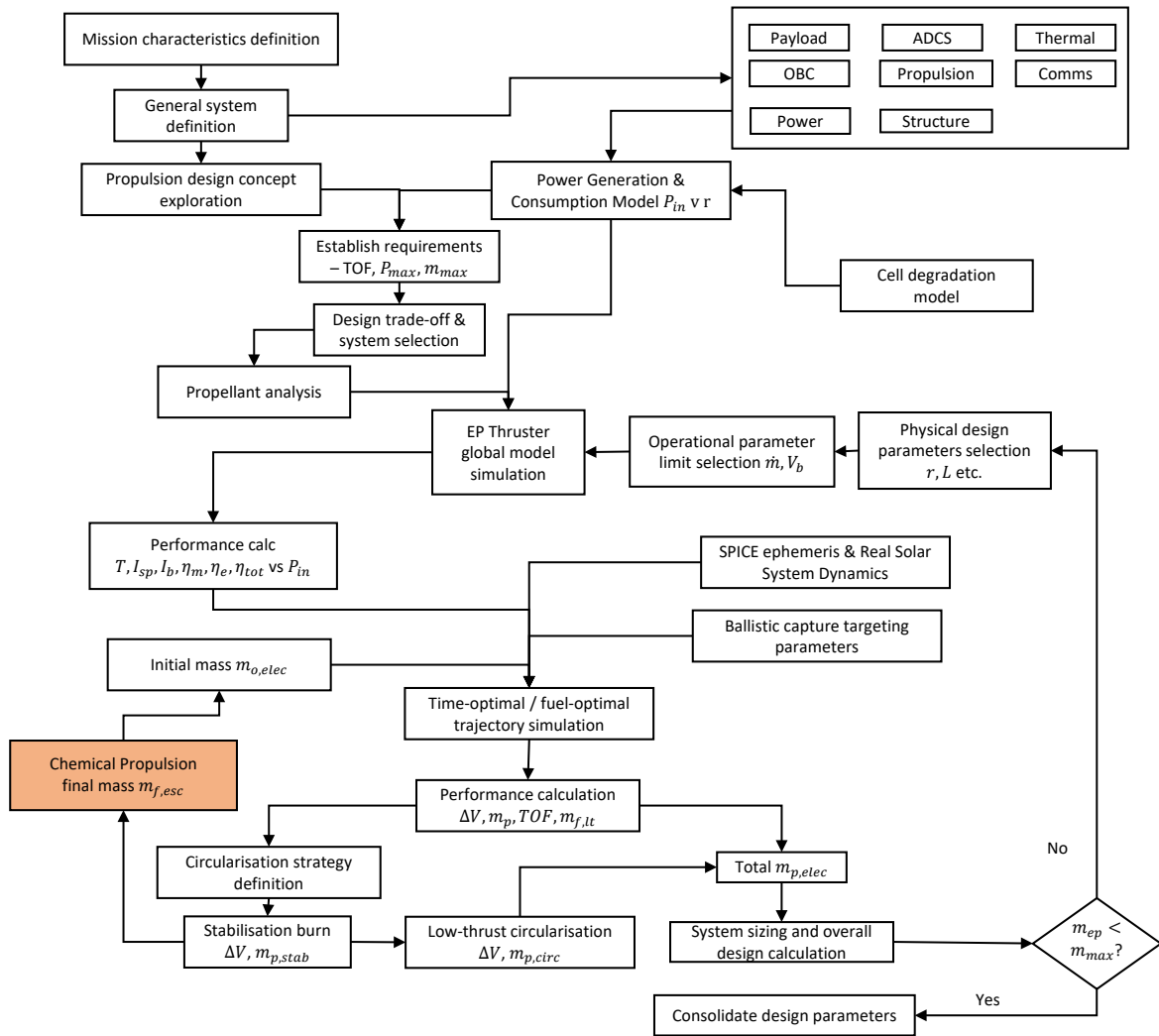


Figure 3-13: Electric propulsion system design strategy

Owing to the restricted power availability, EP-02 imposes a maximum limit on the power consumption of the thruster. Both thrust and I_{sp} vary with thruster input power P_{in} . The power available to the electric propulsion system is calculated as a function of the distance between the spacecraft and the Sun. Figure 3-14 illustrates the available and consumed power for the MARIO mission. The total power available at 1 AU at BOL is 202 W and at 1.5 AU at EOL is 85.75 W. Critical subsystems such as communications, on-board computer, attitude control, and electrical power system operate continuously during the transfer. The combined power consumption of these subsystems is ~ 40 W. Cell degradation, neutralization losses and the power processing and control unit (PPCU) consumption (3 W) are included in the thruster input power calculations. The minimum power supplied to the thruster (at ~ 1.5 AU) is 37.9 W.

The choice of the electric propulsion system is very crucial as the thrusts, power consumptions, and the specific impulses vary significantly among system types. The requirements listed in Table 3-5 indicate that to achieve the transfer, the thruster needs to have a high thrust, high

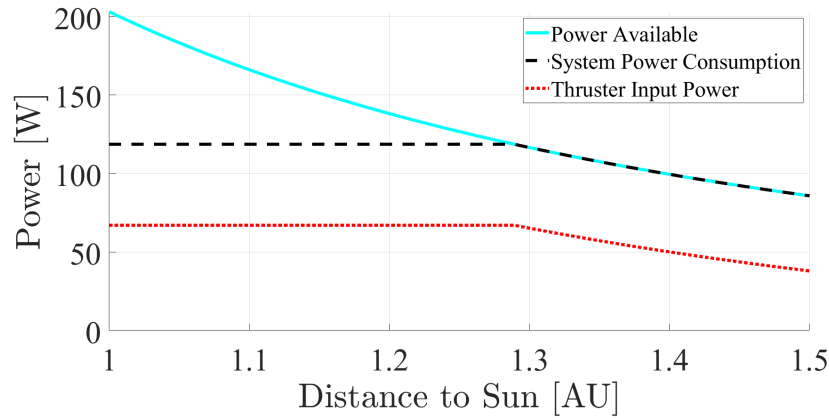


Figure 3-14: Generated and consumed powers variation with the Sun-spacecraft distance for MARIO mission

specific impulse, and high lifetime all while being severely power restricted. Thus, for the system trade-off, these parameters need to be compared. Considering the state-of-the-art, a brief comparison is shown in Table 3-6.

Gridded ion thrusters applicable for small spacecraft have an I_{sp} in the range of 1200-3200 seconds and a propulsion lifetime in the order of 30,000 hours [94, 142]. The power consumption is in the range of 14–80 W, which is highly desirable considering the maximum power requirement EP-02 for the MARIO mission. Hall thrusters yield high thrusts compared to ion thrusters, 1.8–18 mN. However, the I_{sp} yield is lower and the corresponding power consumptions are excessive (90–250 W), which makes it unsuitable in terms of the current mission requirements. Hall thruster lifetime is in the order of 10000 hours. Considering a ~ 4.5 year transfer with continuous thruster operation, Hall thrusters will not be able to deliver the spacecraft to the desired target. Down scaling of Hall thrusters is also a complex issue and dedicated development for CubeSats have not been pursued [13]. Field emission electric propulsion (FEEP) thrusters have very high I_{sp} but also have a considerably high power consumption for the thrust produced, ~ 80 W/mN [94, 112]. Additionally, FEEP lifetime is restricted to < 10000 hours [113]. Pulsed Plasma Thrusters (PPTs) have low I_{sp} and have a limit on propellant loading. The efficiency of PPTs is $\sim 10\%$, which is very low [13]. Lifetime of PPTs are in the order of 1000 hours. While considering the heliocentric transfer time and the corresponding thruster operation time (EP-01), both FEEP and PPT are unsuitable for this mission application. Helicon thrusters, although simple in architecture, have low I_{sp} , thrust, efficiency and lifetime [94]. Dual mode thrusters are similar to that of electrospray propulsion systems in terms of electric mode operation. Thus, lifetime and specific impulse play a crucial role. Considering the lifetime, specific impulse and power consumption, the gridded ion thruster is chosen for the analysis and is well suited for MARIO mission application.

Table 3-6: Comparison of electric propulsion options

Type	Thrust [mN]	I_{sp} [s]	Power [W]	Life [hours]
Gridded Ion	0.1-1.6	1200-3200	14–80	~30000
Hall	1.8-18	800-1600	90–250	~10000
FEEP	0.07-1.5	1500–6000	20–100	<10000
Pulsed Plasma	0.01-0.9	500-1000	0.5–100	~1000
Helicon	0.3–0.9	900–1000	50–70	~1000
Dual mode	0.6–1.6	250–1500	25–65	~1000

3-5 Propellant analysis

3-5-1 Xenon vs Iodine

Most common propellant for ion thruster applications is xenon. It is a noble gas with a high molecular mass (131 amu) and a low ionization potential (12.13 eV). The density of xenon gas is 5.76 kg/m^3 at standard atmospheric conditions. However, Xenon occurs only in trace amounts in the atmosphere and it is extracted as a byproduct in the oxygen separation process, thus making it very expensive ($\sim \$1140$ per kg). A move towards an alternative propellant that has a similar molecular mass and ionization potential is necessary to reduce the costs while achieving similar performances to xenon.

Iodine (I_2 or I), which is located adjacent to Xenon in the periodic table, is a good candidate and has a molecular mass 126.9 kg/kmol (monoatomic). It is a solid in standard atmospheric conditions with a density of 4940 kg/m^3 . This eliminates the need for high pressure tanks, plumbing, and sophisticated thermal control systems, which are otherwise required in the case of Xenon. Iodine stored in a solid state in compact lightweight tanks can be moderately heated to sublime and form I_2 vapour. This makes it highly suitable for deep-space CubeSat missions with high ΔV and subsequently large propellant mass requirements. Compactness of iodine makes it highly suitable for such CubeSat missions since the propellant can be easily accommodated within the structure. The ionization potentials (E_{iz}) for I_2 and I are 9.3 eV and 10.45 eV, respectively, which are lower than that of Xenon. This contributes to a higher electrical efficiency. Additionally, the cost of pure Iodine is $\sim \$400$ per kg. Although Xenon ion thrusters have a great flight heritage, Iodine ion thrusters are well suited for the current mission application. Multiple Iodine ion thrusters have been developed, such as Busek BIT-3, which will be demonstrated in space on-board Lunar IceCube 6U CubeSat launched by NASA SLS Artemis-1 in 2020 [142].

One disadvantage of Iodine is its corrosive nature. However, using corrosion-resistant materials like MACOR or Alumina in plasma-generation chambers makes ion thruster compatible with Iodine. Thruster grids made out of Nickel–Chromium alloys like Hastelloy or Inconel have high resistance towards Iodine corrosion [143, 144]. Solar panels and other external surfaces do not suffer from Iodine corrosion due to the high vapour pressure of I_2 , therefore its condensation is highly unlikely [145].

3-6 Radiofrequency ion thruster principles and performance model

Characterization of the electric propulsion system for a stand-alone CubeSat to Mars requires a performance model of the thruster and its corresponding application in a low-thrust trajectory optimisation framework. Gridded ion thrusters have a plasma generator, accelerator grids and a neutralizer cathode. The principle of operation of GITs are expounded in section 3-2-1. Plasma generation is achieved by three different mechanisms, a) Direct current (DC) electron discharge, b) Radio frequency (RF) discharge, c) Microwave discharge. Although each mechanism has its own intricate advantages and disadvantages, the radiofrequency scheme is chosen for the ion thruster modelling. This is due to the several advantages that RF ion thrusters offer.

In comparison to the other plasma generation mechanisms, the RF thrusters yield the highest specific impulse and therefore contribute to significant mass savings. Also, the mass required for the Power Processing and Control Unit (PPCU) that supplies the power for the RF coils to generate the plasma is low. The complexity of the RF system is low and the lifetime is high. Electric propulsion systems have beam divergence which cause a reduction in thrust. RF ion thrusters nominally have a narrow beam divergence, thereby avoiding significant thrust loss. The operational domain is large and the stability of plasma as well the thrust is excellent throughout. RF ion thrusters provide excellent thrust control in terms of resolution, response, and reproducibility along with very low thrust noise [97, 146]. Additionally, it has the highest growth potential in the near future.

A performance model of an iodine-fueled inductively coupled miniature radiofrequency gridded ion thruster is implemented following Grondein et al [147] and Chabert et al [148] to determine the thrust, specific impulse, beam current and efficiencies.

A heat source is utilised to sublime the solid iodine and generate the I_2 vapour, which is then injected into the chamber. A cylindrical coil is wound around the plasma chamber and is excited with a radiofrequency (RF) power source. Electromagnetic fields are used to heat the plasma electrons which in turn ionize the neutral gas [88]. A magnetic field is induced in the chamber by the RF coils and there is no permanently applied field. The generated ions are accelerated by a set of DC biased grids.

The design and operational parameters for the performance model are listed in Table 3-7. The thruster diameter considered here is similar to that of the BIT-3 thruster [142]. A total mass flow rate of $48 \mu\text{g/s}$ is chosen and the mass flow to the neutralizer cathode is fixed at 10%. The DC grid voltage V_{grid} is set at 2000 V.

Table 3-7: RF thruster performance model parameters

Parameter	Value	Parameter	Value
Thruster radius, R	1.25 cm	Grid transparency, β	0.6 (ion) & 0.3 (neutral)
Thruster length, L	2.2 cm	Mass flow rate, \dot{m}_0	$48 \mu\text{g/s}$
Chamber volume, V	10.792 cm^3	Particle flow rate, Q_0	$1.14 \times 10^{17} \text{ s}^{-1}$
RF coil radius, R_c	1.3 cm	Molecular mass, \mathfrak{M}	253.8 (I_2) & 126.9 (I)
No. of coils, N	5	Grid voltage, V_{grid}	2000 V
Grid separation, s	1 mm	Coil resistance, \mathcal{R}_{coil}	0.7 Ω

3-6-1 Plasma generation and acceleration

3-6-1-1 Collision types and particle balance

The neutral gas I_2 is injected with a flow rate of Q_0 . The ionization process produces positive ions I^+ and I_2^+ , and negative ions I^- . Thrust is produced by the acceleration of I_2^+ and I^+ through the grids and I^- does not have any direct thrust contribution. Neutral gas thrust is produced by the fluxes of I_2 and I . A set of particle balance equations are written for all species in the model: e^- , I_2 , I , I^- , I^+ , I_2^+ to calculate their densities (n) as multiple processes take place in the plasma.

The processes that take place inside the plasma chamber are: elastic collisions between electrons and neutrals (*el*), excitation of neutrals by electrons (*exc*), ionization (*iz*), dissociative ionization (*dissiz*), dissociation (*diss*), dissociative attachment (*dissatt*), charge exchange (*cecx*), ion recombination (*ionrec*), and surface recombination (*sr*). The collision rate factors, K , for each of these processes as functions of the electron temperature \mathcal{T}_e are taken from Grondein et al [147].

The particle balance equations represent the evolution of particle number densities in the plasma chamber that occur due to the plasma processes. The chemical production rates due to plasma processes appearing in the species balances are:

- ▶ I ionization - $I + e^- \rightarrow I^+ + 2e^-$: $w_{iz,I} = K_{iz,I} n_e n_I$
- ▶ I_2 ionization - $I_2 + e^- \rightarrow I_2^+ + 2e^-$: $w_{iz,I_2} = K_{iz,I_2} n_e n_{I_2}$
- ▶ I_2 dissociative ionization - $I_2 + e^- \rightarrow I^+ + I + 2e^-$: $w_{dissiz} = K_{dissiz} n_e n_{I_2}$
- ▶ I_2 dissociation - $I_2 + e^- \rightarrow 2I + e^-$: $w_{diss} = K_{diss} n_e n_{I_2}$
- ▶ e^- - I_2 dissociative attachment - $I_2 + e^- \rightarrow I^- + I$: $w_{dissatt} = K_{dissatt} n_e n_{I_2}$
- ▶ I^- - I_2^+ charge exchange - $I_2 + I^+ \rightarrow I_2^+ + I$: $w_{cecx} = K_{cecx} n_{I^-} n_{I_2^+}$
- ▶ I^- - I^+ recombination : $w_{ionrec} = K_{ionrec} n_{I^-} n_{I^+}$
- ▶ I surface recombination - $I \rightarrow \frac{1}{2}I_2$: $w_{sr} = \frac{1}{8} n_I v_I \frac{\gamma_{sr}}{1-\gamma_{sr}} \frac{A_{sr}}{V}$

The surface recombination factor γ_{sr} is assumed be 0.02 [147]. The particle balance equations are expressed in equations. 3-23–3-28.

$$\dot{n}_e = w_{iz,I} + w_{iz,I_2} + w_{dissiz} - w_{dissatt} - \frac{(\Gamma_{I^+} + \Gamma_{I_2^+}) A_{eff}}{h_L V} \quad (3-23)$$

$$\dot{n}_{I_2} = \frac{Q_0}{V} - w_{dissiz} - w_{dissatt} - w_{iz,I_2} - w_{diss} + w_{cecx} + w_{sr} + \frac{\Gamma_{I_2^+} A_{eff1}}{h_L V} - \frac{1}{4} n_{I_2} v_{I_2} \frac{A_g}{V} \quad (3-24)$$

$$\dot{n}_I = w_{dissiz} + w_{dissatt} - w_{iz,I} + 2w_{diss} + 2w_{ionrec} + w_{cex} - 2w_{sr} + \frac{\Gamma_{I^+} A_{eff1}}{h_L V} - \frac{1}{4} v_I n_I \frac{A_g}{V} \quad (3-25)$$

$$\dot{n}_{I^-} = w_{dissatt} - w_{ionrec} - w_{cex} \quad (3-26)$$

$$\dot{n}_{I^+} = w_{iz,I} + w_{dissiz} - w_{ionrec} - \frac{\Gamma_{I^+} A_{eff}}{h_L V} \quad (3-27)$$

$$\dot{n}_{I_2^+} = w_{iz,I_2} - w_{cex} - \frac{\Gamma_{I_2^+} A_{eff}}{h_L V} \quad (3-28)$$

Here, the effective area for positive ion and electron wall losses A_{eff} is expressed in equation (3-29).

$$A_{eff} = 2\pi R^2 h_L + 2\pi RL h_R \quad (3-29)$$

The quantities h_L and h_R are edge-to-centre plasma density ratios, which are expressed in equation (3-30) [148].

$$h_L = 0.86 \left[\sqrt{3 + \frac{L (n_{I_2} + n_I) \sigma_i}{2}} \right]^{-1} \quad h_R = 0.8 \left[\sqrt{4 + R (n_{I_2} + n_I) \sigma_i} \right]^{-1} \quad (3-30)$$

Where σ_i is the global collision cross section with a value of 10^{-18}m^2 , The effective area for positive ion wall neutralization A_{eff1} and the area for I surface recombination are expressed in equations (3-31)– (3-32).

$$A_{eff1} = \pi R^2 (2 - \beta_i) h_L + 2\pi RL h_R \quad (3-31)$$

$$A_{sr} = \pi R^2 (2 - \beta_g) + 2\pi RL \quad (3-32)$$

Electrons are produced by ionization of I_2 and I, and are lost by dissociative attachment with I_2 and their flux to the chamber walls. Atomic I is produced by the dissociation, dissociative ionization and dissociative attachment of I_2 as well as ion-recombination between I^+ and I^- . It is lost by its ionization, wall recombination and ejection through the grids. Negative ions I^- are produced by dissociative attachment of I_2 and lost by ion-recombination and charge-exchange. Ionization of I and dissociative ionization of I_2 produce I^+ and they are lost by ion-recombination and ion flux through grids. Similarly, I_2^+ are produced by I_2 ionization and lost by charge exchange with I^- [147].

3-6-1-2 Gas heating

Neutral gas heating considers energy rates of elastic collisions of electrons–neutrals (Ω_{el}) and ions–neutrals (Ω_{in}) as well as thermal diffusion (q_{th}). The total gas energy $E_g = \frac{3}{2}(n_I + n_{I_2})\kappa_B\mathcal{T}_g$. The energy balance is given by equation (3-33).

$$\begin{aligned} \dot{E}_g = & \underbrace{3 \frac{m_e}{\mathfrak{M}_I} \kappa_B (\mathcal{T}_e - \mathcal{T}_g) n_e n_I K_{el,I}}_{\Omega_{el,I}} + \underbrace{3 \frac{m_e}{\mathfrak{M}_{I_2}} \kappa_B (\mathcal{T}_e - \mathcal{T}_g) n_e n_{I_2} K_{el,I_2}}_{\Omega_{el,I_2}} \\ & + \underbrace{\frac{1}{4} n_e (n_I \mathfrak{M}_I u_{Bohm,I^+}^2 K_{in,I} + n_{I_2} \mathfrak{M}_{I_2} u_{Bohm,I_2^+}^2 K_{in,I_2})}_{\Omega_{in}} - \underbrace{\kappa \frac{\mathcal{T}_g - \mathcal{T}_{g0}}{\Lambda_0} \frac{A_{surf}}{V}}_{q_{th}} \end{aligned} \quad (3-33)$$

Here, A_{surf} is the total surface area, κ is the thermal conductivity, κ_B is Boltzmann constant, Λ_0 is the heat diffusion length, and u_{Bohm,I_2^+} and u_{Bohm,I^+} are the ion Bohm velocities [147]. They are expressed in equations (3-34)– (3-35)

$$\Lambda_0 = \left[\sqrt{\left(\frac{2.405}{R}\right)^2 + \left(\frac{\pi}{L}\right)^2} \right]^{-1} \quad (3-34)$$

$$u_{Bohm,I_2^+} = \sqrt{\frac{\kappa_B \mathcal{T}_e}{\mathfrak{M}_{I_2}}} \quad ; \quad u_{Bohm,I^+} = \sqrt{\frac{\kappa_B \mathcal{T}_e}{\mathfrak{M}_I}} \quad (3-35)$$

The ion-neutral collision rate factors $K_{in} = \sigma_i v_i$, where v_i is the ion velocity expressed in equation (3-36)

$$v_i = \frac{8\kappa_B \mathcal{T}_i}{\pi \mathfrak{M}} \quad (3-36)$$

3-6-1-3 Electron power balance

Power (P_{RF}) supplied to the RF generator is partly absorbed by the plasma and partly dissipated at the coil. The absorbed power density p_{abs} is expressed in equation (3-37) and the coil power density p_{coil} is expressed in equation (3-38).

$$p_{abs} = \frac{1}{2} \mathcal{R}_{ind} I_{coil}^2 / V \quad (3-37)$$

$$p_{coil} = \frac{1}{2} \mathcal{R}_{coil} I_{coil}^2 / V \quad (3-38)$$

Here \mathcal{R}_{ind} is the resistance of an equivalent circuit composed of plasma and the coil [148]. The resistances are obtained using a transformer model based on Chabert et al [148]. The \mathcal{R}_{ind} is expressed using equation (3-39)

$$\mathcal{R}_{ind} = \frac{2\pi N^2}{L\omega\epsilon_0} \Re e \left[\frac{ikRJ_1(kR)}{\epsilon_p J_0(kR)} \right] \quad (3-39)$$

Here, k is the wave number and ϵ_p is the plasma complex permittivity. Wave number $k = k_0\sqrt{\epsilon_p}$ and $k_0 = \omega/c$, where ω is the oscillation frequency in radians per second, calculated using the signal frequency set at 13.6 MHz, and c is the speed of light. The complex permittivity ϵ_p is expressed in equation. 3-40

$$\epsilon_p = 1 - \frac{\omega_p^2}{\omega(\omega - i\nu_m)} \quad (3-40)$$

where $\omega_p = \sqrt{n_e e^2 / m_e \epsilon_0}$ is the plasma frequency and $\nu_m = n_I K_{el,I} + n_{I_2} K_{el,I_2}$. Quantities e and m_e are electron charge and mass, respectively, while ϵ_0 is the permittivity of free space. The electron power balance is given by equation. 3-41. The positive contribution comes from p_{abs} . The electron power is lost due to plasma processes (ionization, dissociation etc.), electron–neutral elastic collisions ($\Omega_{el,I}$ and Ω_{el,I_2}), and ion losses at walls (p_{wall}) and grids (p_{grid})[147].

$$\dot{E}_e = p_{abs} - p_{iz,I} - p_{iz,I_2} - p_{dissiz} - p_{dissatt} - p_{diss} - p_{exc,I} - \Omega_{el,I} - \Omega_{el,I_2} - p_{wall} - p_{grid} \quad (3-41)$$

$$\text{with, } p_{wall} = 7\kappa_B \mathcal{T}_e \left(u_{Bohm,I^+} n_{I^+} + u_{Bohm,I_2^+} n_{I_2^+} \right) \frac{A_{eff} - \pi R^2 h_L}{V}$$

$$p_{grid} = 6\kappa_B \mathcal{T}_e \left(u_{Bohm,I^+} n_{I^+} + u_{Bohm,I_2^+} n_{I_2^+} \right) \frac{A(1 - \beta_i)}{V}$$

The power $p_{iz,I} = E_{iz,I} w_{iz,I}$, where $E_{iz,I}$ is the ionization potential of I. Similarly, the rest of the terms are $p_{iz,I_2} = E_{iz,I_2} w_{iz,I_2}$, $p_{dissiz} = E_{dissiz} w_{dissiz}$, $p_{dissatt} = E_{dissatt} w_{dissatt}$, $p_{diss} = E_{diss} w_{diss}$ and $p_{exc,I} = E_{exc,I} w_{exc,I}$. The terms E_{iz,I_2} , E_{dissiz} , $E_{dissatt}$, E_{diss} , and $E_{exc,I}$ are the potentials of the corresponding plasma processes expressed in Joule. [149]. Equations 3-23–3-41 are integrated to obtain plasma properties from which the performance values are calculated. The particle densities and the electron temperature are illustrated in Figure 3-15

3-6-2 Performance

The thrust, I_{sp} , and beam current I_{beam} are calculated using ion and neutral fluxes (Γ_i and Γ_g), ion beam velocities ($v_{beam,i} = \sqrt{2eV_{grid}/\mathfrak{M}}$), effective grid area of ions ($A\beta_i$) and neutrals ($A\beta_g$), and the mass flow rate (\dot{m}_0). The total thrust is the sum of the thrust imparted by the accelerated ions and the thrust imparted by the neutrals that escape the grid. The total thrust is expressed in equation (3-42). Correspondingly, the specific impulse I_{sp} and the ion beam current I_{beam} are expressed in equation (3-43)

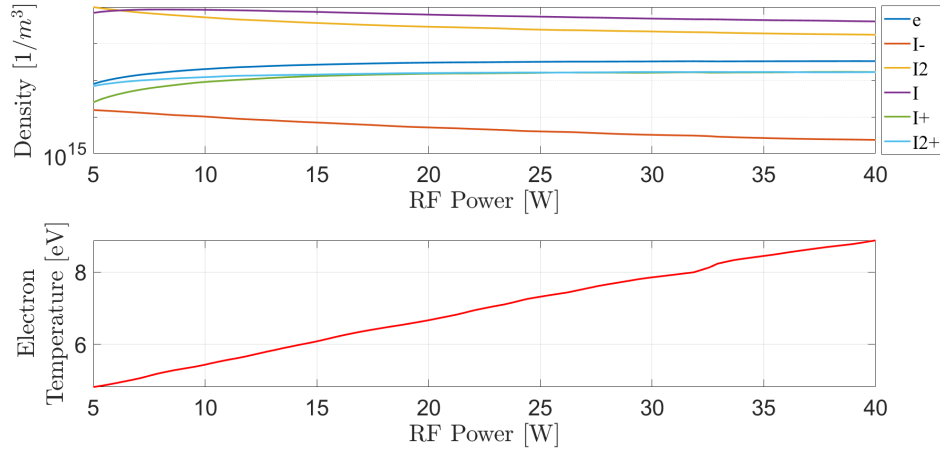


Figure 3-15: Particle densities and electron temperature

$$T = \Gamma_i \mathfrak{M} v_{beam,i} A \beta_i + \Gamma_g \mathfrak{M} v_g A \beta_g \quad (3-42)$$

$$I_{sp} = \frac{T}{\dot{m}_0 g_0} \quad I_{beam} = e \Gamma_i A \beta_i \quad (3-43)$$

The ion and neutral fluxes, Γ_i and Γ_g are expressed in equations (3-44) and (3-45), respectively.

$$\Gamma_i = h_L u_{Bohm,i} n_i \quad (3-44)$$

$$\Gamma_g = \frac{1}{4} v_g n_g \quad (3-45)$$

They are calculated using positive ion and neutral densities (n), ion Bohm velocities ($u_{Bohm,i}$), edge-to-centre plasma density ratio (h_L), and neutral gas velocities ($v_g = \sqrt{8 \kappa_B \mathcal{T}_g / \pi \mathfrak{M}}$) [148]. The fluxes are calculated for ions I_2^+ and I^+ , and neutrals gases I_2 and I . The molecular mass \mathfrak{M} is 253.8 amu for I_2 and 126.9 amu for I .

The input RF power, P_{RF} , supplied to the coils is adjusted according to the available thruster input power, P_{in} (see Figure 3-14). Fluxes Γ_i and Γ_g , and subsequently the powers $P_{beam,i}$ and P_g , depend upon P_{RF} . A simplified neutralizer cathode model based on Richardson's Law of thermionic emission is implemented to calculate the power, P_{cath} , required for ion beam neutralization [88]. The emitter is assumed to be composed of a tungsten filament coated with barium oxide. The emitter temperature is set at $\mathcal{T}_{em} = 1300$ K and the efficiency is assumed to be $\eta_{em} = 0.3$ [150]. According to Richardson's law, the emitter current density for a barium oxide - tungsten (BaO-W) emitter filament is given by equation (3-46). The corresponding cathode power is given by equation (3-47).

$$J_{em} = 1.2 \times 10^6 \mathcal{T}_{em}^2 \exp \left[\frac{-1.67 + 2.82 \times 10^{-4} \mathcal{T}_{em}}{\kappa_{B,eV} \mathcal{T}_{em}} \right]. \quad (3-46)$$

$$P_{cath} = \frac{I_{beam} \sigma_{sb} \mathcal{T}_{em}^4}{J_{em} \eta_{em}} \quad (3-47)$$

Where, $\sigma_{sb} = 5.67 \times 10^{-8} \text{W/m}^2 \text{K}^4$ is the Stefan-Boltzmann constant. It has to be noted that the Boltzmann constant here is $\kappa_{B,eV} = 8.61 \times 10^{-5} \text{eV/K}$. The ion beam power $P_{beam,i}$, the neutral gas thrust power P_g , and the total power P_{th} is expressed in equations (3-48) and (3-49), respectively.

$$P_{beam,i} = I_{beam,i} V_{grid} = e \Gamma_i A \beta_i V_{grid} \quad ; \quad P_g = \frac{1}{2} \mathfrak{M} v_g^2 \Gamma_g A \beta_g \quad (3-48)$$

$$P_{tot} = P_{beam,i} + P_g + P_{cath} + P_{RF} \quad (3-49)$$

The variations of thrust, I_{sp} and η with power are illustrated in Figure 3-16. As the input power increases, the power absorbed by the plasma increases. This results in an increase in ion flux and consequently the thrust. The required neutralization power is 0.63–0.5% of the total power. The mass utilisation efficiency increases and the thruster power efficiency decreases with the increase in power. The thruster performance values are listed in Table 3-8.

Thruster power efficiency (η_p) is calculated using ion beam power $P_{beam,i}$, neutral thrust power P_g and neutralizer cathode power P_{cath} . The mass utilisation efficiency (η_m) is the ratio of ejected ion flow rate ($\Gamma_i A \beta_i$) and injected gas flow rate (Q_0). Total efficiency is the product of η_p and η_m .

$$\eta_p = \frac{P_{beam,i} + P_g}{P_{beam,i} + P_g + P_{cath} + P_{RF}} \quad \eta_m = \frac{\Gamma_i A \beta_i}{Q_0} \quad \eta_{tot} = \eta_p \eta_m \quad (3-50)$$

Table 3-8: RF thruster performance at maximum power (67 W)

Parameter	Value	Parameter	Value
Max Thrust, T_{max}	1.492 mN	Mass utilisation efficiency, η_m	90.33%
Max I_{sp}	3168 s	Power efficiency, η_p	49.2%
Max Beam Current, I_{beam}	16.5 mA	Total efficiency, η_{tot}	44.44%

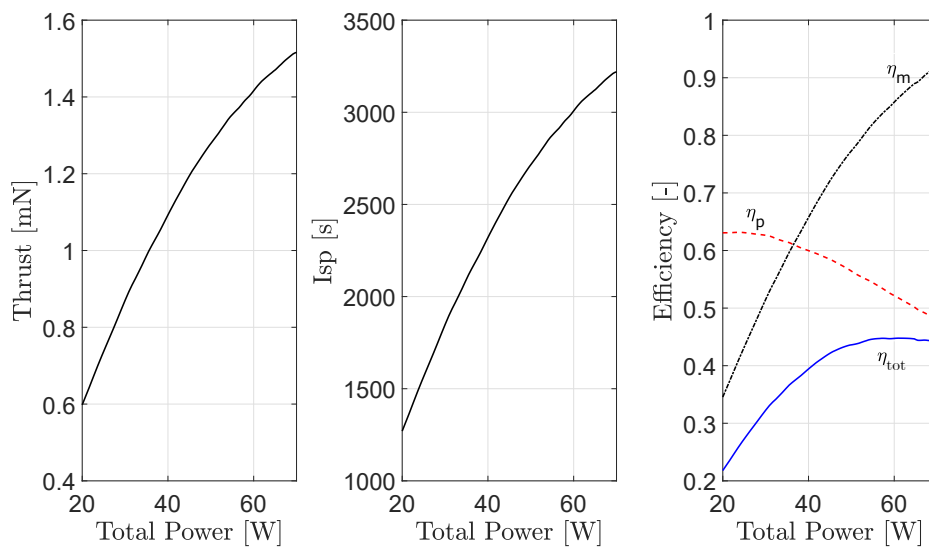


Figure 3-16: Thrust, I_{sp} and efficiencies vs total power

3-7 Low-thrust trajectory optimisation

Earth–Mars transfer trajectory optimisation is performed to target a defined ballistic capture point at a set epoch [18, 151]. As the Sun-spacecraft distance increases, the available power decreases and the thruster performance is affected (see section 3-6-2). The spacecraft departs from a distance of 0.01 AU from Earth (Hill sphere radius), outward on the Sun–Earth line. An optimal control problem is solved to minimize a cost function, namely flight time (time-optimal) or propellant consumption (fuel-optimal). Once the spacecraft reaches the capture point, it acquires a highly irregular Mars orbit just by virtue of the natural attractions of Sun and Mars [18]. Optimisation involves real solar system dynamics and solar radiation pressure (SRP) [151, 152].

3-7-1 Statement of the problem

This section states the Earth–Mars transfer culminating in a ballistic capture as an optimal control problem. The spacecraft uses the low-thrust electric propulsion system to manoeuvre. The gravitational attraction of the Sun is the main force and other dynamics such as third body perturbations and Solar Radiation Pressure (SRP) are considered as well. The force of the engine will have the second largest magnitude behind that of the Sun, except in cases where the spacecraft is near Earth or Mars.

3-7-1-1 Reference frames

The trajectory optimisation shall use different reference frames according to the scenario. For the heliocentric transfer, the ephemerides will be retrieved from the Heliocentric Earth Orbital frame at epoch t_d (HEO@ t_d), where t_d is the departure epoch. This frame is an inertial reference frame, centred at the Sun with its axes defined as:

- ▶ +x axis: aligned to the Sun–Earth line at t_d and points in the direction of the Earth.
- ▶ +z axis: aligned with the angular momentum of the Earth w.r.t the Sun at t_d and points along this vector.
- ▶ +y axis: completes the right handed frame.

The ballistic capture at planets is analysed with reference frames that are directly related to the orbital plane of the target planet. Thus, to study the movement of a spacecraft around Mars, another reference frame called the Radial Tangential Normal frame is defined at epoch t_0 (RTN@ t_0), where t_0 is the arrival time at the ballistic capture point. This frame is also inertial and is centred at Mars. The axes are defined as:

- ▶ +x axis: aligned with Sun–Mars line at t_0 and points in the direction opposite to the Sun.
- ▶ +z axis: aligned to the angular momentum of the Sun w.r.t Mars and points along this vector.

- ▶ +y axis: completes the right handed frame.

The third reference frame called the Spacecraft Radial Tangential Normal (SRTN) is used to define the velocity of the spacecraft (but not the position). It is similar to RTN@ t_0 but rotates about the centre of the spacecraft.

- ▶ +x axis: aligned with Sun–spacecraft line and points in the direction opposite to the Sun.
- ▶ +z axis: aligned to the angular momentum of the spacecraft w.r.t the Sun and points along this vector.
- ▶ +y axis: completes the right handed frame.

The reference frames are illustrated in Figure 3-17. It also shows the definition of the spherical coordinates that will be used for describing the position of the spacecraft in HEO@ t_d . Spherical coordinates and SRTN are used to ensure the slow variation of the state variables, since it allows for a more efficient solution [153].

3-7-1-2 Spacecraft dynamics

Ballistic capture is a phenomenon that occurs due to the natural gravitational forces of multiple bodies acting on the spacecraft. To design the ballistic capture at Mars, at least the point mass gravitational influence of Mars and the Sun must be modelled. Luo et al [154] utilised restricted n -body problem to generate the ballistic captures. Thus, one can use the equations of motion of a massless particle under the influence of $n - 1$ bodies in a non-rotating reference frame centered at one of the bodies. To increase the accuracy of dynamics, the SRP is added to the model. The equation of motion is expressed in equation (3-51).

$$\frac{d^2 \vec{r}}{dt^2} = -\mu \frac{\vec{r}}{r^3} - \sum_{i \in \mathbb{P}} \mu_i \left(\frac{\vec{r}_i}{r_i^3} - \frac{\vec{r}_i - \vec{r}}{\|\vec{r}_i - \vec{r}\|^3} \right) + \frac{Q}{z} \frac{\vec{r} - \vec{r}_s}{\|\vec{r} - \vec{r}_s\|^3} \equiv \vec{f}_{2B} + \vec{f}_{TB} + \vec{f}_{SRP} \quad (3-51)$$

Here, \vec{r} is the position vector of the spacecraft w.r.t the body at the origin of the reference frame, r is the magnitude of \vec{r} , μ is the gravitational parameter of the central body, \mathbb{P} is the set of $n - 2$ bodies each referencing to a perturbing body (a body other than the central one), \vec{r}_i is the position vector of body i w.r.t the origin of the reference frame, and r_i is the magnitude of \vec{r}_i , μ_i is the gravitational parameter of the body i . The parameter \vec{f}_{2B} is the 2-body dynamics which is the main force on the right hand side and \vec{f}_{TB} refers to the summation of the perturbation terms. The contribution of SRP is expressed in equation (3-52).

$$\vec{f}_{SRP} = \frac{Q}{z} \frac{\vec{r} - \vec{r}_s}{\|\vec{r} - \vec{r}_s\|^3} \quad Q = \frac{L_s C_R}{4\pi c} \quad z = \frac{m_0}{A} \quad (3-52)$$

Here, L_s is the luminosity of the sun with a value of 3.8458×10^{26} W, C_R is the reflectivity constant, c is the speed of light, A is the exposed area of the spacecraft to the Sun, and m_0 is the spacecraft mass.

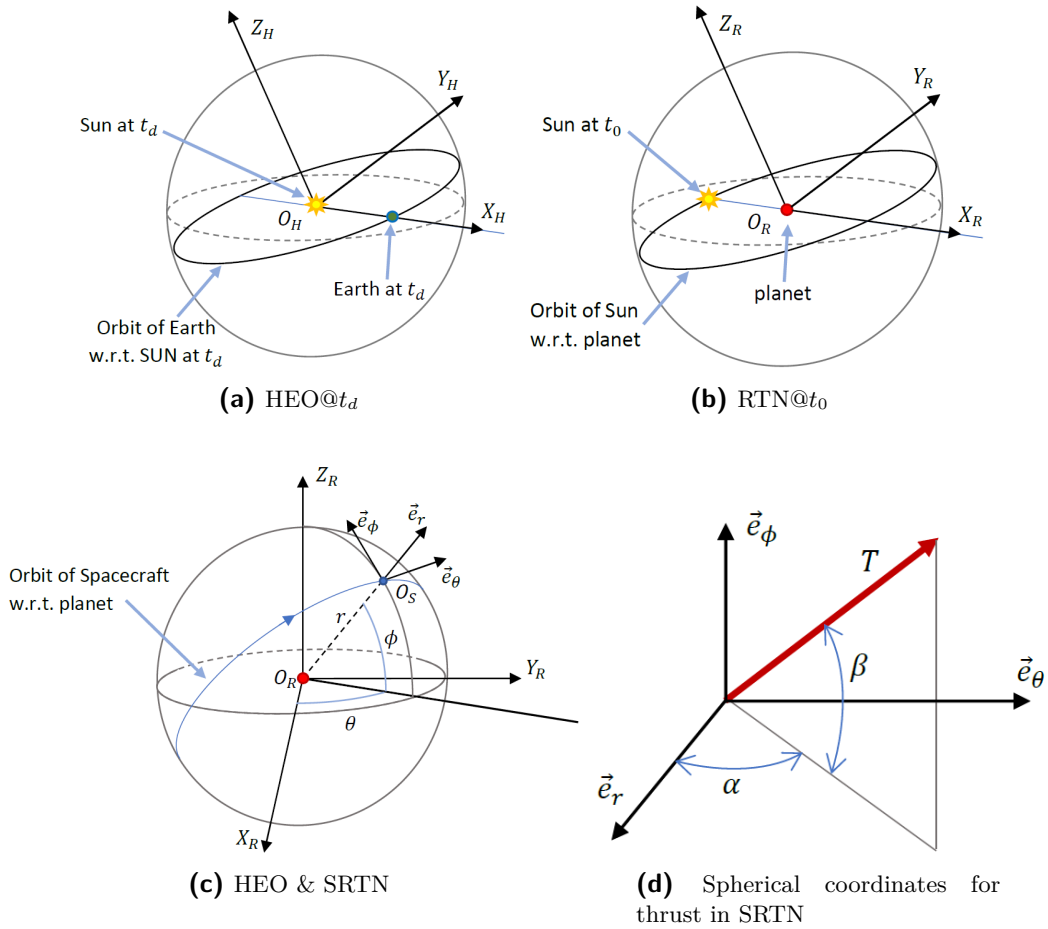


Figure 3-17: Orientation of the HEO@ t_d frame with O_H as its origin is shown in Figure (a). The RTN@ t_0 frame with the origin at O_R is shown in Figure (b). The orientation of HEO@ t_d (origin O_H) and the SRTN frames (origin at O_S) are shown along with the spherical coordinates of the spacecraft in HEO@ t_d frame (r, θ, ϕ) are shown in Figure (c). The spherical coordinates of the thrust in the SRTN frame is shown in Figure (d)

The only unknown parameter in equation (3-51) is the position of the spacecraft \vec{r} . The ephemerides of the rest of the bodies ($n - 2$) on the RHS of the equation (3-51), i.e. \vec{r}_i , will be retrieved from the SPICE toolkit file SPK de430.bsp [155].

3-7-2 Optimal control problem

The equations of motion of the spacecraft are written in the HEO@ t_d with the Sun as the source of the main force acting on the spacecraft, along with secondary forces such as the SRP and the gravitational attraction of the barycentre of all the planets. The equations of motion are then represented using (3-53).

$$\frac{d}{dt} \begin{bmatrix} r \\ \theta \\ \phi \end{bmatrix} \equiv \begin{bmatrix} \dot{r} \\ \dot{\theta} \\ \dot{\phi} \end{bmatrix} = \begin{bmatrix} v_r \\ \frac{v_\theta}{r \cos \phi} \\ \frac{v_\phi}{r} \end{bmatrix} \quad (3-53)$$

$$\frac{d}{dt} \begin{bmatrix} v_r \\ v_\theta \\ v_\phi \end{bmatrix} \equiv \begin{bmatrix} \dot{v}_r \\ \dot{v}_\theta \\ \dot{v}_\phi \end{bmatrix} = \mathcal{P} (\vec{f}_{2B} + \vec{f}_{TB} + \vec{f}_{SRP}) + \mathcal{S} \begin{bmatrix} v_r \\ v_\theta \\ v_\phi \end{bmatrix} \quad (3-54)$$

$$\mathcal{P} \equiv \begin{bmatrix} \cos \phi \cos \theta & \cos \phi \sin \theta & \sin \phi \\ -\sin \theta & \cos \theta & 0 \\ -\sin \phi \cos \theta & -\sin \phi \sin \theta & \cos \phi \end{bmatrix} \quad \mathcal{S} \equiv \begin{bmatrix} 0 & \dot{\theta} \cos \phi & \dot{\phi} \\ -\dot{\theta} \cos \phi & 0 & \dot{\theta} \sin \phi \\ -\dot{\phi} & -\dot{\theta} \sin \phi & 0 \end{bmatrix} \quad (3-55)$$

Here, \vec{f}_{2B} and \vec{f}_{SRP} are written in a non-rotating reference frame, thus their expression is the same as in equations (3-51) and (3-52). The matrices \mathcal{P} and \mathcal{S} are transformation matrices. Since the spacecraft uses the thrust of the electric propulsion system, this contribution should also be included in the dynamics. The force per unit mass \vec{f}_T is expressed in equation (3-56).

$$\vec{f}_T = \frac{T}{m} \begin{bmatrix} \sin \alpha \cos \beta \\ \cos \alpha \cos \beta \\ \sin \beta \end{bmatrix} \quad (3-56)$$

where α and β are the azimuth and elevation angles of thrust, respectively, in the spherical coordinates of the SRTN frame. Since it is already defined in the rotating frame, \vec{f}_T can be added directly to the RHS of equation (3-54). The mass of the spacecraft depends upon the thrust (T) and specific impulse (I_{sp}), which are calculated in section 3-6-2. It is expressed in equation (3-57):

$$\frac{dm}{dt} = -\frac{T}{I_{sp} g_0} \quad (3-57)$$

The overall state vector $\vec{x} \equiv \{r, \theta, \phi, v_r, v_\theta, m\}$ and the control $\vec{u} \equiv \{T, \alpha, \beta\}$. The full set of equations of motion will then be:

$$\frac{d\vec{x}}{dt} = \begin{bmatrix} v_r \\ \frac{v_\theta}{r \cos \phi} \\ \frac{v_\phi}{r} \\ \mathcal{P} (\vec{f}_{2B} + \vec{f}_{TB} + \vec{f}_{SRP}) + \mathcal{S} \begin{bmatrix} v_r \\ v_\theta \\ v_\phi \end{bmatrix} + \vec{f}_T \\ -\frac{T}{I_{sp} g_0} \end{bmatrix} \equiv \vec{\mathcal{F}} [\vec{x}(t), \vec{u}(t), t] \quad (3-58)$$

3-7-2-1 Boundary conditions

The boundary conditions are also written in the reference frames expounded in section 3-7-1-1. The spacecraft departs from Earth's sphere of influence $R_{SOI,E}$ with a zero relative velocity w.r.t the Earth at t_d and arrives at the ballistic capture target point at t_f . The initial point is aligned with the Sun–Earth line and in opposition to the Sun. The time at which the spacecraft arrives at the first periapsis about Mars is designated as t_0 (see Figure 3-18). The time t_f is free to be optimised.

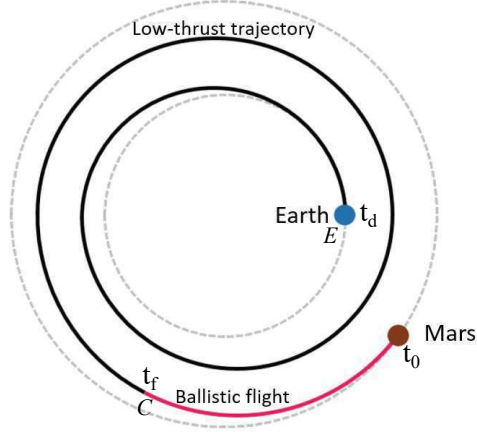


Figure 3-18: Hypothetical low-thrust trajectory and ballistic capture

The departure and arrival boundary conditions are expressed in equations (3-59), (3-60) and (3-61).

$$\Psi_d [\vec{x}_d(t_d), t_d] \equiv \begin{bmatrix} t_d - [t_0 - \Delta t_{TOF}] \\ r(t_d) - [r_E(t_d) + R_{SOI,E}] \\ \theta(t_d) \\ \phi(t_d) \\ v_r(t_d) - v_{rE}(t_d) \\ v_\theta(t_d) - v_{\theta E}(t_d) \\ v_\phi(t_d) \\ m(t_d) - m_{wet} \end{bmatrix} = \vec{0} \quad (3-59)$$

$$\Psi_f [\vec{x}(t_f)] \equiv \begin{bmatrix} r(t_f) - [r_C(t_f)] \\ \theta(t_f) - [\theta_C(t_f) - 2\pi\Delta n] \\ \phi(t_f) - \phi_C(t_f) \\ v_r(t_f) - v_{rC}(t_f) \\ v_\theta(t_f) - v_{\theta C}(t_f) \\ v_\phi(t_f) - v_{\phi C}(t_f) \end{bmatrix} = \vec{0} \quad (3-60)$$

$$\Psi_t(t_f) \equiv t_f - t_\infty \leq 0 \quad (3-61)$$

Here, t_0 is picked based on the capture sets generated by Aguiar [151]. The parameter Δt_{TOF} is the total time of flight (TOF), which is [1200,2200] days chosen with a step of 50 days.

It is defined as $\Delta t_{TOF} = t_0 - t_d$ and not $t_f - t_d$. Earth and the capture point are defined with subscripts E and C , respectively. The spacecraft has to target the point C which shall lead to the capture at Mars at t_0 . The position $\vec{x}_E(t_d)$ is retrieved from the SPICE Satellite and Panel Kernel de430.bsp file available in the toolkit [155]. The parameter Δn controls the number of extra revolutions that the spacecraft performs in the heliocentric orbit w.r.t the ballistic capture point. This can be picked among $[0,1,2,3]$. The time t_f is restricted to be less than the time t_∞ at which the spacecraft first enters the Mars sphere of influence. The wet mass of the spacecraft at the beginning of the transfer is expressed as m_{wet} . The final mass of the spacecraft is free to evolve, however, it must not be less than that of the initial mass.

3-7-2-2 Constraints and objective function

The path constraints of the bounds need to be specified for the optimisation problem. They are expressed in equation (3-62).

$$\mathcal{G}[\vec{x}(t), \vec{u}(t)] \equiv \begin{bmatrix} T(t) - T_{max} \\ T(t) - T_{av}(r) \\ \alpha(t) - \alpha_{max} \\ \alpha_{min} - \alpha(t) \\ \beta(t) - \beta_{max} \\ \beta_{min} - \beta(t) \\ m(t) - m_{wet} \end{bmatrix} \leq \vec{0} \quad (3-62)$$

The inequality constraints pertaining to the thrust are written separately because there is a discontinuity in the maximum power supplied to the thrust, upon which the thrust depends on (see Figure 3-14): once the thruster input power starts decreasing with the Sun-spacecraft distance and drops below the maximum power line, the available thrust (T_{av}) also starts decreasing and the second constraint kicks in. The variation of T with r can be directly obtained by comparing the plots in Figures 3-14 and 3-16 and performing a polynomial curve fit.

The optimisation of the trajectory is done to minimise either the time of flight or the fuel consumption, as mentioned earlier in this section. The departure epoch t_d and the mass of the spacecraft at the departure point m_d are fixed. The objective functions are expressed in equation (3-63).

$$J = \begin{cases} t_f & \text{time optimal} \\ -m_f & \text{fuel optimal} \end{cases} \quad (3-63)$$

In time-optimal solution, the thrust $T = T_{max}(r)$ always. In fuel optimal solution, thrust switches between $T = 0$ and $T = T_{max}(r)$. It has to be noted that for transfers culminating in ballistic capture, the minimisation index $J = t_f$ *minimises the actual powered time of flight rather than the total time of flight*. The total time of flight Δt_{TOF} is fixed. The powered time of flight $\Delta t_{TOF,pow} = t_f - t_d$. To find the global minimum Δt_{TOF} solutions, a parametric analysis needs to be done.

3-7-3 Numerical scheme and solver

Topputo et al [153] have presented a method in which they utilise a direct collocation method to transcribe the optimal control problem to a Non-Linear Programming (NLP) problem. Since the amount of spirals for an Earth–Mars transfer is low, the use of a direct method to transcribe the optimal control problem into an NLP requires less parameters for the representation of states and controls variation with time. Additionally, direct methods have a better convergence properties. Further details regarding the methods are expounded in Topputo et al [153] and Aguiar [151].

An in-house MATLAB code called DIRect collocation Tool for Trajectory Optimization (DIRETTO) is utilised for transcription of the problem and supply the NLP solver with the desired inputs [153]. The time interval $[t_d, t_f]$ is discretized into N nodes (interval) and the control \vec{u} is approximated by a linear function at each subinterval (k). States \vec{x} are approximated by defect constraints ζ . The transcribed NLP problem is expressed in equations (3-64)– (3-69)

$$t_d = t_1 < t_2 < t_3 \dots < t_{N-1} < t_N < t_f \quad (3-64)$$

$$u(t_k) \equiv u_k \quad (3-65)$$

$$x(t_k) \equiv x_k \quad (3-66)$$

$$t_k \leq t \leq t_{k+1} \quad (3-67)$$

$$u(t) \equiv u_k + \frac{t - t_k}{t_{k+1} - t_k} (u_{k+1} - u_k) \quad (3-68)$$

$$\zeta_k (x_k, x_{k+1}, u_k, u_{k+1}, t_k, t_{k+1},) = 0 \quad (3-69)$$

Hermite-Simpson method is then used to construct the defect constraints [153].

$$\zeta_k \equiv x_{k+1} - x_k - \frac{h_k}{6} (F_k + F_c + F_{k+1}) \quad (3-70)$$

$$F_k \equiv F(x_k, u_k, t_k) \quad (3-71)$$

$$F_c \equiv F(x_c, u_c, t_c) \quad (3-72)$$

$$F_{k+1} \equiv F(x_{k+1}, u_{k+1}, t_{k+1}) \quad (3-73)$$

$$x_c = \frac{1}{2}(x_k + x_{k+1}) + \frac{h}{8}(F_k - F_{k+1}) \quad (3-74)$$

$$t_c \equiv t_k + \frac{h}{2} \quad (3-75)$$

$$h \equiv t_{k+1} - t_k \quad (3-76)$$

$$u_c \equiv u(t_c) = \frac{1}{2}(u_k + u_{k+1}) \quad (3-77)$$

The NLP problem is solved using an interior point method. The number of nodes used in the NLP problem will be $N = 400$. This interior point algorithm is particularly suited for solving this problem since it is large and sparse. Tolerances are set for steps, constraints and first order optimality. Step tolerance is 10^{-6} , constraints tolerance is 10^{-12} , and the first order optimality and function value tolerances are 10^{-6} .

Since the difference in the order of the optimisation variables is large, some scaling parameters are used. Distances are scaled with length unit $LU = 1 \text{ AU}$. The time is scaled using the time unit $TU = \sqrt{LU^3/\mu_{sun}}$, and the mass is scaled using the mass unit $MU = m_0$.

3-7-4 Heliocentric trajectory

The mass of the spacecraft after high-thrust Earth escape is 27.447 kg (see Table 2-10). For the time-optimal transfer, the Δt_{TOF} value is set at 1250 days and for the fuel-optimal transfer the Δt_{TOF} is set at 1350 days. It has to be mentioned again that the optimized value of the time is the powered time of flight $\Delta t_{TOF,pow} = t_f - t_d$. The thruster performance obtained in section 3-6-2 is utilised in the dynamics and subsequently in the optimisation.

The transfer trajectories and the variations of heliocentric eccentricity and semi-major axis for time-optimal and fuel-optimal transfers are illustrated in Figure 3-19. In the time-optimal solution, the transfer is achieved within 1250 days (~ 3.28 years) and the powered time of flight $\Delta t_{TOF,pow}$ is 1186.83 days (~ 3.234 years) with a propellant consumption of 4.892 kg. The fuel-optimal solution is achieved within the total transfer time of 1350 days (3.83 years) and the $\Delta t_{TOF,pow}$ is 1334.48 days. The total thrusting time (where the thruster is operating at $T_{max}(r)$) is 1090.9 days and the corresponding propellant consumption of 4.492 kg.

The variations of T and I_{sp} for time-optimal and fuel-optimal transfers are illustrated in Figure 3-20. The quantities α and β pertain to the azimuthal and elevation thrusting angles, defined in the SRTN frame (see Figure 3-17). In the fuel-optimal transfer, the thruster is intermittently switched on and off to save propellant mass. It has to be noted that this bang-bang profile is not imposed a priori but rather found ex-posteriori, thus confirming the appropriateness of the solver. The overall parameters for the time-optimal and fuel-optimal solutions are shown in Table 3-9.

Table 3-9: Comparison of time-optimal and fuel-optimal heliocentric transfers

	Time-optimal	Fuel-optimal
ΔV	5.837 km/s	5.330 km/s
Propellant mass, m_p	4.892 kg	4.492 kg
Total time, Δt_{TOF}	1250 days	1350 days
Powered flight, $\Delta t_{TOF,pow}$	1186.83 days	1334.48 days
Thruster operation time	1186.83 days	1090.9 days

The state variables of the time-optimal and fuel-optimal solutions are illustrated in Figure 3-21.

For the given total transfer time requirements, the mass savings of the fuel-optimal technique is 0.4 kg for an additional 100 day flight time. The penalty in flight time is considered quite high for the achieved mass saving. Thus, time-optimal transfer is selected.

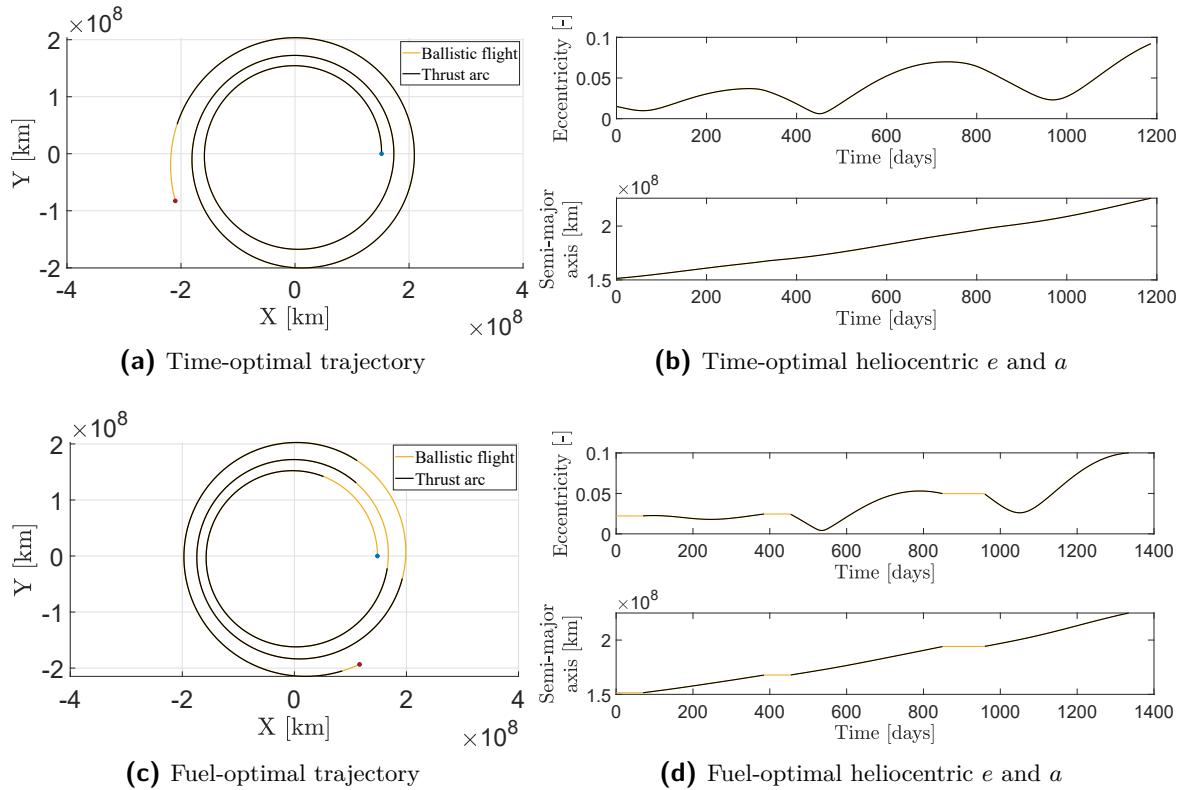


Figure 3-19: Spacecraft heliocentric trajectory, eccentricity e and semi-major axis a variation in time-optimal and fuel-optimal solutions.

3-7-5 Ballistic capture and circularization

The spacecraft enters a highly irregular orbit about Mars after ballistic capture, which is temporary and some energy needs to be dissipated to stabilise it. The ballistic capture sets are generated using an in-house MATLAB tool, GRAvity TIdal Slide - GRATIS [152]. The mass of the spacecraft after time-optimal heliocentric transfer is 22.555 kg. The orbit parameters at the point of capture are listed in Table 3-10 and are obtained from Aguiar [151].

This orbit is highly inefficient for the scientific observation mission. Energy dissipation, stabilization, and circularization to a 60000 km orbit are pursued to perform the science mission. The start epoch is set and the chemical propulsion module, with 3 N thrust, provides a retrodirectional ΔV of 45 m/s for stabilization and initial eccentricity reduction. This is done to reduce the overall circularization time since low-thrust propulsion alone would take several years. The orbit parameters after the chemical burn are $\{a, e, i, \Omega, \omega, \theta\} = \{86876 \text{ km}, 0.9499, 22.5^\circ, 360^\circ, 325.8^\circ, 17.88^\circ\}$. The chemical propellant mass consumption for this stabilization manoeuvre is 0.418 kg (Table 2-10). This serves as the initial point for low-thrust circularization.

To circularize to a 60000 km orbit, multiple techniques can be used. The simplest technique to decelerate the spacecraft when closer to Mars (i.e., $r < a$) to reduce the apoapsis and accelerated when farther away from Mars ($r > a$) to increase the periapsis. This is done until

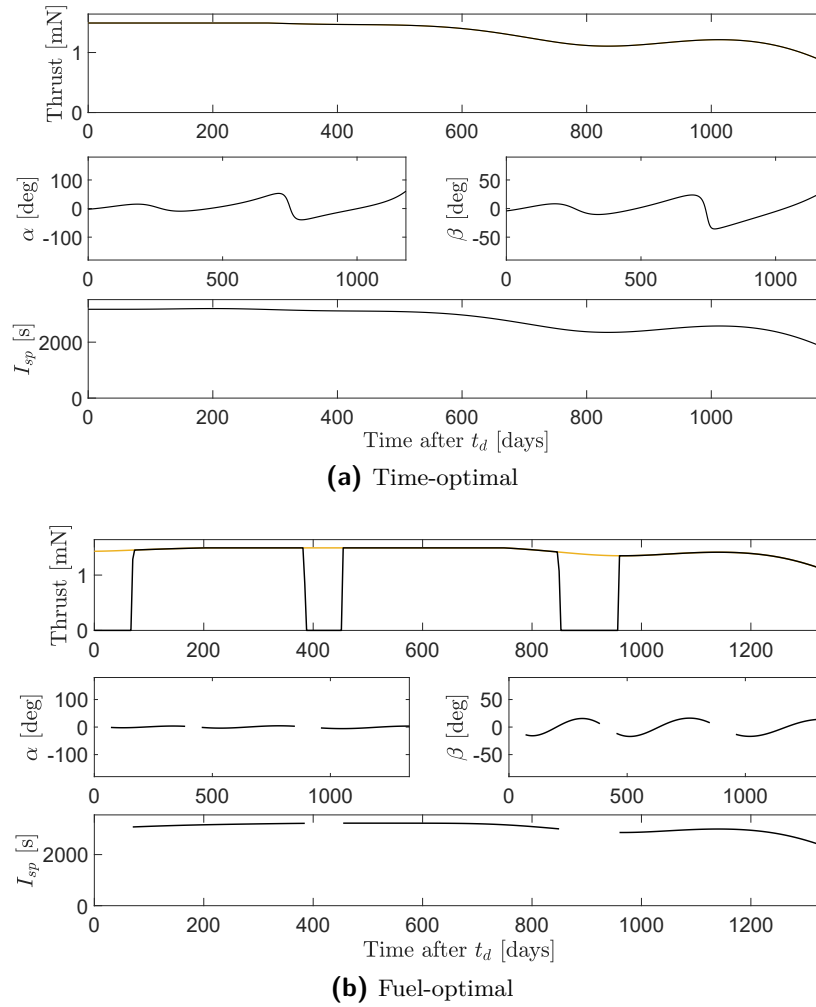
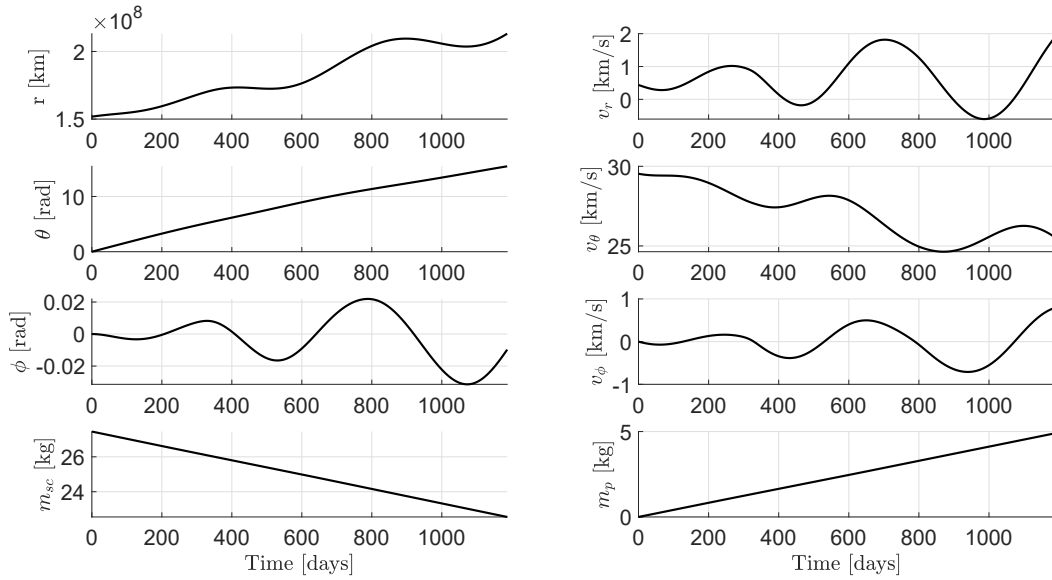


Figure 3-20: Thrust and I_{sp} variations over time for time-optimal and fuel-optimal solutions of heliocentric transfer

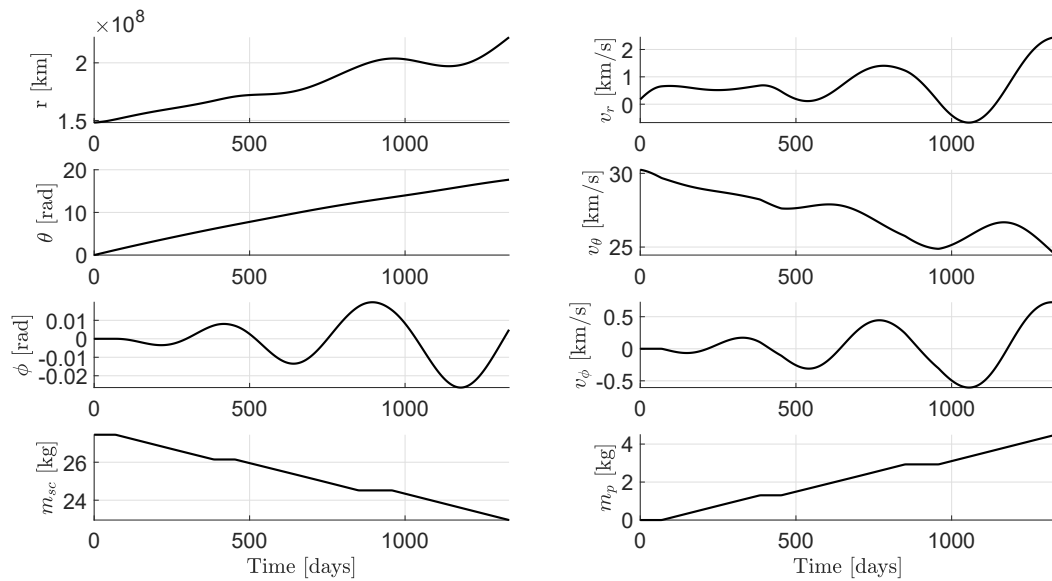
Table 3-10: Parameters at Mars after ballistic capture

Parameter	Value
Periaerion r_{p0}	4346 km
a_0	434600 km
e_0	0.99
i_0	22.5°
Ω_0	0°
ω_0	326°
θ_0	0°
Epoch t_0	08 May 2024 12:36:08.640 UTC
m_0	22.555 kg (time-opt) & 22.955 kg (fuel-opt)

the orbit is circularized at a certain semi-major axis. Then the semi-major axis is reduced



(a) Time-optimal



(b) Fuel-optimal

Figure 3-21: Variation of state variables with time for time-optimal and fuel-optimal solutions

to the desired value through a constant deceleration and finally, the eccentricity is corrected [156]. The results of this technique were presented in Mani et al [28].

However, a more efficient control law was required such that the circularization time and subsequently the propellant mass required are reduced. A law that uses a proximity quotient Q , which measures the similarity of the current osculating orbit and the target orbit is utilised. The implementation of the Q -law follows the description given by Petropoulos [157]. The proximity quotient is expressed in equation (3-78).

$$Q = (1 + W_p P) \sum_{oe} W_{oe} S_{oe} \left| \frac{d(oe, oe_t)}{\tilde{o}\tilde{e}} \right|^2 \quad \text{for } oe = a, e, i \quad (3-78)$$

For the circularization, only three parameters are of interest, the semi-major axis a , the eccentricity e and the inclination i . Naturally, equation (3-78) could be extended to right ascension of the ascending node and the argument of periapsis. The values W_p and W_{oe} are weights whose values are $W_p = 1$, $W_a = 10$, $W_e = 3$, and $W_i = 1$.

P is the penalty function that prevents the spacecraft from reaching infeasible periapsis radius values, for example, Mars atmospheric entry. It is expressed in equation (3-79)

$$P = \exp \left[K \left(1 - \frac{r_p}{r_{p,min}} \right) \right] \quad (3-79)$$

Here, K is a scalar and $r_{p,min}$ is the minimum value of the periapsis radius. In equation (3-78), S_{oe} is the scaling function that prevents discrepancies among the weights of orbital elements. It especially prevents the semi-major axis from reaching values that are far greater than the rest of the elements.

$$S_{oe} = \begin{cases} \left[1 + \left(\frac{a-a_T}{\mathfrak{p} a_T} \right)^{\mathfrak{q}} \right]^{1/\mathfrak{s}} & \text{for } a \\ 1 & \text{for } e, i \end{cases} \quad (3-80)$$

Here, $\mathfrak{p} = 3$, $\mathfrak{q} = 4$, and $\mathfrak{s} = 2$ are constants. The distance function $d(oe, oe_T = oe - oe_T$ for $oe = a, e, i$. The maximum rate of change of orbital elements oe over the thrust direction and true anomaly are measured by $\tilde{o}\tilde{e}_{xx}$

$$\tilde{o}\tilde{e}_{xx} = \max_{\alpha, \beta, \theta} (\dot{o}e) \quad (3-81)$$

where θ is the true anomaly, and α and β are the azimuth and elevation angles of thrust, respectively.

Gauss's form of variational equations of motion are used to express $\tilde{o}\tilde{e}_{xx}$. The corresponding variations of a , e and i are expressed in equations (3-82), (3-83), and (3-84), respectively[157].

$$\dot{a}_{xx} = 2T \sqrt{\frac{a^3(1+e)}{\mu(1-e)}} \quad (3-82)$$

$$\dot{e}_{xx} = \frac{2pT}{h} \quad (3-83)$$

$$\dot{i}_{xx} = \frac{pT}{h \sqrt{1 - e^2 \sin^2 \omega - e |\cos \omega|}} \quad (3-84)$$

The thrust magnitude is represented by T , p is the semilatus rectum, and h is the specific angular momentum of the spacecraft. The quotient Q is constructed in such a way that it

takes positive values always except at the target orbit, where it is zero. It is a measure of how long a given thrust profile will take to reach the target orbit. An optimal thrust profile will be the one that minimizes Q at each step. The rate of change of Q is given by equation (3-85).

$$\frac{dQ}{dt} = \sum_{oe} \frac{\partial Q}{\partial oe} \dot{oe} \quad (3-85)$$

Finally, the variation of the orbital elements is given by Gaussian orbital equations.

$$\frac{da}{dt} = \frac{2a^2}{h} \left(e \sin \theta T_r + \frac{p}{r} T_\theta \right) \quad (3-86)$$

$$\frac{de}{dt} = \frac{1}{h} \{ p \sin \theta T_r + [(p+r) \cos \theta + r_e] T_\theta \} \quad (3-87)$$

$$\frac{di}{dt} = \frac{r \cos \theta + \omega}{h} T_h \quad (3-88)$$

The parameters T_r , T_θ , and T_h are the thrust forces along the radial, tangential, and angular momentum directions. They are represented as follows:

$$T_r = T \cos \beta \sin \alpha \quad (3-89)$$

$$T_\theta = T \cos \beta \cos \alpha \quad (3-90)$$

$$T_h = T \sin \alpha \quad (3-91)$$

Once all the elements are defined, we could obtain the thrust angles α and β at each step that minimizes the \dot{Q} in equation (3-85). This minimisation problem needs to be solved at every integration step. This requires substantial amount of computational resources. Thus, to avoid excessive memory storage and computational time, an analytical expression for \dot{Q} is obtained as a function of α and β using MATLAB's symbolic toolbox. The minimisation problem is solved using MATLAB's `fminsearch` which uses Nelder-Mead simplex direct search method to find the minimum of unconstrained multi-variable functions.

From the initial orbit, defined in Table 3-10, the chemical propulsion burn is performed to provide a $\Delta V = 45$ m/s to stabilize the orbit and the target of the circularization is a near circular orbit with $r = 63,390$ km and $e = 0.05$. Figure 3-22 illustrates the circularization to the desired orbit. The Q-law circularization is compared after time-optimal and fuel-optimal transfers, which have different initial masses.

An overall comparison of parameters of heliocentric transfer, ballistic capture, and circularization is shown in Table 3-11.

Comparing the two solutions, time-optimal heliocentric transfer and subsequent circularization is selected for electric propulsion system design.

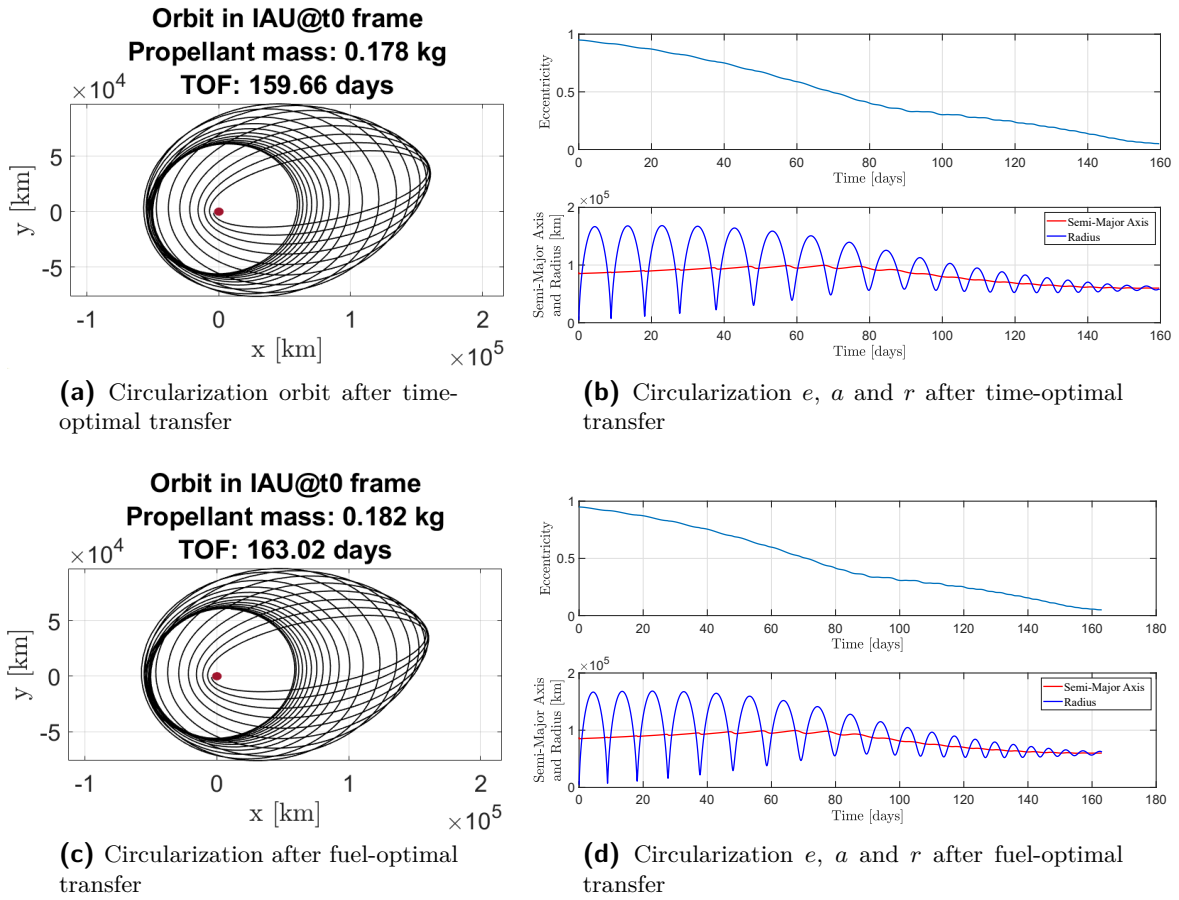


Figure 3-22: Circularization orbits after time-optimal and fuel-optimal heliocentric transfers

Table 3-11: Circularization parameters after time-optimal and fuel-optimal heliocentric transfers

	Circularization after time-opt transfer	Circularization after fuel-opt transfer
Initial spacecraft mass, m_0	22.555 kg	22.955 kg
Chemical prop. burntime ($\Delta V = 45$ m/s)	335 s	341 s
Electric prop. circularization time	159.66 days	163.02 days
Electric prop. m_p	0.178 kg	0.182 kg
Overall transfer time	1359.66 days	1513.02 days
Overall electric prop. m_p	5.07 kg	4.674 kg

3-8 Systems design and sizing

The time-optimal heliocentric transfer and circularization require an overall propellant mass of 5.07 kg. A $\sim 11\%$ margin is applied on this mass for contingency and an extra 5% is applied for station-keeping costs at Mars, which brings it to 5.87 kg. Iodine solid state density is 4940 kg/m^3 and corresponding propellant volume is $\sim 1190 \text{ cm}^3$.

The electric propulsion feed system consists of a propellant reservoir where Iodine is stored and sublimated to gas phase (I_2) using a low-power heat source. The resulting vapour is delivered to the thrust chamber using a latch valve and a proportional flow control valve (mass flow control unit) [158]. The vapour pressure of Iodine is 0.3 Torr at 25°C. The flow line must be heated to keep the Iodine in the vapour state, although it requires <1W power to maintain a 10 mg/s flow of I_2 [159]. Owing to the low storage pressure, the reservoir tank is thin walled and made of a thermoplastic material [142].

The propellant tank is sized to contain solid Iodine and the low-power heat source. The latter occupies 5% of the volume. Additionally, a 5% ullage volume is allocated for the sublimated gas. A tank volume of 1308 cm³ is utilised and the dimensions are 20 cm × 10 cm × 6.54 cm, which is ~1.3U. The tank mass amounts to 0.02 kg. Inclusion of the feed lines, valves, and PPCU volumes brings the total volume to 3U. The electric propulsion system schematic is illustrated in Figure 3-23. The overall design parameters of the electrical propulsion system are summarized in Table 3-12.

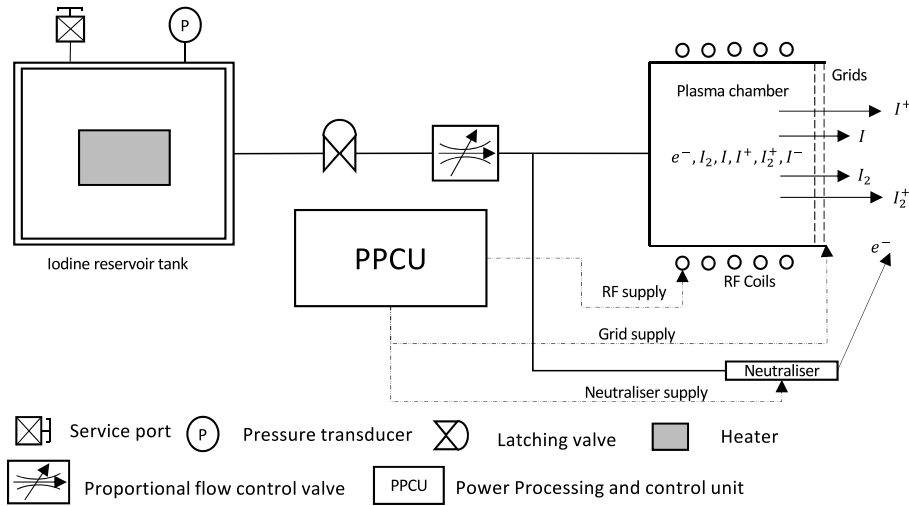


Figure 3-23: Schematic of the electric propulsion system

Table 3-12: Electric propulsion design parameters

Parameter	Value	Parameter	Value
Propellant mass, $m_{p,mg}$	5.87 kg	Feed sys. mass, m_{feed}	0.5 kg
PPCU Mass, m_{PPCU}	0.2 kg	Thruster mass, m_T	0.2 kg
Tank volume	1308 cm ³	Tank dimension	20 × 10 × 6.54 cm ³
EP total mass, $m_{ep,sys}$	6.57 kg	EP total volume, $V_{ep,sys}$	3U

Chapter 4

MARIO Systems Design

The design of the *propulsion* system of MARIO has been presented in chapters 2 and 3. This chapter highlights the *overall systems* design of MARIO with some details on the rest of the subsystems. The content presented in this chapter is partially based on the work published in Mani et al *Systems Design of MARIO: Stand-alone 16U CubeSat from Earth to Mars* [160]. The system design pursued here is in its preliminary phase and higher maturity is envisioned during further development. The detailed systems design is out of scope of this work since the objective is not the development of a full mission but the design of combined chemical–electric propulsion. However, the preliminary systems design that has been presented here provides an overview of the mission and the context of the research work pursued. The mission at a glance is illustrated in Figure 4-1.

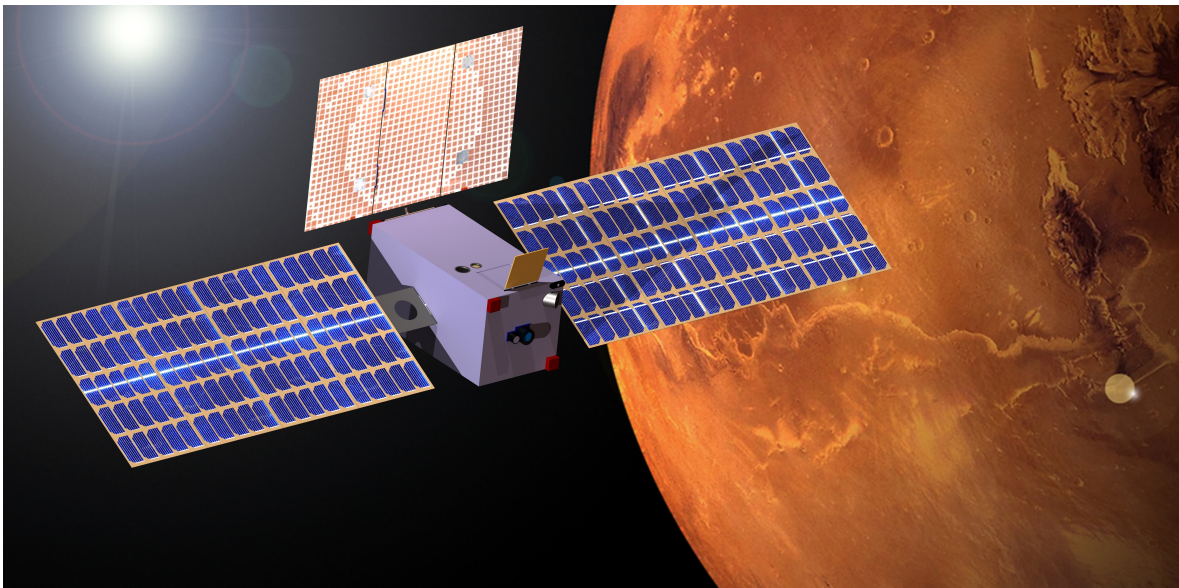


Figure 4-1: MARIO mission at Mars

The MARIO mission seeks to characterise the thermal environment of the Mars upper atmosphere using a payload that detects radiation in the visual and near-infrared ranges. The scientific mission of MARIO is fairly straightforward and open for further iteration. The primary challenge of MARIO is the technological demonstration of activities that have never before been achieved by CubeSats: escaping Earth, autonomous heliocentric transfer, achieving ballistic capture, and circularizing onto an operational orbit at Mars. The science objectives are achieved in conjunction with these. In the overall context, MARIO performs significant science at very low costs.

The major engineering objectives of MARIO are:

1. Demonstrate the feasibility of a stand-alone CubeSat to escape Earth, perform autonomous heliocentric transfer, achieve ballistic capture, and enter an operational orbit at Mars.
2. Demonstrate the feasibility of a CubeSat to establish communication with Earth from Mars operational orbit and transmit scientific data during science operations.
3. Demonstrate the usage of combined chemical–electric propulsion to achieve a stand-alone high-thrust–low-thrust Earth to Mars transfer.
4. Demonstrate the ability of a stand-alone CubeSat to withstand and operate effectively under high radiation conditions near Earth and in the interplanetary space.

4-1 Systems architecture

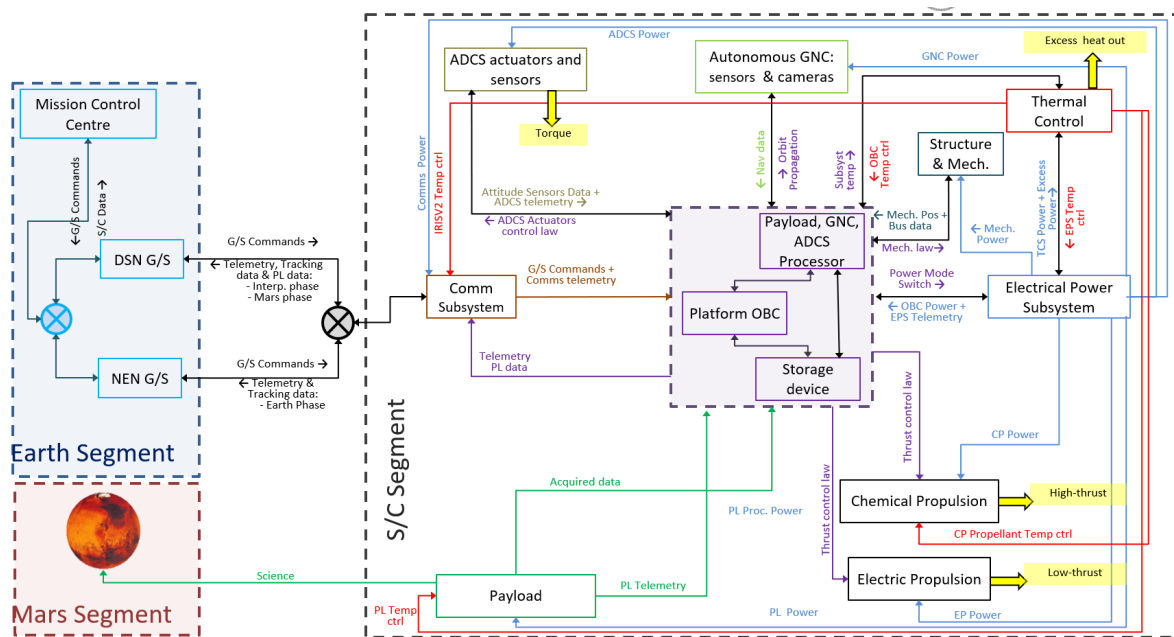


Figure 4-2: MARIO system physical and functional architecture

MARIO system physical and functional architecture is illustrated in Figure. 4-2. The systems present are the thermal imaging camera payload (P/L-CAM), chemical and electric propulsion (CP & EP), reflectarray communications system with high-gain and low-gain antennas (COMT-HGA & COMT-LGA), attitude determination and control systems (ADCS), a flexible electrical power system (EPS), a semi-active thermal control system (TCS), navigation camera (GNC CAM), a platform on-board computer (OBC), and a high speed processor for processing of payload data, ADCS data, and navigation data as well as on-board propagation of orbits for guidance.

4-2 Flight system design

4-2-1 Combined propulsion

The combined chemical–electric propulsion system design has been presented in chapters 2 and 3. The combined characteristics of the propulsion system are presented in Table 4-1.

Table 4-1: Combined propulsion characteristics

Parameter	Chemical	Electric
Flight Time [days]	33.03 ^a	1359.66
Prop. Mass [kg]	5.725	5.87
System Mass (wet) [kg]	6.91	6.57
Size [U]	8	3
ΔV (real) [km/s]	408	6.9
Peak Power [W]	14	70
Overall propulsion mass [kg]	13.38	
Overall propulsion volume [U]	11	

^a This flight time is counted as the Earth orbiting time until eccentricity $e = 1$, and not the time to reach the Earth sphere of influence. An additional ~ 30 days coasting period could be considered for reaching the Earth sphere of influence.

4-2-2 Power

Steady power generation is ensured using two solar arrays connected to SADA mechanisms for continuous Sun pointing. Table 4-2 contains Electrical Power System (EPS) requirements. The solar array sizing is determined by the the power required by the electric propulsion during the heliocentric transfer as well as the power demand while communicating from Mars orbit. Table 4-3 details the power consumption of individual subsystems and Table 4-4 shows the power consumption during different operational modes of the mission. MARIO systems consume 101 W (111 W with 10% margin) while it is in ‘full’ low-thrust manoeuvre (LTM) mode. This mode is active in the interplanetary phase. However, the power generation varies with the Sun-spacecraft distance by the inverse square law. A trade-off is performed to size the solar arrays considering: a) the need of sufficient power for EP to execute the interplanetary transfer and the circularization manoeuvre at Mars, and b) the power consumed by the payload and the rest of subsystems when EP is not in use, i.e, science operational mode

(see 4-4). SCM mode is significantly less demanding than the LTM mode. The system will be infeasible in terms of system mass and volume if the solar arrays are sized for the LTM mode at Mars and there would be a significant waste in power during SCM. The result of the trade-off is that the power system shall deliver 80 W to spacecraft units at Mars distance.

Table 4-2: Power system requirements

ID	Requirement
EPS-01	The system shall have Sun pointing capabilities.
EPS-02	The system shall provide at least 80 W to MARIO subsystems at 1.5 AU distance from the Sun after heliocentric transfer.
EPS-03	The battery shall provide at least 31 W for spacecraft survival for an eclipse duration of 3 hours on Earth orbit.
EPS-04	The EPS shall be able to dissipate the excess power generated to avoid spacecraft overheating

Table 4-3: MARIO subsystems power consumption

Subsystem	Nominal Power [W]	Remarks
P/L-CAM	7,0	
P/L-PROC	10,0	Also used in AOCS
EPS	1,0	Supply and distribution
COMT HGA	41,2	Transmit and Receive 10 W feeding
COMT LGA	33,2	Transmit and Receive 2 W feeding
COMR	12,6	Only Receive
OBC	0,8	Main Computer and Data Handler
AOCS	16,1	RW, STR, Sun sensor, IMU, PLCPROC/2
EPROP	70,0	Could be reduced affecting performance
CPROP	14,0	
TCS	10,0	Could be adapted
MECH	2,0	Deployment and Solar Array orientation
GNC CAM	0,7	

Figure 4-6 depicts MARIO solar arrays. Each one consists of 4 panels (22×45 cm) with 25 solar cells. The selected solar cells are the Azurspace 3G30C 30% efficiency cells. This means a total cell area of 0.6 m^2 . Assuming a 10% inherent degradation and a 0.9% yearly degradation, the power generation capability will be 220 W BOL at Earth distance and 95 W EOL at Mars distance after 6 years. Taking into account an average 92% power distribution efficiency and 5 deg cosine losses, the power available to the subsystems will be 202 W at 1 AU at BOL and 85.75W at 1.5AU at EOL.

The estimated maximum eclipse duration in Earth phase is 3 hours while the eclipse in a 60,000km Mars circular orbit lasts 1.1 hours. Hence, the Earth phase is the most restrictive case from the battery point of view. The power required by the system in eclipse mode is 31 W including a 10% margin. Considering 95% battery efficiency and a Depth of Discharge (DoD) of 65%, the energy required from the battery is 150 Wh. Two GOMspace Nanopower BPX 77Wh batteries will be used as secondary power source to cover those eclipse phases and

Table 4-4: MARIO power operational modes

Mode	Acronym	Peak Power [W] w/ 10% margin	Active systems
Commissioning	CMS	70	EPS, OBC, AOCS, COMT-LGA, MECH
Chem Man. Mode	HTM	49	EPS, OBC, AOCS, CPROP, MECH
Cruise Mode	CRU	34	EPS, OBC, AOCS, MECH, GNC-CAM, TCS
Near Earth Comm Mode	NEC	70	EPS, OBC, AOCS, COMT-LGA, MECH, TCS
Elec Manoeuvre Mode	LTM	111	EPS, OBC, AOCS, EPROP, MECH, GNC-CAM, TCS
Deep-space Comm Mode	DSC	79	EPS, OBC, AOCS, COMT-HGA, MECH, GNC-CAM, TCS
Science Mode	SCM	46	EPS, OBC, AOCS, PL-CAM, PL-PROC, MECH, TCS
Safe Mode	SFM	45	EPS, OBC, AOCS, COMR, TCS
OptNav Mode	NAV	37	EPS, OBC, AOCS, PL-CAM (Nav-mode), MECH, TCS
Eclipse Mode	ECL	31	EPS, OBC, AOCS, TCS

peaks demand (see Figure 4-5). Besides, the GOMspace Nanopower P60 serves as PMAD (Power Management And Distribution) unit and equips two PDU (Power Distribution Unit) and two ACU (Array Conditioning Unit). This PMAD units will enable a flexible electrical power system architecture to enhance power management. On the one hand, each ACU is connected with several lines to a solar array. On the other hand, the PDUs distribute the power among the different subsystems using suitable lines. Figure 4-3 represents a schema of the electrical interfaces of MARIO CubeSat.

4-2-3 Communications

Table 4-5 lists communications subsystem requirements. Establishing a direct communication link from MARIO to Earth at more than 1 AU distance is one of the most important challenges of this mission. CubeSats cannot equip conventional parabolic reflectors as larger interplanetary spacecraft do and the power available is much more limited. These facts compels us to pursue an innovative solution for interplanetary CubeSat communications. The deep-space communications strategy for MARIO is based on a deployable reflectarray high gain antenna (HGA) combined with IRIS transponder. MarCO mission used this technology serving as a data relay for Insight lander [161] successfully. Furthermore, in 2018, ISARA mission transmitted to Earth with a reflectarray from LEO and M-ARGO ESA CubeSat is designed to employ this antenna for interplanetary communications [23, 162]. MARIO communications subsystem is completed with a low gain patch antenna (S-Band) that will

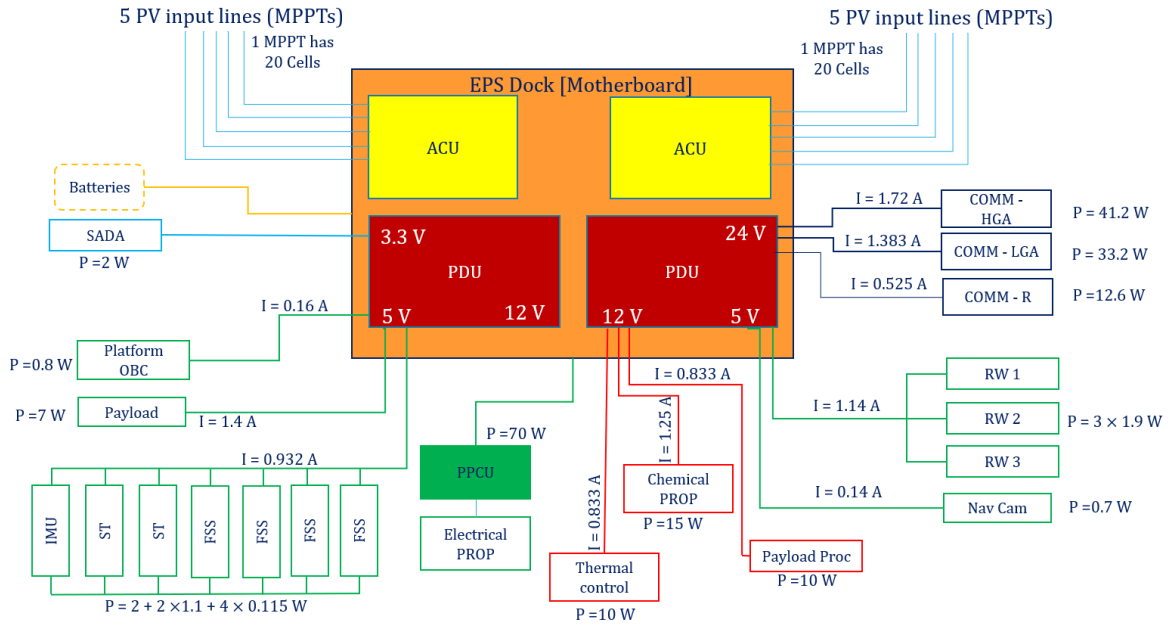


Figure 4-3: MARIO electrical interface

be utilized to establish first contact with the Earth after launch and during the Earth orbit raising manoeuvre.

Table 4-5: Communications system requirements

ID	Requirement
COM-01	The system shall provide direct link to Earth to transmit telemetry.
COM-02	The system shall communicate with G/S using X-Band in Mars phase and in interplanetary phase.
COM-03	The system shall communicate with G/S using S-Band in Earth orbit.
COM-04	The system shall be able to transmit 2 kbps data rate from 1.5AU by means of a direct link to the Earth.
COM-05	The system shall BER shall be below 10^{-6} .
COM-06	The stack size of the HGA shall be below 45x23x4 cm.

The deployable reflectarray is designed to fit on the 16U CubeSat configuration so it consists of three 20x44 cm panels. During the launch phase, the three panels are folded down forming a one single panel configuration. Later, the stack panel is deployed and then unfolded. Finally, the reflectarray feeder is also deployed, ending in a configuration that can be observed in Figure 4-6.

The HGA antenna will operate in the X-Band frequency (8.4GHz) and will transmit data to the DSN. The estimated maximum gain for this antenna is about 29.95 dB taking into account a 42% efficiency. The power provided to the feeder is set to 10 W but it could be increased if there is enough power available to improve transmission performance. On the other side of the link, a 70 m DSN antenna will receive the data from MARIO.

The path losses are the main source of losses because of the huge distance that waves have to travel. From 1.5AU and with the selected frequency, the free space losses are 278 dB. On top of that, 1 dB loss is added to account for rain and atmospheric gases attenuation. Besides, the system noise temperature, which is the other main contributor to the attenuation of the signal is estimated at 140 K. Finally, average values for antenna pointing, polarization and modulation losses are taken. The required BER is set at 10^{-6} and the selected modulation is BPSK. The corresponding required energy per bit noise ratio is 5 dB [62]. Under the described conditions, MARIO is able to transmit more than the required 2.0 kbps from 1.5AU distance (2.4 kbps). Table 4-6 summarises the main parameters involved in the link computation and the achieved performances.

Table 4-6: HGA link budget from 1.5AU

DOWNLINK BUDGET		
Assumptions		
DSN 70 m station	-	-
Madrid Avg. Rain	-	-
1 AU = 1,5·10E8 km	-	-
Distance	1,50	AU
Data Rate	2000	bps
Frequency		
Frequency	8420	MHz
Tx Antenna		
Feed power	10	W
Gain	30,0	dBi
Pointing Loss (1° pointing error)	-1,9	dB
Rx Antenna		
Gain	74,8	dBi
Pointing Loss	-0,1	dB
Losses		
Polarization Loss	-0,2	dB
Total Path Loss	-279,0	dB
System Noise Temperature	140,0	K
Transmitter Feeder Loss	-1,0	dB
Performance Parameters		
Equivalent Isotropic Radiated Power (EIRP)	39,0	dBm
Gain to Noise Temperature Ratio (G/T)	53,4	dB/K
Carrier to Noise Spectral Density Ratio (C/N0)	39,3	dBHz
Energy per Bit to Noise Ratio (Eb/N0)	5,81	dB
Modulation	BPSK + R-1/2 Vitervi	
(Eb/N0)req	5,0	dB
Recovery Margin	0,80	dB

Since the distance from Earth to MARIO will vary along the mission, the maximum data rate that can be transmitted will also vary. Figure 4-4 illustrates the maximum data rate that could be transmitted as a function of MARIO–Earth distance and feeder input power taking into account the above-mentioned considerations for the link budget. The maximum data rate decreases significantly from 0.5 AU to 1.5 AU. Therefore, during Earth-Mars conjunction (0.5 AU distance), MARIO will be able to transmit about 25 kbps for 10 W feeder power.

Nevertheless, the distance from the Earth to Mars increases up to 2.5 AU (planets opposition) which reduces dramatically the maximum data rate. In such case, MARIO can use its low gain antenna to transmit information to a larger Mars orbiter spacecraft which then would relay it to the Earth.

IRIS v2 transponder currently works with X-band and UHF bands. It is planned to extend its capabilities to other frequency bands like the S-Band. The transponder weights 1.2 kg and its nominal power consumption for X-band transmit/receive is 35 W for 3.8 W feeder power. Finally, ISM S-Band antenna manufactured by Endurosat is selected as the low gain patch antenna because of its low mass and performance.

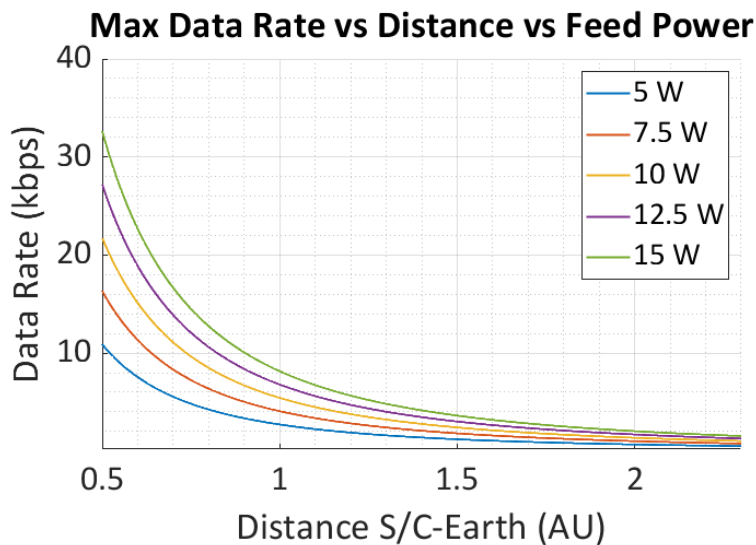


Figure 4-4: Maximum data rate transmission as a function of distance and feed input power

4-2-4 Other subsystems

Semi-active thermal control system is designed to preserve the payload, propellants, and other subsystems within their operational temperature limits at near-Earth and interplanetary environments. This task will be performed by means of heaters, MLI and different surface finishes. To cool down the payload, the possibility of adding a dedicated radiator is considered.

Attitude determination and control will be carried out by the combination of several COTS. Two ST400 star trackers are installed in MARIO. They only consume 0.7 W in nominal operation and they have competitive attitude determination accuracy: 10 arcseconds in pitch and yaw and 120 arcseconds in roll (3σ). To compensate the lower of accuracy in roll axis, the two STR are oriented along different axis. Both of them are equipped with baffles to reduce straylight and protect them against thrusters' plume impingement. The update rate of ST400 STR is 5Hz, which is compatible with IMU performance. In addition, four fine Sun sensors (nanoSSOC-D60) pointing towards different directions serve as a backup for attitude determination. These Sun sensors have a 60 deg FOV and an accuracy of 0.5 deg. Finally, STIM300 IMU measures angular acceleration and velocity with 2000 SPS and with a 0.3 deg/h gyro bias instability. In the actuators side, 3 RW400 reaction wheels are responsible for the

attitude control. Owing to their 50 mNms momentum storage capacity and their relatively low power consumption (1.9 W), RW400 are suitable for MARIO. Finally, four small 0.1 kg cold gas thrusters for reaction wheels desaturation and course correction complete the ADCS.

Skylab NanoOBC is the main On-Board computer. It is a light (about 60g) and robust device against SEE. The main OBC is in charge of general housekeeping and command transmission in MARIO. On the contrary, the dedicated and more powerful payload processor deals with science data processing, attitude determination and orbit control and is also responsible for processing navigation information. The selected COTS is the Unibap e20xx. Despite its high power consumption, the performance is quite high.

The payload system consists of a customized VIS and IR camera and the above-mentioned payload processor. The maximum available weight for the payload camera to comply with spacecraft total mass requirements is about 1.8 kg and the maximum power consumption shall be below 7 W. The PL camera shall occupy less than 1.2U inside the CubeSat. The overall system characteristics are listed in Table 4-7.

4-3 Structure and system configuration

MARIO is a 16U CubeSat whose primary structure consists of 4 ‘decks’ of 4U each. A 16U COTS structure does not exist at the moment (12U is the maximum) but several manufacturers could provide customized structures. The structure has to allow visibility access to the cameras and sensors as well as room for internal harnesses and feed system pipings of the thrusters. In addition to the structure, the different sides or panels have to be covered by an aluminum shielding layer (2.5mm thickness) to protect the spacecraft against radiation. The total mass of aluminum thickness is 2 kg and has been scaled from the result of LUMIO mission [67]. Hereinafter, the sides of the CubeSat are referred to as the PL panel (where is the PL camera), the Anti-PL panel (the opposite side), the bottom panel, the top panel, the right panel and the left panel.

The main drivers for the configuration are: a) accommodation of 2 different types of propulsion, b) power generation strategy, c) having an unobstructed side for the PL camera, and d) communications with reflectarray.

The CP and the EP modules are placed on opposite sides of the CubeSat. The primary reason is that there is not enough space to hold both on one side. Besides, the center of mass with them placed on opposite sides is kept closer to the geometrical center of the spacecraft. Hence, the CP module is placed close to the bottom panel, with the 2 CP thrusters outside the structure, while the EP module is placed close to the top panel, with the ion engines outside (see Figure 4-5 and Figure 4-7). On the one hand, the four CP propellant tanks are located just above the bottom panel. The tanks themselves occupy about 1.8U. The pressuriser tank position takes advantage of the shape of the CP propellant tanks and is installed in the central axis of the CubeSat. Therefore, above each CP propellant tank up to the upper half of the CubeSat there is 0.2U available space for piping. On the other hand, the iodine tank is placed centered on the top part of the structure. The PPCU is located close to it facing the PL panel.

The Solar Drive Actuators mechanisms (SADA) divide the CubeSat in two halves. The rotation axis of SADA is orthogonal to the right and left panels. The majority of the components

Table 4-7: Overall system characteristics

Subsystems and Payload summary	
Propulsion	Chemical Propulsion: - 2 1,5N range thrusters - FLP-106 Propellant - High thrust maneuvers - Gaseous Nitrogean pressurant
	Electric Propulsion: - Gridded Ion Thruster - Iodine solid propellant - Low thrust trajectory and ballistic capture
Power	- 2 Deployable solar arrays with SADA - 30% Eff. Azurspace 3G30C solar cells - 2 GOMSpace BPX 77W/h batteries - PMAD: GOMSpace P60
Communications	- IRIS V2 Transponder - Reflectarray HGA X-Band - LGA S-Band
ADCS	- 3 RW: RW400 50mNms Hyperion Tech. - IMU STIM300 - 2 STR: ST400 Hyperion Tech. - 4 Sun Sensors: nanoSSOC-D60 Solar MEMS - 4 ADCS Cold gas thrusters
Data Handling	- Main OBC: NanoOBC Skylab
Structure	- 16U COTS modification - Aluminum shielding
Thermal Control	- 10W heaters power - MLI and coatings
Navigation	- NAV Camera: IM200 Hyperion Tech.
Payload	Payload Camera: - Customized VIS and IR Camera - 7W consumption and 1,8kg
	Payload Processor: - UNIBAP's e20xx/e21xx - Performs AOCS tasks too

of MARIO are located on the third deck of the structure. The PL is placed along the PL panel for Mars centre pointing and the PL processor is below it. The 3 RW are oriented in 3 different axis and the IMU and 1 Sun sensor are just above one of them. The Iris transponder

and the OBC are stacked behind the PL so they are hidden in Figure 4-5. Finally, one STR, a navigation camera and the PMAD can be found in the remaining 1U space.

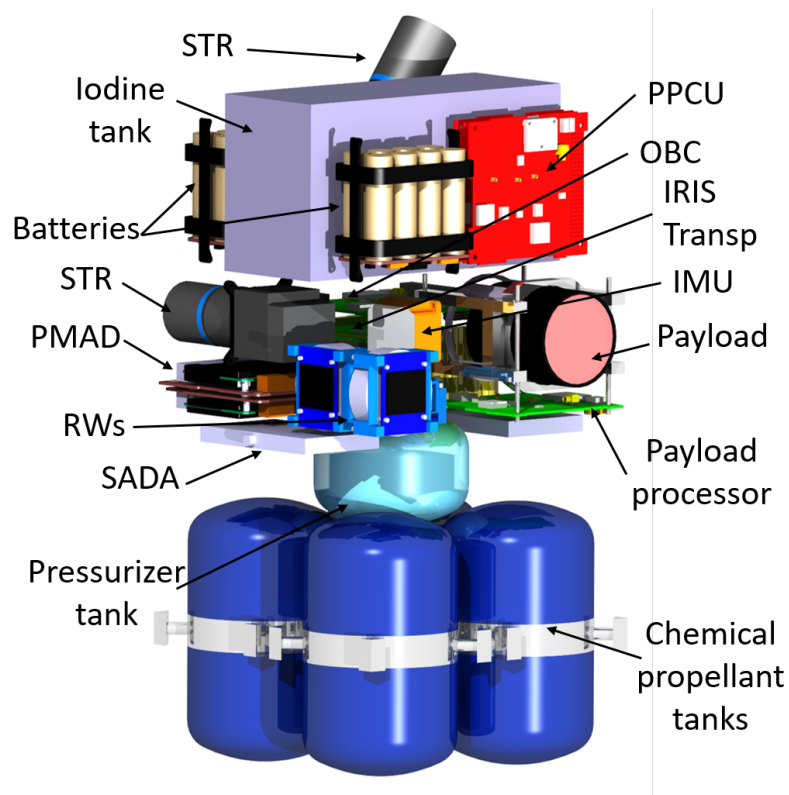


Figure 4-5: MARIO internal configuration

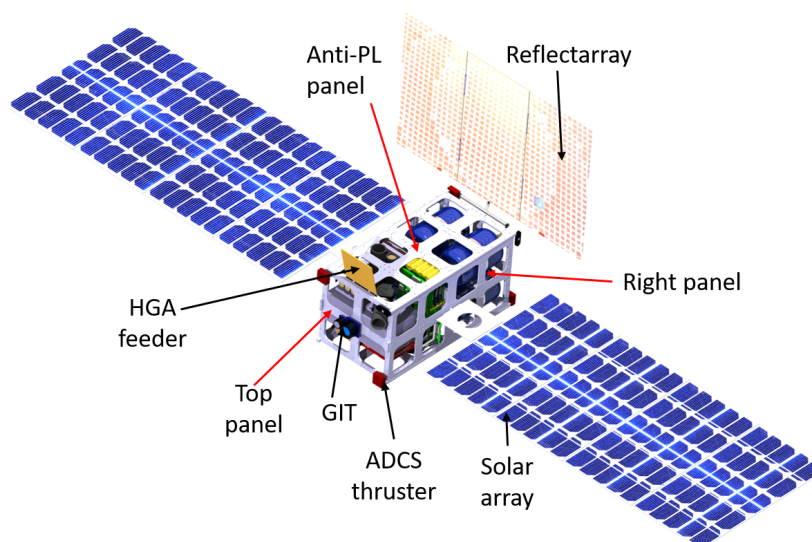


Figure 4-6: MARIO external configuration w/o shielding

On the upper deck, apart from the EP module, batteries are symmetrically located with respect to the EP tank. In addition, another STR is placed tilted with respect to the orthogonal

direction of the top panel. They are tilted because, primarily from the performance point of view, it is worse to have the STR along the same axis. That is the reason why the PL panel was discarded as a location. Besides, if the STR is oriented towards the right panel, it would be obstructed by the solar array eliminating that direction as an option. The direction orthogonal to the top panel would be suitable from performance point of view but not for potential plume impingement, which is the second driver. To reduce the plume impingement, the STR is tilted and a baffle is used to protect it.

In the outer part of the spacecraft, the rest of Sun sensors (one on the top panel and two on the bottom panel) are installed. Besides, the 4 ADCS thrusters are placed symmetrically in the top and bottom panels. Reflectarray and its deployment mechanism are located on the outer side of the Anti-PL panel. Therefore, the feeder is also located in that panel. Finally, each solar array is attached to their corresponding SADA mechanism on the left and right panels. In stack configuration, both solar panels and reflectarray will be folded. The same applies to the feeder of the HGA antenna. Therefore, the outer envelope of the whole CubeSat will be 25x25x50cm.

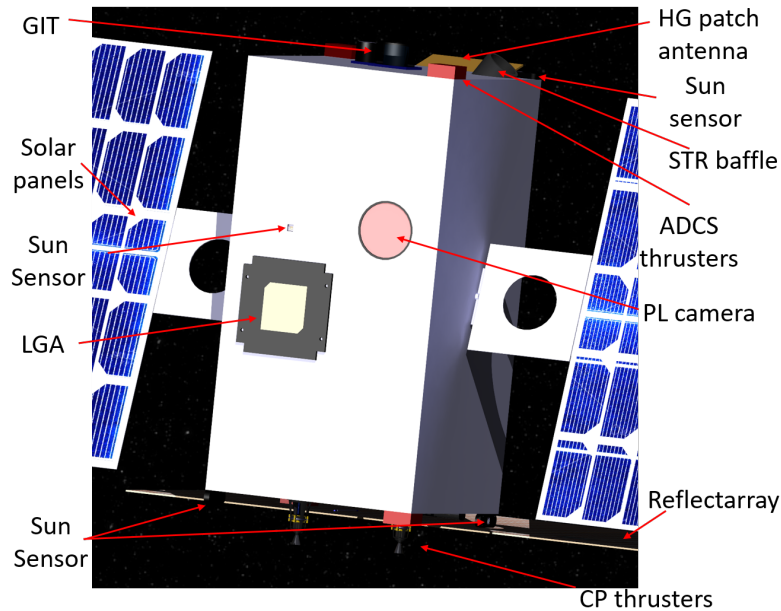


Figure 4-7: MARIO external configuration Detail

Currently, ISIS has a commercial 16U deployer that is yet to be flight tested. However, owing to the overall size, dimensions, and configuration of the MARIO CubeSat, the existing 16U CubeSat deployer, such as the one of ISIS, would need to be customized to accommodate primarily the thrusters and the solar panels.

4-3-1 Mass Budget

Table 4-8 shows the mass budget of MARIO CubeSat grouping components by subsystems. Figure 4-8 is a pie chart that represents the distribution of dry mass among subsystems. The table includes the subsystem level margin that depends on the design maturity of each

subsystem/component (5, 10 or 20%) and the dry mass system margin which is set to 5%. On top of that, chemical propellant, pressuriser and iodine masses are added, obtaining the total wet mass. Propellant and pressuriser masses already include a margin through the ΔV .

Table 4-8: Mass Budget of MARIO including unit and system margins

Item	Mass [kg]	Margin	Mass w/ margin [kg]	Design approach
Structure	4,326	5%	4,542	COTS with modification
EPS	3,964	5%	4,180	COTS with modification
Communications	1,982	5%	2,081	COTS with modification
ADCS	1,971	5%	2,070	COTS
ADCS Thrusters	0,400	10%	0,440	COTS with modification
Navigation CAM	0,060	5%	0,063	COTS
Chemical Propulsion	1,06		1,223	
Propellant Tank	0,219	10%	0,241	Customized design
Thruster	0,400	20%	0,480	COTS
Feeding system	0,200	20%	0,240	Customized design
Press Tank	0,238	10%	0,262	Customized design
Electric Propulsion	0,70		0,810	
Propellant Tank	0,100	10%	0,110	Customized design
Thruster	0,200	20%	0,240	COTS
PPCU	0,200	10%	0,220	COTS with modification
Feeding system	0,200	20%	0,240	Customized design
Mechanisms	0,650	10%	0,715	COTS
OBC	0,058	5%	0,061	COTS
Harness	0,200	20%	0,240	COTS with modification
TCS	0,300	20%	0,360	COTS with modification
PL Camera	1,840	20%	2,208	Customized design
PL Processor	0,300	5%	0,315	COTS
Total Dry Mass	17,808		19,31	
System margin		5%		
Dry mass w/ marg.			20,27	
Chemical Propellant			5,72	Margin in Delta V
Pressurizer			0,13	Margin in Delta V
Iodine			5,87	Margin in Delta V
Total Wet Mass			32,00	

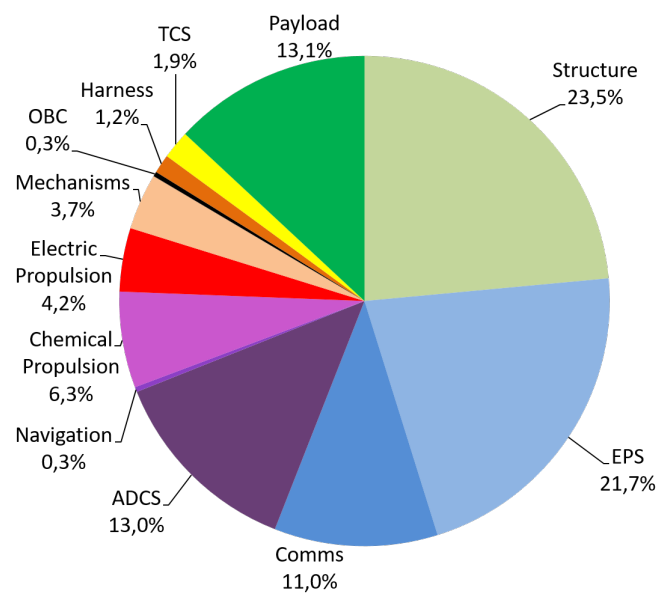


Figure 4-8: Relative contribution of different subsystems to MARIO CubeSat dry mass

Concurrent propulsion–trajectory optimisation

Traditionally, low-thrust trajectory optimisation is done by establishing an optimisation framework in which the thrust T is utilised as a control variable. The specific impulse I_{sp} is also utilised in the optimisation as it influences the variation of spacecraft mass. However, these performance variables are considered with a set of defined thruster operational characteristics. No insight is usually provided into how the thruster is actually controlled. Indeed, only recently have there been analyses which consider the variations of T and I_{sp} with the thruster input power [163]. However, the rest of the parameters that influence the thruster performance are discarded.

A new paradigm is required for a more comprehensive mission design. In this approach, the crucial parameters that influence the thruster performance are incorporated into the optimisation framework such that the thruster operation and the low-thrust trajectory are concurrently optimised. The thruster physics are directly taken into account through the inclusion of the control parameters. This allows for a higher level of control capability and autonomy since by knowing the parameters that are real-time controllable and those that influence the thruster performance, we can incorporate them into the control law algorithms uploaded on the on-board processor.

5-1 Thruster performance envelope

The radiofrequency ion thruster performance and design parameters applicable to MARIO mission are calculated in section 2-5. The iodine plasma thruster model is implemented to calculate the thrust T , specific impulse I_{sp} and efficiencies η_m , η_p and η_{tot} as functions of the total power P_{tot} . The mass flow rate \dot{m}_0 is fixed at 48 $\mu\text{g/s}$ and the grid voltage V_{grid} is fixed at 2000 V. The low-thrust trajectory optimisation is performed and the heliocentric transfer trajectory is calculated using this thruster performance.

The P_{tot} , which drives the performance, is ensured to be always equivalent to the thruster input power P_{in} , i.e., the thruster utilises all the power available to it to generate the thrust and specific impulse. The distance between the Sun and the spacecraft r determines the power available to the overall system, and therefore P_{in} , based on the inverse square law, i.e., $P \propto 1/r^2$. The relationship between r and P_{in} is illustrated in Figure 3-14.

Revisiting equation 3-49, we have

$$P_{tot} = P_{beam,i} + P_g + P_{cath} + P_{RF} \quad (5-1)$$

The Power Processing and Control Unit (PPCU) supplies the RF coils with P_{RF} which directly influences the production of ions in the plasma chamber, i.e., the ion beam current $I_{beam,i}$, and subsequently the thrust T and I_{sp} (see equations (3-42) and (3-43)). The DC grids are maintained at V_{grid} , which when multiplied with $I_{beam,i}$ yields $P_{beam,i}$. Thus, both P_{RF} and V_{grid} influence $P_{beam,i}$ and consequently P_{tot} . The grid voltage V_{grid} also determines the ion beam velocity $v_{beam,i}$, which then contributes to T . Additionally, the mass flow rate \dot{m}_0 determines the particle densities and subsequently the ion flux Γ_i , which contributes to the $I_{beam,i}$ and hence $P_{beam,i}$. The \dot{m}_0 also contributes to the neutral gas thrust power P_g through neutral gas flux Γ_g . Thus, V_{grid} , \dot{m}_0 and P_{RF} influence T and I_{sp} . This is illustrated in Figure 5-1.

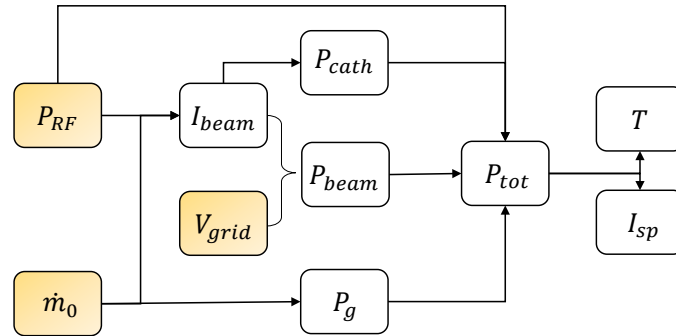


Figure 5-1: Relationship between parameters P_{RF} , V_{grid} , \dot{m}_0 and total power P_{tot} as well as performance T and I_{sp}

These three parameters, V_{grid} , \dot{m} , and P_{RF} are real-time adjustable independently, and can be used as the main control parameters that influence the performance of the thruster. Thus, to broaden the scope of the analysis, the thruster performance is analysed over a range of V_{grid} , \dot{m}_0 , and P_{RF} to create a thruster performance envelope. Figure 5-2 represents T , I_{sp} , and P_{tot} as functions of the control parameters. P_{RF} is varied from 5 to 40 W, \dot{m}_0 from 45 $\mu\text{g/s}$ to 60 $\mu\text{g/s}$ and V_{grid} from 1900 to 2100 V. The thruster performance model presented in section 3-6 is utilised to create the envelope.

Over these ranges of control parameters, the maximum T 2.0253 mN the minimum T is 0.3154 mN, maximum I_{sp} is 3441.7 s and the minimum I_{sp} is 714.56 s, and the maximum P_{tot} is 86.8 W and the minimum P_{tot} is 11.3 W. The trends of T , I_{sp} and P_{tot} are such that they increase with the increase in V_{grid} , \dot{m}_0 , and P_{RF} . A single ‘slice’ of Figure 5-2, the T and I_{sp} variation with \dot{m}_0 and P_{RF} for $V_{grid} = 2000$ V is shown in Figure 5-3.

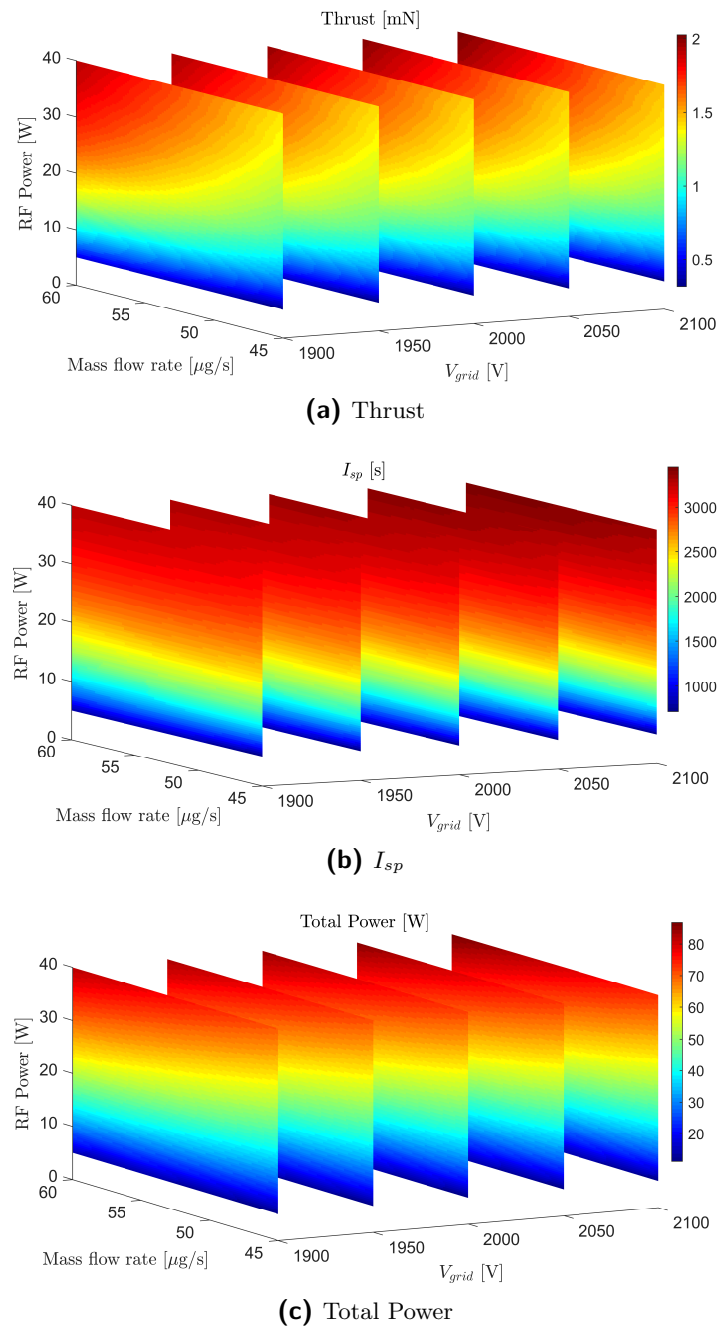


Figure 5-2: Thrust, I_{sp} and total power variations with grid voltage V_{grid} , mass flow rate \dot{m} , and RF power P_{RF}

The T and I_{sp} performance envelope measured as a function of total power P_{tot} at $V_{grid} = 2000$ V is illustrated in Figure 5-4. It can be inferred that for the same P_{tot} (same contour level), multiple values of T and I_{sp} can be obtained depending upon the values of the control parameters.

Thus, by varying the control parameters real time, we can adjust the performance values and therefore provide the spacecraft with a higher control capability. Since the T and I_{sp}

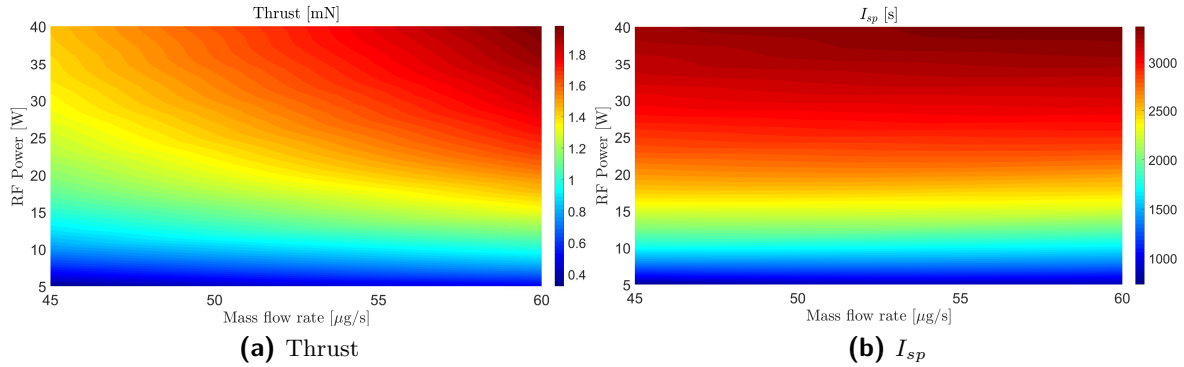


Figure 5-3: Thrust and I_{sp} variation with mass flow rate \dot{m}_0 and RF power P_{RF} for a single grid voltage $V_{grid} = 2000$ V.

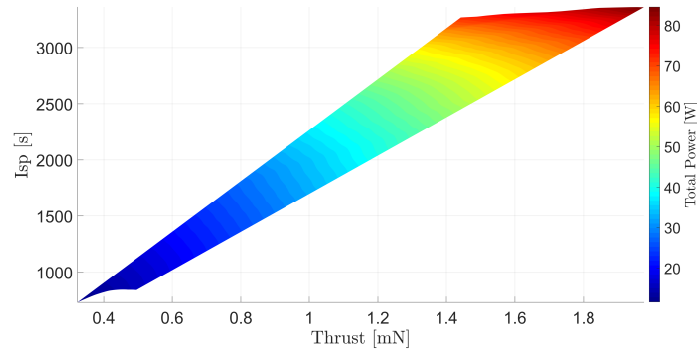


Figure 5-4: Thrust and I_{sp} vs P_{tot} for $V_{grid} = 2000$ V

performance directly influences the trajectory of the spacecraft, incorporating the thruster controls into the trajectory optimisation increases the flexibility of operations.

5-2 Statement of the problem

5-2-1 Spacecraft dynamics

The spacecraft dynamics used in this work until now is presented in section 3-7-1-2. The equation of motion considers the 2-body dynamics, third body perturbations, and the solar radiation pressure. An ephemeris model that incorporates the real time positions of the celestial bodies is used. In section 3-7, the in-house MATLAB code DIRECT collocation Tool for Trajectory Optimization (DIRETTO) is introduced. The non-linear optimal control problem is solved by direct transcription through collocation to a Non-Linear Programming (NLP). Then, an interior point method is used to solve the NLP problem [153].

However, DIRETTO was not created to handle the incorporation of thruster physics and the subsequent optimisation of thruster control parameters along with trajectory optimisation. The complexity involved in the concurrent optimisation through DIRETTO is enormous in terms of computational resources and time.

For the purpose of demonstrating the incorporation of thruster control into the trajectory optimisation problem, a simple but effective method is introduced. First, the dynamics have to be redefined. A simple 2-body problem is considered for this application and the complexities such as solar radiation pressure and third body perturbations are removed. The reference frame is an inertial frame centered at the Sun since the heliocentric transfer trajectory is simulated.

The state vector and the control are expressed in equations (5-2) and (5-3), respectively.

$$\vec{x} \equiv \begin{Bmatrix} \vec{r} \\ \vec{v} \\ m_{sc} \end{Bmatrix} \quad (5-2)$$

$$\vec{u} \equiv \begin{Bmatrix} V_{grid} \\ \dot{m}_0 \\ P_{RF} \\ \alpha \\ \beta \end{Bmatrix} \quad (5-3)$$

The state vector \vec{x} comprises the position vector \vec{r} , the velocity vector \vec{v} , and the spacecraft mass m_{sc} . The control comprises the thruster control parameters V_{grid} , \dot{m}_0 and P_{RF} , and the thrust directional control angles α and β , which are the azimuth and elevation thrusting angles. The angles α and β are the control parameters for the trajectory. Thus, by incorporating all the control parameters, we make way for a concurrent optimisation problem.

The equations of motion are,

$$\frac{d\vec{x}}{dt} = \begin{bmatrix} v_r \\ \vec{f}_{2B} + \vec{f}_T \\ -\dot{m}_0 \end{bmatrix} \equiv \vec{\mathcal{F}}[(\vec{x}(t), \vec{u}(t), t)] \quad (5-4)$$

The thrust contribution \vec{f}_T is,

$$\vec{f}_T = \frac{T(V_{grid}, \dot{m}_0, P_{RF})}{m_{sc}} \begin{bmatrix} \sin \alpha \cos \beta \\ \cos \alpha \cos \beta \\ \sin \beta \end{bmatrix} \quad (5-5)$$

Here, the thrust T magnitude is a function of the control parameters V_{grid} , \dot{m}_0 and P_{RF} , obtained from the thruster performance envelope. The multiplier term that consists of α and β determines the direction of thrust. The rate of change of the spacecraft mass \dot{m}_{sc} is essentially the propellant consumption represented by $-\dot{m}_0$.

5-2-2 Boundary conditions

The spacecraft departs from the Earth’s sphere of influence $R_{SOI,E}$ that is farthest from the Sun on the Sun–Earth line at t_d and arrives at the ballistic capture target point at t_f . This t_f is free to be optimised. Since the ephemeris model is not utilised, the model is autonomous and t_d is set to zero without any loss of generality. The departure and arrival boundary conditions are expressed in equations (5-6)– (5-8). They are expressed in Cartesian coordinates.

$$\Psi_d [\vec{x}_d(t_d), t_d] \equiv \begin{bmatrix} t_d \\ r_x(t_d) - [r_{x,E}(t_d) + R_{SOI,E,x}] \\ r_y(t_d) - [r_{y,E}(t_d) + R_{SOI,E,y}] \\ r_z(t_d) - [r_{z,E}(t_d) + R_{SOI,E,z}] \\ v_x(t_d) - v_{x,E}(t_d) \\ v_y(t_d) - v_{y,E}(t_d) \\ v_z(t_d) - v_{z,E}(t_d) \\ m_{sc}(t_d) - m_{wet} \end{bmatrix} = \vec{0} \quad (5-6)$$

$$\Psi_f [\vec{x}(t_f)] \equiv \begin{bmatrix} r_x(t_f) - r_{x,C}(t_f) \\ r_y(t_f) - r_{y,C}(t_f) \\ r_z(t_f) - r_{z,C}(t_f) \\ v_x(t_f) - v_{x,C}(t_f) \\ v_y(t_f) - v_{y,C}(t_f) \\ v_z(t_f) - v_{z,C}(t_f) \end{bmatrix} = \vec{0} \quad (5-7)$$

$$\Psi_t(t_f) \equiv t_f - t_\infty \leq 0 \quad (5-8)$$

The settings of the departure point and capture point are obtained from the analysis performed in section 3-7.

5-2-3 Constraints and objective

The control parameters serve as the optimisation variables. This flight time t_f corresponds to the time of flight from the departure point at $R_{SOI,E}$ to the target point at which the ballistic capture initiates. The constraints are shown in in equation (5-9).

$$\mathcal{G} [\vec{x}(t), \vec{u}(t)] \equiv \begin{bmatrix} V_{grid}(t) - V_{grid,max} \\ V_{grid,min} - V_{grid}(t) \\ \dot{m}_0(t) - \dot{m}_{0,max} \\ \dot{m}_{0,min} - \dot{m}_0(t) \\ P_{RF}(t) - P_{RF,max} \\ P_{RF,min} - P_{RF}(t) \\ \alpha(t) - \alpha_{max} \\ \alpha_{min} - \alpha(t) \\ \beta(t) - \beta_{max} \\ \beta_{min} - \beta(t) \\ P_{tot} - P_{in}(r) \\ P_{tot} - P_{in,max} \\ m(t) - m_{wet} \end{bmatrix} \leq \vec{0} \quad (5-9)$$

The constraints are defined such that the control parameters do not exceed their upper and lower bounds. The bounds for V_{grid} are 1900 V and 2100 V, for \dot{m}_0 are 45 $\mu\text{g/s}$ and 60 $\mu\text{g/s}$, and for P_{RF} are 5 W and 40 W, which are in accordance with the thruster performance envelope defined earlier in section 5-1. The quantities α and β essentially are free of bounds but one can decide to impose limits if required. The most crucial constraint here is the one placed on total power P_{tot} . Considering the system requirements (EP-02 in Table 3-5), the maximum power available to the system is 70 W, out of which 3 W go to the PPCU. Thus, the thruster operates with a maximum power of 67 W. Additionally, as the Sun-spacecraft distance increases, the power available to the thruster P_{in} reduces and depends upon r . The power constraint is a non-linear inequality constraint. However, if one chooses to maximise the power utilisation, this constraint can be set as a non-linear equality constraint.

The objective of the optimisation is the minimisation of time. It is expressed as,

$$J = t_f \quad (5-10)$$

5-3 Numerical simulation

In the simulations presented in section 3-7-4, the departure and capture points are defined in spherical coordinates in the heliocentric reference frame HEO@ t_d . These points are retrieved and expressed in Cartesian form to speed up the simulation. A simple shooting technique is used to transcribe the optimal control problem to an NLP problem.

1. The time span t_f is discretized into nodes.
2. Initial guesses for the control parameters at each node are supplied.
3. The spacecraft dynamics equations are propagated until t_f , i.e., ‘shooting’ performed.
4. The error in the boundary conditions are evaluated.

5. The control variables are adjusted to satisfy the constraints using an NLP solver. Steps 1–4 are repeated until the optimal solution is found that satisfies the constraints and meets the boundary conditions.

The time span t_f is divided into several nodes and random values for the control parameters V_{grid} , \dot{m}_0 , P_{RF} , α , and β are supplied as initial guesses at each node. The time of flight t_f is also passed as an optimisation parameter with an initial guess value of 1250 days. The initial mass at departure m_d is fixed at 27.447 kg, the same value used in section 3-7-4.

The equations of motion are integrated until t_f and the control parameters are interpolated using piecewise cubic hermite polynomial (PCHIP) method between the nodes at each integration step. Thus, at each integration step, the interpolated control parameters are utilised to calculate the thrust magnitude T (see equation (5-5)). This influences the dynamics and consequently the spacecraft position and velocity. The position in turn affects the power. The loop is closed as the power influences T and I_{sp} .

The relationships between the control parameters V_{grid} , \dot{m}_0 and P_{RF} , and T , I_{sp} and P_{tot} are obtained from the thruster performance envelope by using a multivariate polynomial regression [164, 165]. Polynomial expressions for T , I_{sp} and P_{tot} with the 3 control parameters as the variables are generated and the interpolated values are supplied to calculate the corresponding magnitudes.

The final states after each integration are retrieved and the boundary conditions are checked. The final position and velocity must match the target position and velocity within a tolerance value of 10^{-6} . The initial state vector \vec{x}_d and final state vector \vec{x}_f are expressed in equation (5-11). The positions are in kilometre, the velocities are in kilometre per second, and the mass is in kilogram.

$$\vec{x}_d \equiv \begin{bmatrix} r_{x,E} \\ r_{y,E} \\ r_{z,E} \\ v_{x,E} \\ v_{y,E} \\ v_{z,E} \\ m_{sc} \end{bmatrix} = \begin{bmatrix} 1.5296 \times 10^8 \\ 0 \\ 0 \\ 0.0894 \\ 29.2873 \\ 0 \\ 27.447 \end{bmatrix} \quad \vec{x}_f \equiv \begin{bmatrix} r_{x,C} \\ r_{y,C} \\ r_{z,C} \\ v_{x,C} \\ v_{y,C} \\ v_{z,C} \\ m_f \end{bmatrix} = \begin{bmatrix} -1.7867 \times 10^8 \\ 1.311 \times 10^8 \\ 9.2324 \times 10^5 \\ -16.4623 \\ -18.3460 \\ 0.0347 \\ \text{free} \end{bmatrix} \quad (5-11)$$

The minimisation problem is solved using an interior point method through MATLAB's `fmincon` to find the minimum of the constrained multi-variable functions. The objective function $J = t_f$ is minimised. The non-linear constraints are evaluated at each iteration and the optimisation procedure runs until they are satisfied. One of the key non-linear inequality constraints is the power constraint, i.e., $P_{tot} \leq P_{in}(r)$. The number of non-linear constraints constructed for power is equal to the number of nodes, and P_{tot} and $P_{in}(r)$ are evaluated at each node and checked whether they satisfy the constraint.

The position vectors (r_x , r_y and r_z) in the Cartesian form are evaluated at each node and their norm is calculated to obtain the magnitude of the Sun–spacecraft distance. Using the inverse square law and considering the power production capabilities of MARIO solar panels, the maximum power availability to the thruster at that distance $P_{in}(r)$ is calculated. Of course, the maximum input power requirement of 67 W is applied if $P_{in}(r) > 67$. The value of P_{tot}

at each node is obtained by evaluating the polynomial expression obtained using multivariate polynomial regression. Satisfying this constraint ensures that the thruster is operating within its performance envelope.

The optimisation procedure completes when the constraints are satisfied and the boundary conditions are met. The results contain the optimised values for the control parameters V_{grid} , \dot{m}_0 , P_{RF} , α and β . The values of T , I_{sp} and P_{tot} along the trajectory are calculated using the optimised control parameters. The results of the optimisation are presented in Figure 5-5.

From Figure 5-5, it can be observed that the mass flow rate \dot{m}_0 reaches the maximum value. The inference is that the minimisation of time leads to the thrust being increased. Since the problem is power constrained, the parameter V_{grid} is adjusted until this constraint is satisfied and the \dot{m}_0 , which also influences the thrust through the neutral gas, is increased as much as its maximum value to yield the highest attainable thrust. The variations of α and β are between -200° to $+200^\circ$. The parameter β reaches zero near the end. The values of P_{tot} is maximum until near the end where the Sun-spacecraft distance increases and the value decreases to the reduced availability of power. The thrust T is high and continuous since time-optimal problems require such continuous thrusting operations.

The overall time of transfer t_f is 1485.5 days and the overall propellant consumption is 7.69 kg, which are higher than the results obtained in section 3-7-4. There are multiple reasons to this. The numerical scheme and the dynamics used in the previous simulations are much more robust compared to the schemes used in this analysis. Thus, the results are bound to be 'more optimised' in the case of DIRETTO simulations. The specific impulse I_{sp} value obtained in the current analysis is lower than that of the results obtained by DIRETTO. The thruster was operated at a fixed flow rate of 48 $\mu\text{g/s}$ in the previous case whereas it stays around 60 $\mu\text{g/s}$. The increase in \dot{m}_0 leads to a decrease in I_{sp} , and given the thrusting time, the propellant consumption is higher.

The techniques used in this analysis are crucial for the future implementation of a more robust framework that concurrently optimises the thruster operation and the low-thrust trajectory. This introduces a direct and a flexible control capability to the spacecraft. The thrusting performance of the thruster is determined by these control parameters. The knowledge of the control parameters that directly control the thrusting performance is crucial as this information can be fed into the control algorithms in the on-board computer such that the spacecraft can be operated autonomously and with flexibility.

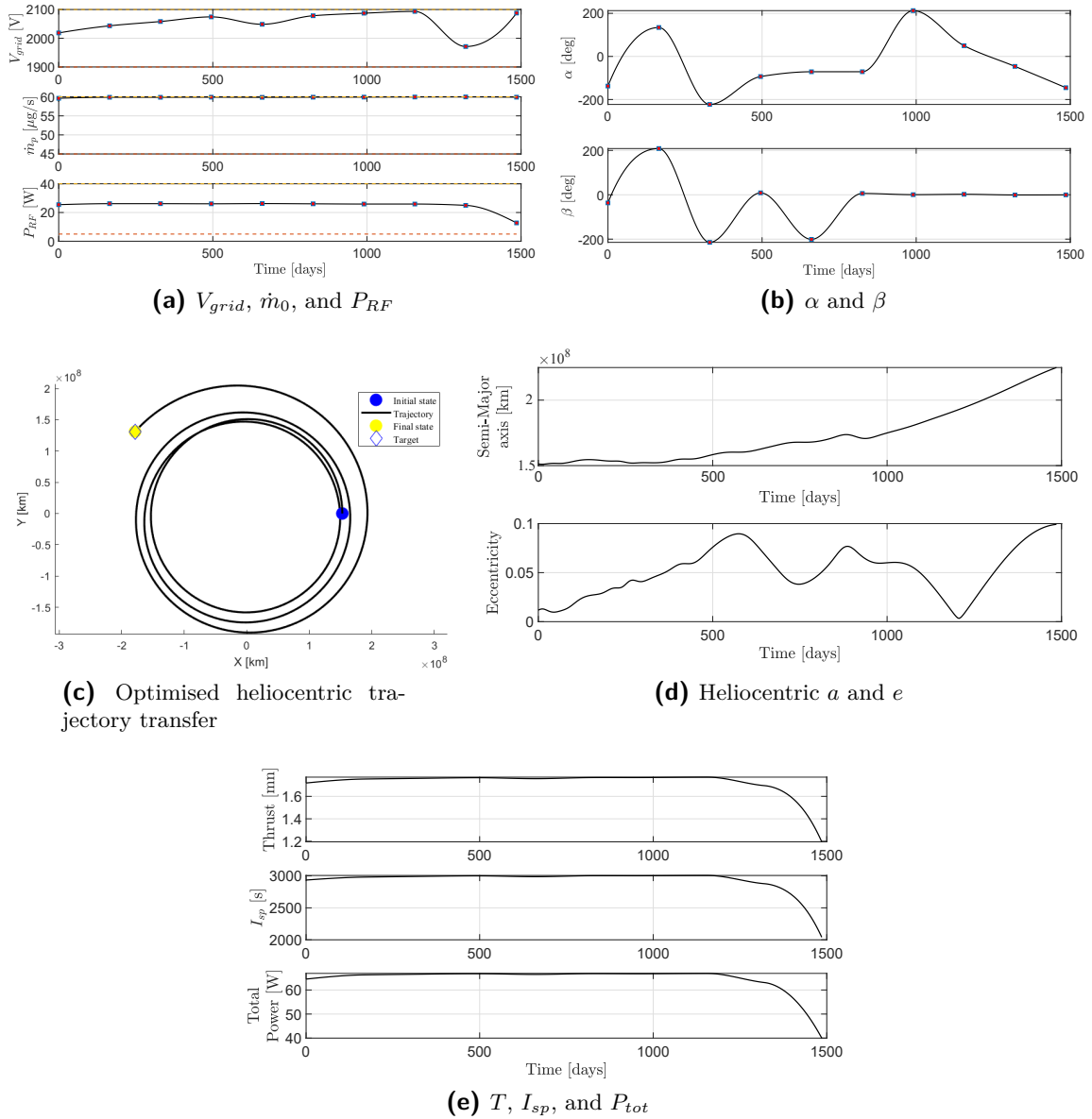


Figure 5-5: Concurrent thruster–trajectory optimisation. Figure (a) represents the optimised thruster control parameters V_{grid} , \dot{m}_0 , and P_{RF} . Figure (b) represents the optimised trajectory control parameters α and β . The final values at the nodes are indicated with a Figure (c) represents the optimised heliocentric transfer trajectory. Figure (d) represents the heliocentric semi-major axis a and eccentricity e . Figure (e) represents the thrust T , specific impulse I_{sp} , and total power P_{tot} along the heliocentric trajectory.

Chapter 6

Closure

6-1 Summary

The first chapter introduced the basics of interplanetary CubeSat missions and their corresponding challenges. The need for primary propulsion for stand-alone deep-space CubeSat missions is established since orbital manoeuvring and precise trajectory control capabilities are indispensable to ensure mission success. The motivation for the research work is established and the key concept of combined chemical–electric propulsion is introduced. Hybrid transfer solutions that utilise chemical–electric propulsion achieve a balance between system mass and transfer time. The main objectives are then established:

1. **Provide design solutions for combined chemical–electric propulsion systems that enable stand-alone CubeSat missions on a deep-space cruise.**
2. **Develop a methodology for concurrent systems–trajectory design and establish an overall design framework for an interplanetary CubeSat mission.**
3. **To transpose the knowledge of combined propulsion design, concomitant with optimal trajectories for future interplanetary CubeSat designers and propulsion system developers to enhance solar system exploration efforts at high science-to-investment ratio.**

MARIO mission application case is defined with its four key phases: a) orbit raising & Earth escape, b) low-thrust deep-space cruise c) ballistic capture at Mars and d) acquisition of the final operating orbit at Mars. The high-thrust chemical propulsion is used in orbit raising and Earth escape as well as Mars orbit stabilisation. The low-thrust electric propulsion is used in deep-space cruise and final circularization to an operational orbit. The propulsion design solutions are pursued by considering the mission context. To achieve the research objectives, the corresponding research questions that need to be answered are listed.

Chapter 2 deals with the chemical propulsion system and the high-thrust trajectory. The state-of-the-art chemical propulsion systems applicable for CubeSats, such as solid rocket motors, liquid monopropellant and bipropellant engines as well as cold gas propulsion systems, are studied and analysed. The system design strategy is elaborated and a trade-off is performed to select the best suited system type based on the requirements. Green monopropellant systems are chosen for the design. Propellant properties are evaluated and thermochemical analysis is pursued to characterise the propellant performance. Green propellants such as blends of Ammonium Dinitramide (ADN) and Hydroxylammonium Nitrate (HAN) are compared. Chemical thruster design is pursued and overall system sizing and feed system design is done to deliver the ΔV requirements of the high-thrust trajectory.

Chapter 3 focuses on the electric propulsion system and the low-thrust trajectory. The state-of-the-art of electric propulsion that is applicable for CubeSats is documented. A comparison between gridded ion thrusters, Hall effect thrusters, field emission electric propulsion, pulsed plasma thrusters and helicon thrusters are made and a trade-off based on the system requirements is performed. Gridded ion thrusters excited with a radiofrequency power source is chosen for the design. An analysis of propellants, xenon and iodine, is done and iodine is chosen for its compactness, cost effectiveness and high performance yield. The physics behind the operation of a radiofrequency ion thruster are highlighted and a performance model is implemented to obtain the variations of thrust and specific impulse with input power. A power constrained low-thrust trajectory optimisation using the thruster performance model is pursued to calculate the transfer time, ΔV , and the required propellant mass for the heliocentric transfer and ballistic capture. Circularization onto an operational orbit about Mars is also detailed. Finally, the system sizing is presented.

Chapter 4 presents the overall system design of MARIO. The system architecture and flight systems design that includes information on subsystems such as power, communications etc. are presented. The focus is on preliminary systems design in order to provide an overview of the mission and a context for the propulsion systems design. The configuration of the MARIO spacecraft and the system budgets are also presented.

Chapter 5 deals with the concurrent propulsion–trajectory optimisation. Thruster performance envelope is established and a novel framework for the concurrent optimisation of the thruster and the low-thrust trajectory control parameters is set up. The heliocentric transfer trajectory is simulated and the control parameters are optimised to yield a minimum flight time. The knowledge of these parameters allows for a direct implementation into the control law algorithms on the on-board processor for flexible, autonomous and responsive operations during flight and shall enable a prudent design of autonomous interplanetary CubeSats.

6-2 Conclusion

This section highlights the main findings and conclusions derived from this work. The research questions that were posed in the beginning are answered and the rationale behind them are expounded.

6-2-1 On the combined chemical–electric propulsion design and hybrid trajectory

This section aims to answer three research questions:

1. What is the design strategy for combined chemical–electric propulsion for a stand-alone CubeSat to Mars?
2. What are the design and performance characteristics for combined chemical–electric propulsion that enable a stand-alone CubeSat to Mars?
3. What are the trajectory characteristics of a stand-alone CubeSat mission to Mars?

Short answer: Combined chemical–electric propulsion systems are *separate systems present in the same spacecraft*, and are operated alternatively. The overall system design strategy is illustrated in Figure 6-1. The chemical propulsion system is utilised in orbit raising and Earth escape as well as Mars orbit stabilisation. The electric propulsion system is used in low-thrust deep-space cruise and ballistic capture as well as final circularization. The design solution for the chemical propulsion system yields a thrust of 3 N and an I_{sp} of 241.2 seconds while using ADN-blend propellant called FLP-106. The propellant mass is 5.725 kg, which corresponds to a margined ΔV of 445 m/s. The overall chemical propulsion system mass is 6.91 kg and it occupies a volume of 8U. The design solution for the electric propulsion system yields a max thrust of 1.492 mN and a max I_{sp} of 3168 seconds. The thrust and I_{sp} vary with input power. The propellant mass is 5.87 kg. The overall electric propulsion system mass is 6.57 kg and it occupies 3U volume. The systems are designed to execute a hybrid high-thrust–low-thrust trajectory. The sequence is high-thrust orbit raising and Earth escape, low-thrust deep-space cruise and ballistic capture, high-thrust Mars orbit stabilisation, and low-thrust circularization. The overall transfer time is 1472.69 days.

Explanation: Fully-chemical transfers are fast but lead to an excessive system mass. Fully-electric transfers save mass but have untenable escape times. Hybrid transfer solutions that utilise chemical–electric propulsion achieve a balance between system mass and transfer time. The mission characteristics are defined such that the spacecraft has to escape Earth, pursue low-thrust deep-space cruise, achieve ballistic capture and acquire an operational orbit at Mars. The system characteristics are defined and the requirements and initial parameters for the propulsion system are set. The state-of-the-art technologies and concepts applicable for CubeSats are explored and a trade-off analysis is done to select the suitable systems, each for chemical and electric propulsion. Propellant analysis and characterisation is then done. Thruster design parameters are predicted and iterated until the performance requirements are delivered.

The design of the chemical propulsion system is based on the total ΔV requirement for Earth escape and Mars orbit stabilisation. Considering a 10% margin on each of those, $\Delta V_{tot,mg} =$

445 m/s. Additionally, constraints on thrust, burntime and total system mass were also placed. The design strategy is illustrated in Figure 6-1 (red part). The chemical propulsion system selected for design is the green monopropellant system that uses the propellant FLP-106, which is a blend of ammonium dinitramide (ADN). Compared to hydrazine, FLP-106 has a higher density (1357 kg/m^3), very high I_{sp} and is non-toxic. Thruster design and performance analysis is performed to calculate the size of the thruster to yield the required performance. The thruster operates at 2 MPa combustion pressure and has a combustion chamber volume of 662.7 mm^3 . The nozzle throat diameter is 0.75 mm and the expansion area ratio is 200. With an expansion half angle of 15° , the nozzle length is 18.47 mm. Two thrusters are used and the total thrust yield is 3.072 N and the I_{sp} yield is 241.2 seconds. The mass of two thrusters is 0.4 kg. The total propellant mass is 5.725 kg, with a break down of 4.993 kg for $\Delta V_{esc,mg}$, 0.459 kg for $\Delta V_{stab,mg}$ and 0.273 kg for reaction control. The total propellant volume is 4218.6 cm^3 . Four elliptical dome ended cylindrical tanks are used to accommodate the propellant and each has a volume of 1160.1 cm^3 including a 10% ullage. The tank dimensions are 9.4 cm diameter and 18.05 cm height. The tanks are designed for a burst pressure of 3.9 MPa and a nominal feed pressure of 2.2 MPa. A pressuriser tank with a volume of 492 cm^3 containing gaseous nitrogen at 28 MPa is designed to maintain the propellant tank pressure. The total feed system volume is 8U and the corresponding dry mass is 0.784 kg (including the pressurant gas mass). The overall mass of the chemical propulsion system is 6.91 kg, which is 21.59% of the initial spacecraft mass of 32 kg.

The spacecraft is injected into a $295 \text{ km} \times 90,000 \text{ km}$ orbit. The high-thrust trajectory is executed in multiple burns to raise the orbit and then perform a final manoeuvre to achieve Earth escape. Six burns are executed about the perigee for a burn duration of 598.6 seconds each. The burn duration is split equally before and after the perigee. The cumulative thruster burntime is 3591.6 seconds. The overall flight time until reaching eccentricity $e = 1$ is 792.73 hours (~ 33.03 days). An additional ~ 30 days is assumed as the coasting period until the Earth's sphere of influence is reached.

The design of electric propulsion system is based on the requirements placed on maximum transfer time and maximum power consumption. Constraints are placed on the total system mass and consideration is also given to the accommodation of the propellant within the CubeSat structure. The design strategy is illustrated in Figure 6-1 (green part). The type of electric propulsion system chosen for design is a miniaturised inductively-coupled radiofrequency gridded ion thruster using iodine propellant. Iodine propellant is chosen for its high density (4940 kg/m^3) and compact storability due to its existence in solid state in standard conditions. Additionally, in comparison with xenon, iodine is low-cost, abundant and yields a similar performance. The thruster has a diameter of 2.5 cm and a length of 2.2 cm. The plasma chamber volume is 10.79 cm^3 . The initial mass flow rate is maintained at $48 \text{ } \mu\text{g/s}$ and the grids are maintained at 2000 V potential difference for ion acceleration. The maximum thrust yield is 1.492 mN and the maximum I_{sp} is 3168 seconds, considering the maximum input power of 67 W. The thrust and I_{sp} increase/decrease with increasing/decreasing input power, which in turn depends upon the Sun-spacecraft distance. The total propellant mass amounts to 5.87 kg, with a break down of 4.892 kg for time-optimal heliocentric transfer, 0.178 kg for low-thrust circularization, and $\sim 16\%$ margin for contingency and station-keeping. A thermoplastic propellant tank with a volume of 1308 cm^3 and dimensions of $20 \text{ cm} \times 10 \text{ cm} \times 6.54 \text{ cm}$ is used to store the propellant. Including the PPCU and the feed system, the

overall volume amounts to 3U. The overall system mass is 6.57 kg, which is 20.53% of the initial spacecraft mass of 32 kg.

The thruster performance in terms of T and I_{sp} vs input power is utilised to solve an optimal control problem to optimise the heliocentric trajectory and ballistic capture. Time-optimal continuous thrust technique and fuel-optimal bang-bang control techniques were investigated and the time-optimal solution was chosen since the difference was 100 days of lesser flight time for a penalty of 0.4 kg propellant mass. The total time of flight is 1250 days with a continuous thrusting period of 1186.83 days. The cumulative ΔV is 5.837 km/s. The amount of revolutions around the Sun to reach Mars from Earth is 3. After ballistic capture, low-thrust circularization replaces the spacecraft at a 60,000 km circular orbit about Mars, which takes 159.66 days and consumes 0.178 kg.

Overall, the combined chemical–electric propulsion systems weigh 13.48 kg, which is $\sim 42.12\%$ of the initial spacecraft wet mass of 32 kg. They occupy a total volume of 11 U in a 16U spacecraft. The end-to-end transfer time of orbit raising and Earth escape, low-thrust deep-space cruise and ballistic capture, high-thrust Mars stabilisation and finally low-thrust circularization is 1472.69 days, which is ~ 4.035 years. The requirements for the total propulsion system mass and the total transfer time are satisfied.

6-2-2 On the concurrent systems–trajectory design framework

This section aims to answer the research question,

1. How can the low-thrust propulsion system and trajectory be concurrently optimised?

Short answer: Low-thrust propulsion system and the trajectory can be concurrently optimised by designing a framework in which the control parameters that dictate the thruster performance and the control parameters that dictate the orbital propagation are optimised together to satisfy the boundary conditions and constraints. This shall lead to a more comprehensive mission design.

Explanation: The concurrent optimisation strategy involves the use of control parameters that directly affect the thruster and the trajectory. Nominally, in low-thrust trajectory optimisation problems, the thrust T is used as a control parameter. However, the key parameters that determine the thrust and subsequently the entire thruster physics are not taken into account. The concurrent optimisation strategy incorporates these control parameters which have a direct influence on the thruster performance, which consequently affects the trajectory. In total, there are 5 control parameters, 3 for the thruster and 2 for the trajectory. The thruster control parameters are the grid voltage V_{grid} , mass flow rate \dot{m}_0 , and the input radiofrequency power P_{RF} . The trajectory control parameters are the two thrusting angles which determine the direction of thrust: azimuth angle α and elevation angle β .

First, the thruster performance envelope must be defined. In the current application case, the performance parameters thrust T , specific impulse I_{sp} , and total power P_{tot} are calculated for ranges of V_{grid} , \dot{m}_0 and P_{RF} . The state vector and the control vector are defined and the equations of motion are written. The specific force due to thrust, as a function of the control parameters, is incorporated into the dynamics. The initial and final boundary conditions are

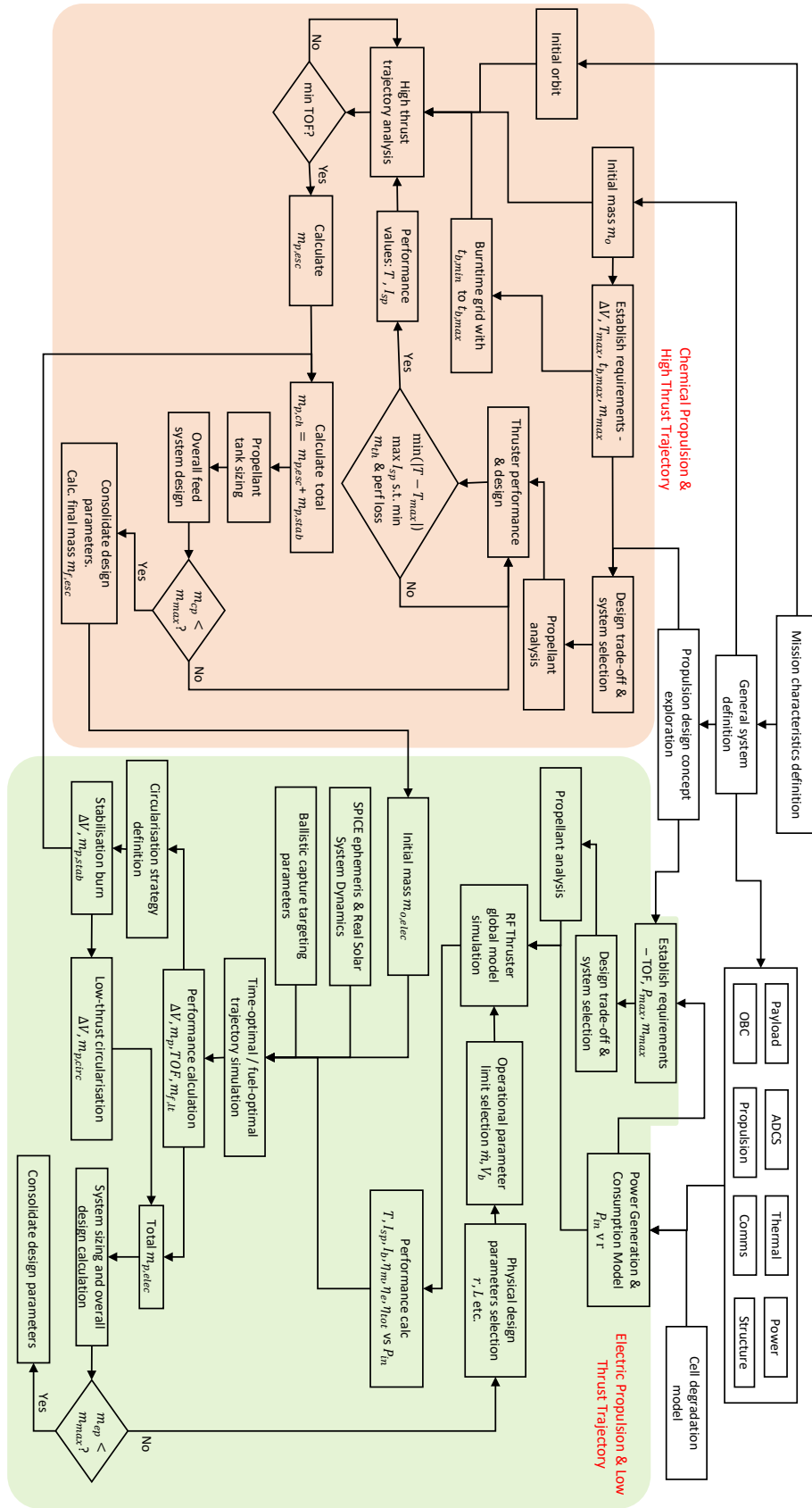


Figure 6-1: Overall combined chemical-electric propulsion system design strategy

defined along with the constraints and the objective. The initial state comprises the initial position that is the Earth sphere of influence and the initial velocities and spacecraft mass. The final state comprises the final position and velocity at a target point, which shall lead to a ballistic capture at Mars. The critical constraint here is the power constraint. The total power calculated using the thruster control parameters shall be less than or equal to the maximum allowable thruster power input. The objective is the minimisation of time.

Simple shooting technique is used to transcribe the optimal control problem into a non-linear programming problem. The total flight time is discretized into a series of nodes and the initial guesses for the control parameters at each node are supplied. The spacecraft equations of motion are integrated over the flight time, i.e. ‘shooting’ is performed. The error in the boundary conditions are evaluated. Using an NLP solver, the control parameters are then adjusted until the constraints are satisfied and the boundary conditions are met. The steps are repeated until an optimal solution is found.

The techniques used in this analysis are crucial for the future implementation of a more robust framework that concurrently optimises the thruster operation and the low-thrust trajectory. This introduces a direct and a flexible control capability to the spacecraft. The thrusting performance of the thruster is determined by these control parameters. The knowledge of the control parameters that directly control the thrusting performance is crucial as this information can be fed into the control algorithms in the on-board computer such that the spacecraft can be operated autonomously and with flexibility.

6-2-3 Recommendations to spacecraft designers

One of the primary objectives of this work is to provide a design framework and solution of propulsion systems such that spacecraft designers can focus their development efforts on enabling the technologies that are required to achieve stand-alone CubeSat missions like MARIO.

The main ‘take aways’ from this research work are:

- ▶ The design of propulsion systems for stand-alone deep-space CubeSats is heavily mission dependent. The primary factors that influence the design are the initial injection orbit, the final target, and the design constraints. For a 16U CubeSat that is launched into a high-energy Earth orbit, the most suitable solution is the combined chemical–electric propulsion system that enables a hybrid high-thrust–low-thrust transfer trajectory thereby balancing flight time and system mass.
- ▶ The design solution achieved in this work for the combined chemical–electric propulsion satisfies the requirements and yields a feasible solution for a stand-alone CubeSat mission to Mars.
- ▶ The choice of propulsion system type is crucial. CubeSats are secondary payloads and the usage of green propulsion becomes imperative in order to protect the primary payload and to avoid self-damage. Additionally, CubeSat design philosophy involves simplified systems design and operation. This reduces cost and complexity, thereby ensuring affordability and reliability. Monopropellant systems are well suited for missions

involving Earth escape. They provide a high performance while having relatively low complexity. Usage of chemical propulsion ensures swift escape, thereby significantly reducing radiation damage.

- ▶ Electric propulsion and low-thrust trajectory design is the most crucial aspect of stand-alone CubeSat mission design. A high specific impulse system ensures significant mass savings and a compact propellant ensures significant volume savings. Gridded ion thrusters utilising iodine propellant are highly suitable for this class of missions. Precision control of the trajectory is enabled through low-thrust propulsion and the achievement of the target is guaranteed.
- ▶ Ballistic capture at the target planet must be exploited in stand-alone CubeSat missions since the natural dynamics ensure that there is no propellant mass required to achieve a successful capture.
- ▶ The design framework for concurrent low-thrust propulsion and trajectory optimisation is crucial for enabling direct control over spacecraft motion. This paves the way for a comprehensive design of the thruster and the mission, and enables flexible and autonomous operations in future.
- ▶ Enabling combined chemical–electric propulsion system shall lead to a major paradigm shift in solar system exploration efforts using CubeSats at a very high science-to-investment ratio. Although the risk is higher than that of traditional interplanetary missions, the gain is significantly high.

Multiple points of improvement can be addressed in the further stages of research. Firstly, chemical propulsion system design could be further refined by performing in-depth CFD analyses and experiments to determine the full-scale system performances. A combined analysis of chemical propulsion and attitude control system is required for optimising operations. Although there are reaction wheels and reaction control systems that can handle a ~ 3 N thrust on small spacecraft, a detailed analysis would be useful for fine-tuning the throttle control.

Electric propulsion systems utilising iodine propellant are at their nascent stage of development. A higher level of system maturation and space qualification is yet to be achieved. Full particle-in-cell (PIC) or Hybrid fluid–PIC simulations that give in-depth information about the plasma processes in the ion thruster will be immensely helpful. This increases the fidelity of the thruster model and subsequent concurrent optimisation of the thruster and the trajectory.

6-3 Reflections of the author

During this work, the first issue encountered was the setting up of specific goals that had a good scientific value and achievable within an acceptable time frame. Design, development, testing and integration of chemical propulsion and electric propulsion for a CubeSat that goes all the way from Earth to Mars while being stand-alone is a near herculean task as the scope of investigation is extensively broad and deep. Indeed, the development of each of these individual systems itself requires a dedicated doctoral research.

Thus, it was decided to pursue a key scientific objective of providing a design solution for combined chemical–electric propulsion along with hybrid high-thrust–low-thrust trajectories such that a feasible solution in terms of system mass and flight time could be achieved for a CubeSat that shall travel from Earth orbit to Mars. This work was deemed feasible within the time frame and would provide a very good starting point for any future research on stand-alone interplanetary CubeSats. Transposing the knowledge of the propulsion system design for spacecraft designers and propulsion system developers was seen as an important step that shall drive the industry to enable the required technologies.

Context to the research is crucial since the scope of interplanetary CubeSats is broad. The research was pursued with an ambitious mission in mind, albeit sensible and potentially feasible. The mission definition involved multiple feats that have never before been achieved by CubeSats. First, no CubeSat has achieved Earth escape by itself. Second, no CubeSat has pursued an autonomous heliocentric transfer, especially after achieving that Earth escape. Third, no CubeSat has achieved a ballistic capture at a planet and finally, no CubeSat has ever been placed on an operational orbit about Mars. The goal of this research was set to enable a CubeSat mission to achieve these feats.

As the design process proceeded, different options were considered for the type of propulsion systems and the depth of analysis required. It became clear that for chemical propulsion system, a thermochemical calculations and performance analysis would lead to a design solution of sufficient depth and accuracy that shall fit the scope of the overall analysis. The high thrust trajectory simulations, with the assumptions of a two-body problem, would then be sufficient to provide system sizing solution required. The design and sizing parameters were calculated using the standard design principles. Although CFD simulations would have helped shed more light on the thruster physics, the objectives of the work and the timeframe in which these objectives need to be achieved as well as the usefulness in the current scope of analyses gave an impression that this should be reserved for the future.

For the electric propulsion system, basic performance equations were not sufficient to properly model the thruster. Initially, a linear model was assumed for the thrust and the specific impulse with fixed efficiencies and the trajectory was simulated. However, the author was not satisfied with depth of the analysis with linear models. Thus, it was decided to implement a global performance model using iodine which represented the thruster physics much better. Very good insight was obtained while modelling the plasma processes and subsequently the thruster performance w.r.t. input power. The trajectory optimisation tool used is DIRETTO and the thruster performance was incorporated through a curve-fit. Although it was not guaranteed to yield the desired results, it was a pleasant feeling when the final trajectory computations yielded the results that the author had hoped for.

Regarding the concurrent optimisation, the author aimed to implement a simplified but effective algorithm to demonstrate that the thruster and the trajectory can indeed be optimised concurrently. Although the best outcome would have been a direct implementation into DIRETTO, the structure in which DIRETTO was coded made the incorporation way too complicated. Since the primary focus from the initial point was on propulsion systems design, a complete redesign of DIRETTO for this particular was seen as cumbersome and eventually not yielding extraordinarily improved results. Although some more robustness could be applied, such as the inclusion of ephemeris model, the approach to the analysis was seen as sufficient for the purpose of demonstration.

The author definitely had the idea to do a complete and end-to-end systems and trajectory optimisation. That is, from the start point to the end point every single aspect of chemical and electric propulsion systems as well as the high-thrust and low-thrust trajectories incorporated into a monolithic optimisation scheme. However, it was found that some parts of analyses required different software and different techniques. No single programming platform could handle the enormity of all-inclusive framework. The scales of dynamics and optimisation are vastly different and a complete incorporation would result in an inefficient scheme that yields inaccurate results and would consume exceptionally large computational resources as well as time. Of course, an all-encompassing optimisation scheme sounds immense and ground breaking, but considering practicality, the creation of such a framework that yields accurate and globally optimised results while consuming limited computational resources seems phantasmagorical, at least at the time of this work.

Glossary

List of Acronyms

ADN	Ammonium dinitramide
CG	Cold Gas
CP	Chemical Propulsion
COTS	Commercial off-the-shelf
DIRETTO	DIRect colocation Tool for Trajectory Optimization
EP	Electric Propulsion
ESA	European Space Agency
FEED	Field Emission Electric Propulsion
GIT	Gridded Ion Thruster
HAN	Hydroxylammonium nitrate
HET	Hall Effect Thruster
HPGP	High performance green propulsion
HRE	Hybrid Rocket Engine
HTPB	Hydroxyl-terminated polybutadiene
JPL	Jet Propulsion Laboratory
LEO	Low-Earth Orbit
LRE	Liquid Rocket Engine
MarCO	Mars Cube One
M-ARGO	Miniaturised - Asteroid Remote Geophysical Observer

MARIO	Mars Atmospheric Radiation Imaging Orbiter
NASA	National Aeronautics and Space Administration
NLP	Non-Linear Programming
PPCU	Power Processing and Control Unit
SRM	Solid Rocket Motor
SRP	Solar Radiation Pressure
TRL	Technology Readiness Level

List of Symbols

α	Azimuth angle for thrusting
α_d	Nozzle divergence angle
β	Elevation angle for thrusting
β_g	Grid transparency for neutral gas
β_i	Grid transparency for ions
η_c	Combustion efficiency
η_m	Mass utilization efficiency
η_n	Nozzle efficiency
η_p	Thruster power efficiency
η_{tot}	Total efficiency
Γ	Particle flux [$1/m^2s$]
κ	Thermal conductivity [W/mK]
κ_B	Boltmann constant [J/K]
Λ_0	Heat diffusion length [m]
μ	Gravitational parameter of Earth [km^3/s^2]
Ω_{el}	Rate of electron-neutral elastic collisions [W/m^3]
Ω_{in}	Rate of ion-neutral elastic collisions [W/m^3]
ε	Expansion area ratio
ΔH_f^0	Heat of formation [kJ/mol]
\dot{m}	Mass flow rate [kg/s]
\mathcal{R}	Resistance [Ω]
\mathcal{T}_c	Combustion temperature [K]
\mathcal{T}_e	Electron temperature [K]
\mathcal{T}_g	Neutral gas temperature [K]
\mathfrak{M}	Molecular mass [amu]
A	Ion thruster cross sectional area [m^2]

A_c	Combustion chamber area [m ²]
A_e	Nozzle exit area [m ²]
A_{eff1}	Effective area for ion wall neutralization [m ²]
A_{eff}	Effective area for ion and electron wall losses [m ²]
A_g	Grid area for neutral gas [m ²]
A_{sr}	Surface recombination area [m ²]
A_{surf}	Total surface area [m ²]
A_t	Nozzle throat area [m ²]
c^*	Characteristic velocity [m/s]
C_F	Coefficient of thrust
D_c	Chamber diameter [m]
D_t	Nozzle throat diameter [m]
e	Electron charge [C]
E	Plasma process potential [J]
E_e	Electron energy [J/m ³]
E_g	Neutral gas energy [J/m ³]
F	Force [N]
g_0	Gravitational acceleration [m/s ²]
h_L, h_R	Edge-to-centre plasma density ratios
I	Total impulse [Ns]
I_{beam}	Beam current [A]
I_{sp}	Specific impulse [s]
K	Collision rate factor [m ³ /s]
k	Specific heat ratio
L^*	Characteristic length [m]
L_c	Chamber length [m]
L_{con}	Nozzle constriction length [m]
L_N	Nozzle divergent part length [m]
m	Mass [kg]
m_0	Initial mass [kg]
m_f	Final mass [kg]
m_p	Propellant mass [kg]
n	Particle number density [1/m ³]
P	Power [W]
p	Plasma process power [W/m ³]
P_a	Ambient pressure [Pa]
P_c	Combustion chamber pressure [Pa]
P_e	Nozzle exhaust pressure [Pa]
Q_0	Particle flow rate [Pa]
q_{th}	Rate of thermal diffusion [W/m ³]

R	Radius [m]
r	Spacecraft distance [km]
R_u	Throat longitudinal radius [m]
R_{gas}	Gas constant [kJ/kmol – K]
T	Thrust [N]
t_b	Burn time [s]
t_s	Residence time [s]
u	Throttle factor
$u_{Bohm,i}$	Ion bohm velocity [m/s]
V	Plasma chamber volume [m ³]
V_c	Combustion chamber volume [m ³]
v_e	Exhaust velocity [m/s]
v_g	Gas velocity [m/s]
$v_{beam,i}$	Ion beam velocity [m/s]
$v_{e,eff}$	Effective exhaust velocity [m/s]
v_i	Ion velocity [m/s]
$V_{s,c}$	Specific volume at combustion chamber [m ³ /kg]
$V_{s,t}$	Specific volume at throat [m ³ /kg]
w	Particle number density rate due to plasma processes [1/m ³ s]

Bibliography

- [1] Puig-Suari, J., Turner, C., and Ahlgren, W., “Development of the standard CubeSat deployer and a CubeSat class PicoSatellite,” *IEEE Aerospace Conference, Big Sky, MT, United States*, Vol. 1, IEEE, Mar 2001, pp. 1–7.
- [2] Swartwout, M., “The first one hundred cubesats: A statistical look,” *Journal of Small Satellites*, Vol. 2, No. 2, 2013, pp. 213–233.
- [3] Long, M., Lorenz, A., Rodgers, G., Tapio, E., Tran, G., Jackson, K., Twiggs, R., Bleier, T., and Solutions, S., “A cubesat derived design for a unique academic research mission in earthquake signature detection,” *16th Annual AIAA/USU Conference on Small Satellites, Logan, Utah, United States*, Aug 2002, pp. SSC02–IX–6.
- [4] Selva, D., and Krejci, D., “A survey and assessment of the capabilities of Cubesats for Earth observation,” *Acta Astronautica*, Vol. 74, 2012, pp. 50–68. doi:10.1016/j.actaastro.2011.12.014.
- [5] Swartz, W. H., Dyrud, L. P., Lorentz, S. R., Wu, D. L., Wiscombe, W. J., Papadakis, S. J., Huang, P. M., Reynolds, E. L., Smith, A. W., and Deglau, D. M., “The RAVAN CubeSat mission: advancing technologies for climate observation,” *Geoscience and Remote Sensing Symposium (IGARSS), Milan, Italy, IEEE*, July 2015, pp. 5300–5303.
- [6] Doe, R. A., and Watchorn, S., “Climate-monitoring cubesat mission (CM2): a project for global Mesopause temperature sensing,” *Earth Observing Systems XVI, San Diego, California, United States*, Vol. 8153, International Society for Optics and Photonics, Sep 2011, p. 81530Q.
- [7] Gill, E., Sundaramoorthy, P., Bouwmeester, J., Zandbergen, B., and Reinhard, R., “Formation flying within a constellation of nano-satellites: The QB50 mission,” *Acta Astronautica*, Vol. 82, No. 1, 2013, pp. 110–117. doi:10.1016/j.actaastro.2012.04.029.
- [8] Kitts, C., Ronzano, K., Rasay, R., Mas, I., Williams, P., Mahacek, P., Minelli, G., Hines, J., Agasid, E., Friedericks, C., et al., “Flight results from the GeneSat-1 biological microsatellite mission,” *21st Annual AIAA/USU Conference on Small Satellites, AIAA*, Aug 2007, pp. SSC07–XI–1.

- [9] Hodges, R. E., Hoppe, D. J., Radway, M. J., and Chahat, N. E., “Novel deployable reflectarray antennas for CubeSat communications,” *2015 IEEE MTT-S International Microwave Symposium, Phoenix, Arizona, United States*, IEEE, May 2015, pp. 1–4.
- [10] Hyvönen, P., Liljeblad, M., and Vidmark, A., “Deep Space Cubesat Communications,” *2018 SpaceOps Conference, Marseille, France*, May 2018, p. 2662.
- [11] Franzese, V., Di Lizia, P., and Topputo, F., “Autonomous Optical Navigation for LUMIO Mission,” *AAS/AIAA Space Flight Mechanics Meeting, Kissimmee, Florida, United States*, Jan 2018, pp. 1977–1987.
- [12] Franzese, V., and Topputo, F., “Line-of-Sight Deep-Space Autonomous Navigation,” *arXiv preprint arXiv:1909.08459*, Vol. 1, 2019, pp. 1–8.
- [13] Mueller, J., Hofer, R., and Ziemer, J., “Survey of Propulsion Technologies Applicable to Cubesats,” *Joint Army Navy NASA Air Force (JANNAF) Propulsion Meeting, Colorado Springs, United States*, May 2010, p. 1646.
- [14] Lemmer, K., “Propulsion for CubeSats,” *Acta Astronautica*, Vol. 134, May 2017, pp. 231–243. doi:10.1016/j.actaastro.2017.01.048.
- [15] Hodges, R. E., Radway, M. J., Toorian, A., Hoppe, D. J., Shah, B., and Kalman, A. E., “ISARA-integrated solar array and reflectarray CubeSat deployable Ka-band antenna,” *2015 IEEE International Symposium on Antennas and Propagation & USNC/URSI National Radio Science Meeting*, IEEE, 2015, pp. 2141–2142.
- [16] Yoon, S., Shin, Y., Jeon, J., Seo, Y., Jeon, J., Woo, J., and Seon, J., “Analysis of the charged particle radiation effect for a CubeSat transiting from Earth to Mars,” *Current Applied Physics*, Vol. 14, No. 4, Apr 2014, pp. 575–581. doi:10.1016/j.cap.2014.01.018.
- [17] Sinclair, D., and Dyer, J., “Radiation effects and COTS parts in SmallSats,” *27th Annual AIAA/USU Conference on Small Satellites, Logan, Utah, United States*, Aug 2013, pp. 1–12.
- [18] Topputo, F., and Belbruno, E., “Earth–Mars transfers with ballistic capture,” *Celestial Mechanics and Dynamical Astronomy*, Vol. 121, No. 4, 2015, pp. 329–346. doi:10.1007/s10569-015-9605-8.
- [19] Ofodile, I., Kütt, J., Kivastik, J., Nigol, M. K., Parelo, A., Ilbis, E., Ehrpais, H., and Slavinskis, A., “ESTCube-2 attitude determination and control: Step towards interplanetary CubeSats,” *2019 IEEE Aerospace Conference*, IEEE, 2019, pp. 1–12.
- [20] Furano, G., and Menicucci, A., “Roadmap for on-board processing and data handling systems in space,” *Dependable Multicore Architectures at Nanoscale*, Springer, Aug 2018, pp. 253–281. doi:10.1007/978-3-319-54422-9_10.
- [21] Klesh, A., Clement, B., Colley, C., Essmiller, J., Forgette, D., Krajewski, J., Marinan, A., Martin-Mur, T., Steinkraus, J., Sternberg, D., et al., “MarCO: Early Operations of the First CubeSats to Mars,” *32nd Annual AIAA/USU Conference on Small Satellites, Logan, Utah, United States*, Aug 2018, pp. 1–10.

- [22] Asmar, S., and Matousek, S., “Mars Cube One (MarCO): the first planetary CubeSat mission,” *Mars CubeSat/NanoSat Workshop, Pasadena, California*, Vol. 20, 2014, p. 21.
- [23] Walker, R., Binns, D., Bramanti, C., Casasco, M., Concari, P., Izzo, D., Feili, D., Fernandez, P., Fernandez, J. G., Hager, P., et al., “Deep-space CubeSats: thinking inside the box,” *Astronomy and Geophysics*, Vol. 59, No. 5, 2018, pp. 5–24. doi:10.1093/astrogeo/aty232.
- [24] Cook, A., Colaprete, A., Mauro, D., Stupl, J., Nguyen, A., Kahre, M., Haberle, R., Perez, A. D., Uribe, E., Bonner, K., et al., “Aeolus: A Mission to Observe the Thermal and Wind Environment of Mars,” *Planetary Science Vision 2050 Workshop*, Vol. 1989, LPI Contributions, 2017, pp. 1–2.
- [25] Wood, J. A., Boynton, W. V., Buck, W. R., Ferris, J. P., Hayes, J. M., Meech, K. J., Mustard, J. F., Nagy, A. F., Noll, K. S., Paige, D. A., Pappalardo, R. T., Reysenbach, A.-L., Schopf, J. W., and Sprague, A. L., *Assessment of Mars science and mission priorities*, Space Studies Board, National Research Council, National Academies Press, Washington D.C, 2003. ISBN: 978-0309089173.
- [26] Topputo, F., Massari, M., Biggs, J., Di Lizia, P., Dei Tos, D., Mani, K., Ceccherini, S., Franzese, V., Cervone, A., Sundaramoorthy, P., et al., “LUMIO: Characterizing Lunar Meteoroid Impacts with a CubeSat,” *69th International Astronautical Congress (IAC 2018)*, Oct 2018, pp. 1–11.
- [27] Sutton, G. P., and Biblarz, O., *Rocket propulsion elements*, 7th ed., John Wiley & Sons, New York, 2010, Chaps. 3, 9, pp. 5–9 & 55–68 & 90–92 & 282–284 & 342. ISBN: 978-0471326427.
- [28] Mani, K. V., Cervone, A., and Topputo, F., “Combined Chemical–Electric Propulsion for a Stand-Alone Mars CubeSat,” *Journal of Spacecraft and Rockets*, 2019, pp. 1–15. doi:10.2514/1.A34519, URL <https://arc.aiaa.org/doi/full/10.2514/1.A34519>.
- [29] Mani, K., Topputo, F., and Cervone, A., “Dual Chemical-Electric Propulsion Systems Design for Interplanetary CubeSats,” *6th Space Propulsion Conference*, 2018, pp. 1–12.
- [30] Mani, K., Topputo, F., Cervone, A., et al., “Chemical Propulsion System Design for a 16U Interplanetary CubeSat,” *69th International Astronautical Congress, Bremen, Germany*, 2018, pp. 1–15.
- [31] Tummala, A. R., and Dutta, A., “An Overview of Cube-Satellite Propulsion Technologies and Trends,” *MDPI Aerospace Journal*, Vol. 4, No. 4, 2017, p. 58. doi:10.3390/aerospace4040058.
- [32] Yost, B., “State of the art of small spacecraft technology,” Tech. Rep. NASA/TP—2018–220027, National Aeronautics and Space Administration: Ames Research Center, Moffett Field, California, Dec 2018.
- [33] Rovey, J., Lyne, C. T., Mundahl, A. J., Rasmont, N., Glascock, M. S., Wainwright, M. J., and Berg, S. P., “Review of Chemical-Electric Multimode Space Propulsion,” *AIAA Propulsion and Energy 2019 Forum*, 2019, p. 4169.

- [34] Gibbon, D., “Review of the use of butane as a low cost propellant,” *2nd Space Propulsion Conference, San Sebastian, Spain*, May 2010, p. 11.
- [35] *JPL MarCO - Micro CubeSat Propulsion System*, VACCO, 2012. URL https://www.vacco.com/images/uploads/pdfs/JPL_MarCO_-_Micro_CubeSat_Propulsion_System_datasheet.pdf, Last accessed: 10-Oct-2019.
- [36] Hinkley, D., “A novel cold gas propulsion system for nanosatellites and picosatellites,” *22nd Annual AIAA/USU Conference on Small Satellites, Logan, Utah, United States*, Aug 2008, pp. SSC08–VII–7.
- [37] *Marotta Cold Gas Thruster*, Marotta Controls Inc., 2015. URL <http://marotta.com/wp-content/uploads/2015/12/CGMT-Tech-Briefs-Article.pdf>, Last accessed: 10-Oct-2019.
- [38] *Monopropellant Thrusters*, Moog Inc., 2018. URL https://www.moog.com/content/dam/moog/literature/Space_Defense/spaceliterature/propulsion/Moog-MonopropellantThrusters-Datasheet.pdf, Last accessed: 10-Oct-2019.
- [39] Knauber, R., “Thrust misalignments of fixed-nozzle solid rocket motors,” *Journal of spacecraft and rockets*, Vol. 33, No. 6, 1996, pp. 794–799. doi:10.2514/6.1995-2873.
- [40] Zondervan, K., Fuller, J., Rowen, D., Hardy, B., Kobel, C., Chen, S.-H., Morrison, P., Smith, T., and Kremer, A., “CubeSat solid rocket motor propulsion systems providing delta-Vs greater than 500 m/s,” *28th Annual AIAA/USU Conference on Small Satellites, Logan, Utah, United States*, Aug 2014, pp. SSC14–X–1.
- [41] Unnikrishnan, K., Pandureng, L., and Krishnamurthy, V., “The effect of vacuum and radiation on solid propellant properties,” *Propellants, Explosives, Pyrotechnics*, Vol. 6, No. 5, 1981, pp. 121–125. doi:10.1002/prop.19810060502.
- [42] Sathiyathan, K., Lee, R., Chesser, H., Dubois, C., Stowe, R., Farinaccio, R., and Ringuette, S., “Solid propellant microthruster design for nanosatellite applications,” *Journal of Propulsion and Power*, Vol. 27, No. 6, 2011, pp. 1288–1294. doi:10.2514/1.b34109.
- [43] Rossi, C., Larangot, B., Pham, P.-Q., Briand, D., de Rooij, N. F., Puig-Vidal, M., and Samitier, J., “Solid propellant microthrusters on silicon: design, modeling, fabrication, and testing,” *Journal of microelectromechanical systems*, Vol. 15, No. 6, 2006, pp. 1805–1815. doi:10.1109/jmems.2006.880232.
- [44] Chaalane, A., Chemam, R., Houabes, M., Yahiaoui, R., Metatla, A., Ouari, B., Metatla, N., Mahi, D., Dkhissi, A., and Esteve, D., “A MEMS-based solid propellant microthruster array for space and military applications,” *Journal of Physics: Conference Series*, Vol. 660, IOP Publishing, 2015, p. 012137.
- [45] *STAR 4G and STAR 5A*, Northrop Grumman Innovation Systems, 2016. URL https://www.northropgrumman.com/Capabilities/PropulsionSystems/Documents/NGIS_MotorCatalog.pdf, Last accessed: 10-Oct-2019.

- [46] *CAPS-3*, Digital Solid State Propulsion, 2016. URL <https://static1.squarespace.com/static/59de9c9c18b27ddf3bac610a/t/5a3a9c5d9140b78b7a1768e9/1513790563886/Brochure+Inlet+CAPS+3+Website.pdf>, Last accessed: 10-Oct-2019.
- [47] Wurdak, M., Strauss, F., Werling, L., Ciezki, H. K., Greuel, D., Lechler, R., Wingborg, N., Hasan, D., and Scharlemann, C., “Determination of fluid properties of the green propellant FLP-106 and related material and component testing with regard to applications in space missions,” *3rd Space Propulsion Conference, Bordeaux, France*, May 2012, pp. 1–8.
- [48] Sackheim, R. L., and Masse, R. K., “Green propulsion advancement: Challenging the maturity of monopropellant hydrazine,” *Journal of Propulsion and Power*, Vol. 30, No. 2, 2014, pp. 265–276. doi:10.2514/6.2013-3988.
- [49] Gohardani, A. S., Stanojev, J., Demairé, A., Anflo, K., Persson, M., Wingborg, N., and Nilsson, C., “Green space propulsion: Opportunities and prospects,” *Progress in Aerospace Sciences*, Vol. 71, Nov 2014, pp. 128–149. doi:10.1016/j.paerosci.2014.08.001.
- [50] Schmuland, D., Masse, R., and Sota, C., “Hydrazine propulsion module for CubeSats,” *25th Annual AIAA/USU Conference on Small Satellites, Logan, Utah, United States*, 2011, pp. SSC11–X–4.
- [51] Scharlemann, C., Schiebl, M., Amsüss, R., Tajmar, M., Miotti, P., Kappenstein, C., Batonneau, Y., Brahmi, R., and Hunter, C., “Monopropellant thruster development: investigation of decomposition efficiencies,” *3rd International Conference on Green Propellants for Space Propulsion, Poitiers, France*, 2006, pp. 1–10.
- [52] Scharlemann, C., and Tajmar, M., “Development of Propulsion Means for Microsatellites,” *43rd AIAA /ASME/SAE/ASEE Joint Propulsion Conference & Exhibit*, July 2007, p. 5184.
- [53] Anflo, K., and Crowe, B., “In-space demonstration of an ADN-based propulsion system,” *47th AIAA /ASME/SAE/ASEE Joint Propulsion Conference & Exhibit*, July 2011, p. 5832.
- [54] Negri, M., Wilhelm, M., Hendrich, C., Wingborg, N., Gediminas, L., Adelöw, L., Maleix, C., Chabernaud, P., Brahmi, R., Beauchet, R., et al., “New technologies for ammonium dinitramide based monopropellant thrusters—The project RHEFORM,” *Acta Astronautica*, Vol. 143, Feb 2018, pp. 105–117. doi:10.1016/j.actaastro.2017.11.016.
- [55] McLean, C. H., “Green propellant infusion mission program overview,” *49th AIAA/ASME/SAE/ASEE Joint Propulsion Conference, San Jose, United States*, July 2013, p. 3847.
- [56] Werling, L. K., Haßler, M., Lauck, F., Ciezki, H. K., and Schlechtriem, S., “Experimental Performance Analysis (c^* & c^* Efficiency) of a Premixed Green Propellant consisting of N_2O and C_2H_4 ,” *53rd AIAA/SAE/ASEE Joint Propulsion Conference, Atlanta, Georgia, United States*, July 2017, p. 5069.

- [57] Spores, R. A., “GPIM AF-M315E Propulsion System,” *51st AIAA/SAE/ASEE Joint Propulsion Conference, Orlando, Florida, United States*, American Institute of Aeronautics and Astronautics, July 2015, p. 3573.
- [58] Masse, R., Allen, M., Spores, R., and Driscoll, E. A., “AF-M315E propulsion system advances and improvements,” *52nd AIAA/SAE/ASEE Joint Propulsion Conference, Salt Lake City, Utah, United States*, July 2016, p. 4577.
- [59] Masse, R. K., Carpenter, C. B., Schmuland, D. T., Overly, J., and Allen, M. Y., “CubeSat High-Impulse Adaptable Modular Propulsion System (CHAMPS) Product Line Development Status and Mission Applications,” *49th AIAA/ASME/SAE/ASEE Joint Propulsion Conference, San Jose, California, United States*, AIAA, July 2013, p. 3760.
- [60] *1N HPGP Thruster*, Bradford ECAPS, 2017. URL http://ecaps.space/assets/pdf/Bradford_ECAPS_Folder_2017.pdf, Last accessed: 10-Oct-2019.
- [61] *BGT-X5*, Busek Company Inc., 2016. URL http://busek.com/index_htm_files/70008517E.pdf, Last accessed: 10-Oct-2019.
- [62] Wertz, J. R., Everett, D. F., and Puschell, J. J., *Space mission engineering: the new SMAD*, Microcosm Press, Hawthorne, California, 2011, Chap. 18, pp. 545–546. ISBN: 978-1881883159.
- [63] Asakura, T., Hayashi, S., Yano, Y., and Kakami, A., “Influence of Injector for Performance of N₂O/DME Bipropellant Thruster,” *Transactions of the Japan Society for Aeronautical and Space Sciences, Aerospace Technology Japan*, Vol. 16, No. 2, 2018, pp. 177–180. doi:10.2322/tastj.16.177.
- [64] Marcu, B., Prueger, G., Epstein, A., and Jacobson, S., “The commoditization of space propulsion: Modular propulsion based on mems technology,” *41st AIAA/ASME/SAE/ASEE Joint Propulsion Conference & Exhibit, Tucson, Arizona, United States*, July 2005, p. 3650.
- [65] Woschnak, A., Krejci, D., Schiebl, M., and Scharlemann, C., “Development of a green bipropellant hydrogen peroxide thruster for attitude control on satellites,” *Progress in Propulsion Physics*, Vol. 4, 2013, pp. 689–706. doi:10.1051/eucass/201304689.
- [66] *HYDROS*, Tethers Unlimited, 2019. URL <http://www.tethers.com/wp-content/uploads/2019/09/2019-HYDROS.pdf>, Last accessed: 10-Oct-2019.
- [67] ESA-ESTEC, “CDF Study Report of Lunar Meteoroid Impacts Observer (LUMIO) Mission,” Tech. Rep. LUMIO-CDF-R-36, European Space Agency, Noordwijk, the Netherlands, May 2018.
- [68] Hegel, D., “Flexcore: Low-cost attitude determination and control enabling high-performance small spacecraft,” *30th Annual AIAA/USU Conference on Small Satellites, Logan, Utah, United States*, Aug 2016, pp. 1–8.
- [69] World Health Organization, “Hydrazine: health and safety guide,” *Health and safety guide. Companion volume to: Environmental health criteria*, Vol. 68, No. 56, 1991, pp. 1–29.

- [70] Negri, M., “Replacement of hydrazine: overview and first results of the H2020 project Rheform,” *6th European Conference for Aeronautics and Space Sciences (EUCASS)*, Krakow, Poland, June 2015, pp. 29–06.
- [71] Gordon, S., and McBride, B. J., “Computer program for calculation of complex chemical equilibrium compositions and applications. Part 1: Analysis,” Tech. Rep. NASA-RP-1311, National Aeronautics and Space Administration. Glenn Research Center, Cleveland, Oct 1994.
- [72] *AF-M315E Safety Data Sheet*, Digital Solid State Propulsion, 2019. URL https://static1.squarespace.com/static/59de9c9c18b27ddf3bac610a/t/5b915dbb88251bc75257c55f/1536253374030/AF-M315E+SDS+2013_Rev+3.pdf, Last accessed: 10-Oct-2019.
- [73] Wilhelm, M., Negri, M., Ciezki, H., and Schlechtriem, S., “Preliminary tests on thermal ignition of ADN-based liquid monopropellants,” *Acta Astronautica*, Vol. 158, May 2018, pp. 388–396. doi:10.1016/j.actaastro.2018.05.057.
- [74] Negri, M., Wilhelm, M., Hendrich, C., Wingborg, N., Gediminas, L., Adelöw, L., Koopmans, R.-J., Schuh, S., Bartok, T., Scharlemann, C., et al., “Technology development for ADN-based green monopropellant thrusters—an overview of the Rheform project,” *7th European Conference for Aeronautics and Space Sciences (EUCASS)*, Milan, Italy, July 2017, pp. 1–13.
- [75] Vatani, A., Mehrpooya, M., and Gharagheizi, F., “Prediction of Standard Enthalpy of Formation by a QSPR Model,” *International Journal of Molecular Sciences*, Vol. 8, No. 5, 2007, pp. 407–432. doi:10.3390/i8050407.
- [76] Kon’kova, T. S., Matyushin, Y. N., Miroshnichenko, E. A., and Vorob’ev, A. B., “Thermochemical properties of dinitramidic acid salts,” *Russian Chemical Bulletin*, Vol. 58, No. 10, 2009, pp. 2020–2027. doi:10.1007/s11172-009-0276-z.
- [77] Rumble, J., *CRC Handbook of Chemistry and Physics*, 99th ed., CRC Press, Boca Raton, Florida, 2018. ISBN: 978-1439880494.
- [78] Wingborg, N., Larsson, A., Elfsberg, M., and Appelgren, P., “Characterization and ignition of ADN-based liquid monopropellants,” *41st AIAA /ASME/SAE/ASEE Joint Propulsion Conference & Exhibit*, Tucson, Arizona, United States, July 2005, p. 4468.
- [79] Huzel, D. K., *Modern engineering for design of liquid-propellant rocket engines*, AIAA, 1992, Vol. 147, Chap. 8, pp. 289–304. ISBN: 978-1563470134.
- [80] Jens, E., Karp, A. C., Nakazono, B., Eldred, D. B., DeVost, M. E., and Vaughan, D., “Design of a Hybrid CubeSat Orbit Insertion Motor,” *52nd AIAA/SAE/ASEE Joint Propulsion Conference*, Salt Lake City, Utah, United States, July 2016, p. 4961.
- [81] *RNH 64-1 Technical Data Sheet*, Eagle Picher Technologies, Feb 2003. URL https://www.datasheetarchive.com/companies/eaglepicher_com.html, Last Accessed: 30-March-2019.
- [82] Welsch, G., Boyer, R., and Collings, E., *Materials properties handbook: titanium alloys*, ASM international, 1993. ISBN: 978-0871704818.

- [83] Sato, E., Sawai, S., Uesugi, K., Takami, T., Furukawa, K., Kamada, M., and Kondo, M., "Superplastic Titanium Tanks for Propulsion System of Satellites," *Superplasticity in Advanced Materials*, Vol. 551-552, Trans Tech Publications, July 2007, pp. 43–48. doi:10.4028/www.scientific.net/msf.551-552.43.
- [84] Mani, K., Boccelli, S., Topputo, F., Cervone, A., et al., "Electric Propulsion Characterization for a Stand-Alone Mars CubeSat," *36th International Electric Propulsion Conference, Vienna, Austria*, 2019, pp. 1–15.
- [85] Choueiri, E. Y., "A critical history of electric propulsion: The first 50 years (1906-1956)," *Journal of Propulsion and Power*, Vol. 20, No. 2, 2004, pp. 193–203. doi:10.2514/1.9245.
- [86] Dobbins, T. O., "Thermodynamics of rocket propulsion and theoretical evaluation of some prototype propellant combinations," Tech. rep., Aeronautical Systems DIV Wright Field OH, 1959.
- [87] Jahn, R. G., *Physics of electric propulsion*, Courier Corporation, 2006. ISBN: 978-0-486-45040-7.
- [88] Goebel, D. M., and Katz, I., *Fundamentals of electric propulsion: ion and Hall thrusters*, John Wiley & Sons, New York, 2008, Vol. 1, Chaps. 4,6, pp. 148,251–255. ISBN: 978-047-04364-48.
- [89] Martinez-Sanchez, M., and Pollard, J. E., "Spacecraft electric propulsion-an overview," *Journal of Propulsion and Power*, Vol. 14, No. 5, 1998, pp. 688–699. doi:10.2514/2.5331.
- [90] Turner, M. J., *Rocket and spacecraft propulsion: principles, practice and new developments*, Springer Science & Business Media, 2008. ISBN: 978-354-06920-27.
- [91] Tajmar, M., Genovese, A., and Steiger, W., "Indium field emission electric propulsion microthruster experimental characterization," *Journal of Propulsion and Power*, Vol. 20, No. 2, 2004, pp. 211–218. doi:10.2514/1.9247.
- [92] Gamero-Castano, M., and Hruby, V., "Electrospray as a source of nanoparticles for efficient colloid thrusters," *Journal of Propulsion and Power*, Vol. 17, No. 5, 2001, pp. 977–987. doi:10.2514/2.5858.
- [93] Hill, P. G., and Peterson, C. R., *Mechanics and thermodynamics of propulsion*, Addison-Wesley Publishing Co., Reading, Massachusetts, United States, 1992. ISBN: 978-020-11465-92.
- [94] Mazouffre, S., "Electric propulsion for satellites and spacecraft: established technologies and novel approaches," *Plasma Sources Science and Technology*, Vol. 25, No. 3, 2016, p. 033002. doi:10.1088/0963-0252/25/3/033002.
- [95] Samples, S., Li, G. Z., and Wirz, R. E., "Performance Testing and Development of the MiXI Thruster with the ARCH Discharge," *2018 Joint Propulsion Conference, Cincinnati, Ohio, United States*, July 2018, p. 4648.
- [96] Wirz, R. E., "Discharge plasma processes of ring-cusp ion thrusters," Ph.D. thesis, California Institute of Technology, 2005.

- [97] Leiter, H., Berger, M., and Rath, M., “Evolution of the Airbus DS GmbH Radio Frequency Ion Thruster Family,” *Joint Conference of 30th ISTS, 34th IEPC and 6th NSAT, Kobe-Hyogo, Japan*, 2015, pp. IEPC–2015–90 / ISTS–2015–b–90.
- [98] *BIT-3*, Busek Company Inc., 2019. URL http://busek.com/index_htm_files/70010819F.pdf, Last accessed: 10-Oct-2019.
- [99] Martinez Martinez, J., Rafalskyi, D., and Aanesland, A., “Development and Testing of the NPT30-I2 Iodine Ion Thruster,” *36th International Electric Propulsion Conference, Vienna, Austria*, 2019, pp. IEPC–2019–811.
- [100] Wirz, R., “Miniature ion thrusters: A review of modern technologies and mission capabilities,” *Joint Conference of 30th ISTS, 34th IEPC and 6th NSAT*, Univ. of California Los Angeles, CA, 2015, pp. IEPC–2015–275 / ISTS–2015–b–275.
- [101] *NPT30*, ThrustMe, 2019. URL <https://satsearch.co/products/thrustme-npt30>, Last accessed: 10-Oct-2019.
- [102] Wright, W., and Ferrer, P., “Electric micropropulsion systems,” *Progress in Aerospace Sciences*, Vol. 74, 2015, pp. 48–61. doi:10.1016/j.paerosci.2014.10.003.
- [103] Grishin, S., and Leskov, L., “Electrical Rocket Engines of Space Vehicles,” *Mashinostroenie, Moscow*, 1989.
- [104] Khayms, V., and Martinez-Sanchez, M., “Fifty-watt Hall thruster for microsattellites,” *Micropropulsion for small spacecraft*, 2000, p. 233.
- [105] Szabo, J. J., Tedrake, R., Metivier, E., Paintal, S., and Taillefer, Z., “Characterization of a one hundred Watt, long lifetime Hall effect thruster for small spacecraft,” *53rd AIAA/SAE/ASEE Joint Propulsion Conference, Atlanta, Georgia, United States*, July 2017, p. 4728.
- [106] Szabo, J., Pote, B., Paintal, S., Robin, M., Hillier, A., Branam, R. D., and Huffmann, R. E., “Performance evaluation of an iodine-vapor Hall thruster,” *Journal of Propulsion and Power*, Vol. 28, No. 4, 2012, pp. 848–857. doi:10.2514/6.2011-5891.
- [107] Polzin, K. A., Markusic, T. E., Stanojev, B. J., Dehoyos, A., Raiteses, Y., Smirnov, A., and Fisch, N. J., “Performance of a low-power cylindrical Hall thruster,” *Journal of propulsion and power*, Vol. 23, No. 4, 2007, pp. 886–888. doi:10.2514/1.28595.
- [108] Misuri, T., Albertoni, R., Ducci, C., Waldvogel, B., Appel, L., Eytan, R., Lev, D., Dannenmayer, K., and Di Cara, D., “MEPS: A low power electric propulsion system for small satellites,” *10th IAA Symposium on Small Satellites for Earth Observation, Berlin, Germany*, Apr 2015, pp. 20–24.
- [109] Capacci, M., Matticari, G., Materassi, M., and Noci, G., “Development and qualification of a neutralizer device for the FEPP micro propulsion on microscope and Lisa Path Finder,” *30th International Electric propulsion Conference, Florence, Italy*, Vol. 154, Sep 2007, pp. IEPC–2007–154.

- [110] Marcuccio, S., Genovese, A., and Andrenucci, M., “Experimental performance of field emission microthrusters,” *Journal of Propulsion and Power*, Vol. 14, No. 5, 1998, pp. 774–781. doi:10.2514/2.5340.
- [111] Taylor, G. I., “Disintegration of water drops in an electric field,” *Royal Society of London. Series A. Mathematical and Physical Sciences*, Vol. 280, No. 1382, 1964, pp. 383–397. doi:10.1098/rspa.1964.0151.
- [112] Vasiljevich, I., Tajmar, M., Grienauer, W., Plesescu, F., Buldrini, N., Gonzalez del Amo, J., Carnicero Domunguez, B., and Betto, M., “Development of an indium mN-FEEP thruster,” *44th AIAA /ASME/SAE/ASEE Joint Propulsion Conference & Exhibit, Hartford, Connecticut, United States*, July 2008, p. 4534.
- [113] Reissner, A., “Lifetime testing of the mN-FEEP thruster,” *52nd AIAA/SAE/ASEE Joint Propulsion Conference, Salt Lake City, Utah, United States*, July 2016, p. 5045.
- [114] Schönherr, T., Little, B., Krejci, D., Reissner, A., and Seifert, B., “Development, Production, and Testing of the IFM Nano FEEP Thruster,” *36th International Electric Propulsion Conference, Vienna, Austria*, 2019, pp. IEPC–2019–362.
- [115] Krejci, D., Reissner, A., Seifert, B., Jelem, D., Hörbe, T., Plesescu, F., Friedhoff, P., and Lai, S., “Demonstration of the IFM Nano Feep Thruster in Low Earth Orbit,” *The 4S Symposium, Sorrento, Italy*, June 2018, pp. 1–12.
- [116] Ceruti, L., Antimiani, A., and Polli, A., “Power control unit for μ N FEEP propulsion subsystem,” *30th International Electric Propulsion Conference, Florence, Italy*, 2007, pp. IEPC–2007–283.
- [117] Reissner, A., Buldrini, N., Seifert, B., Plesescu, F., Scharlemann, C., del Amo, J. G., and Massotti, L., “Detailed Performance Characterization of the mN-FEEP Thruster,” *4th Space Propulsion Conference, Cologne, Germany*, May 2014, pp. 1–14.
- [118] Krejci, D., Hugonnaud, V., Schönherr, T., Little, B., Reissner, A., Seifert, B., Koch, Q., Bosch Borrás, E., and Gonzalez del Amo, J., “Full Performance Mapping of the IFM Nano Thruster, Including Direct Thrust Measurements,” *Journal of Small Satellites*, Vol. 8, No. 2, 2019, pp. 881–893.
- [119] Marcuccio, S., Paita, L., Saviozzi, M., and Andrenucci, M., “Flight demonstration of FEEP on get away special,” *34th AIAA/ASME/SAE/ASEE Joint Propulsion Conference and Exhibit*, 1998, p. 3332.
- [120] *IFM Nano Thruster*, Enpulsion, 2019. URL <https://www.enpulsion.com/wp-content/uploads/ENP2018-001.F-IFM-Nano-Thruster-Product-Overview.pdf>, Last accessed: 10-Oct-2019.
- [121] Kisasi, S., Muraoka, R., Huanjun, C., Tanaka, M., Tahara, H., and Wakizono, T., “Research and Development of Osaka Institute of Technology PROITERES Nano-Satellite Series with Electrothermal Pulsed Plasma Thruster systems,” *29th International Symposium on Space Technology and Science, Nagoya-Aichi, Japan*, 2013, pp. ISTS–2013–b–15.

- [122] Pottinger, S., and Scharlemann, C., “Micro pulsed plasma thruster development,” *30th International Electric Propulsion Conference, Florence, Italy*, 2007, pp. IEPC–2007–125.
- [123] Antropov, N., Bogaty, A., Dyakonov, G., Lyubinskaya, N., Popov, G., Semenikhin, S., Tyutin, V., Khrustalev, M., and Yakovlev, V., “A new stage in the development of ablative pulsed plasma thrusters at the RIAME,” *Solar System Research*, Vol. 46, No. 7, 2012, pp. 531–541. doi:10.1134/s0038094612070064.
- [124] Ciaralli, S., Coletti, M., and Gabriel, S., “Results of the qualification test campaign of a Pulsed Plasma Thruster for Cubesat Propulsion (PPTCUP),” *Acta Astronautica*, Vol. 121, 2016, pp. 314–322. doi:10.1016/j.actaastro.2015.08.016.
- [125] *Bmp-220 PPT*, Busek Company Inc, 2019. URL http://busek.com/index_html_files/70008502F.pdf, Last accessed: 10-Oct-2019.
- [126] West, M. D., Charles, C., Boswell, R. W., et al., “Testing a helicon double layer thruster immersed in a space-simulation chamber,” *Journal of Propulsion and Power*, Vol. 24, No. 1, 2008, p. 134. doi:10.2514/1.31414.
- [127] Charles, C., Boswell, R., Alexander, P., Costa, C., Sutherland, O., Pfitzner, L., Franzen, R., Kingwell, J., Parfitt, A., Frigot, P.-E., et al., “Helicon double layer thrusters,” *42nd AIAA /ASME/SAE/ASEE Joint Propulsion Conference & Exhibit, Sacramento, California, United States*, July 2006, p. 4838.
- [128] Ahedo, E., “Plasma dynamics in a helicon thruster,” *Progress in Propulsion Physics*, Vol. 4, EDP Sciences, Mar 2013, pp. 337–354.
- [129] Pavarin, D., Ferri, F., Manente, M., Curreli, D., Guclu, Y., Melazzi, D., Rondini, D., Suman, S., Carlsson, J., Bramanti, C., et al., “Design of 50 W helicon plasma thruster,” *31st International Electric Propulsion Conference, Ann Arbor, Michigan, United States*, 2009, pp. IEPC–2009–205.
- [130] Ahedo, E., “Plasmas for space propulsion,” *Plasma Physics and Controlled Fusion*, Vol. 53, No. 12, 2011, p. 124037. doi:10.1088/0741-3335/53/12/124037.
- [131] Ahedo, E., “Parametric analysis of a magnetized cylindrical plasma,” *Physics of Plasmas*, Vol. 16, No. 11, 2009, p. 113503. doi:10.1063/1.3262529.
- [132] Ahedo, E., “Cylindrical model of a helicon-generated plasma,” *31st International Electric Propulsion Conference, Ann Arbor, Michigan, United States*, Vol. 193, 2009, pp. IEPC–2009–193.
- [133] Lafleur, T., “Helicon plasma thruster discharge model,” *Physics of Plasmas*, Vol. 21, No. 4, 2014, p. 043507. doi:10.1063/1.4871727.
- [134] Ahedo, E., and Merino, M., “On plasma detachment in propulsive magnetic nozzles,” *Physics of Plasmas*, Vol. 18, No. 5, 2011, p. 053504. doi:10.1063/1.3589268.
- [135] Ahedo, E., and Navarro-Cavallé, J., “Helicon thruster plasma modeling: Two-dimensional fluid-dynamics and propulsive performances,” *Physics of Plasmas*, Vol. 20, No. 4, 2013, p. 043512. doi:10.1063/1.4798409.

- [136] Ahedo, E., and Sánchez, M. M., “Theory of a stationary current-free double layer in a collisionless plasma,” *Physical review letters*, Vol. 103, No. 13, 2009, p. 135002. doi: 10.1103/physrevlett.103.135002.
- [137] Lieberman, M. A., and Lichtenberg, A. J., *Principles of plasma discharges and materials processing*, John Wiley & Sons, 2005.
- [138] Navarro-Cavallé, J., Ahedo, E., Merino, M., Gómez, V., Ruiz, M., and del Amo, J. A. G., “Helicon Plasma Thrusters: prototypes and advances on modeling,” *33rd International Electric Propulsion Conference. Washington, D.C.*, 2013, pp. IEPC–2013–285.
- [139] Pottinger, S., Lappas, V., Charles, C., and Boswell, R., “Performance characterization of a helicon double layer thruster using direct thrust measurements,” *Journal of Physics D: Applied Physics*, Vol. 44, No. 23, 2011, p. 235201. doi:10.1088/0022-3727/44/23/235201.
- [140] Manente, M., Trezzolani, F., Magarotto, M., Fantino, E., Selmo, A., Bellomo, N., Toson, E., and Pavarin, D., “REGULUS: A propulsion platform to boost small satellite missions,” *Acta Astronautica*, Vol. 157, 2019, pp. 241–249. doi:10.1016/j.actaastro.2018.12.022.
- [141] *REGULUS*, Technology for Propulsion and Innovation - T4i, 2019. URL http://www.t4innovation.com/wp-content/uploads/2018/09/20180903_00_00_REGULUS_datasheet_WEB.pdf, Last accessed: 10-Oct-2019.
- [142] Tsay, M., Frongillo, J., and Zwahlen, J., “Maturation of iodine fueled BIT-3 RF ion thruster and RF neutralizer,” *52nd AIAA/SAE/ASEE Joint Propulsion Conference, Salt Lake City, Utah, United States*, July 2016, p. 4544.
- [143] Tsay, M., Frongillo III, J. J., Model, J., and Zwahlen, J., “Iodine propellant rf ion thruster with rf cathode,” , 2018. US Patent App. 15/425,317.
- [144] Branam, R. D., “Iodine Plasma (Electric Propulsion) Interaction with Spacecraft Materials,” Tech. Rep. AFRL-AFOSR-VA-TR-2016-0381, The University of Alabama Tuscaloosa & Air Force Research Laboratory, United States, Dec 2016.
- [145] Polzin, K. A., Peeples, S. R., Seixal, J. F., Mauro, S. L., Lewis, B. L., Jerman, G. A., Calvert, D. H., Dankanich, J., Kamhawi, H., Hickman, T. A., et al., “Propulsion system development for the iodine satellite (iSAT) demonstration mission,” *Joint Conference 30th ISSTS, 34th IEPC and 6th Nanosatellite Symposium, Kobe, Japan*, July 2015, pp. 1–14.
- [146] Bassner, H., Killinger, R., Leiter, H., and Mueller, J., “Advantages and applications of the RF-ion thrusters RIT,” *37th Joint Propulsion Conference and Exhibit*, 2001, p. 3494.
- [147] Grondein, P., Lafleur, T., Chabert, P., and Aanesland, A., “Global model of an iodine gridded plasma thruster,” *Physics of Plasmas*, Vol. 23, No. 3, 2016, p. 033514. doi: 10.1063/1.4944882.
- [148] Chabert, P., Arancibia Monreal, J., Bredin, J., Popelier, L., and Aanesland, A., “Global model of a gridded-ion thruster powered by a radiofrequency inductive coil,” *Physics of Plasmas*, Vol. 19, No. 7, 2012, p. 073512. doi:10.1063/1.4737114.

- [149] Lucken, R., Marmuse, F., Tavant, A., Bourdon, A., and Chabert, P., “Global model of a magnetized ion thruster with xenon and iodine,” *36th International Electric Propulsion Conference, Vienna, Austria*, 2019, pp. IEPC–2019–678.
- [150] Pedrini, D., Misuri, T., Paganucci, F., and Andrenucci, M., “Development of hollow cathodes for space electric propulsion at sitael,” *MDPI Aerospace Journal*, Vol. 4, No. 2, 2017, p. 26. doi:10.3390/aerospace4020026.
- [151] Cruz Chambel de Aguiar, G., “Earth–Mars low-thrust transfers with ballistic capture and real-Solar-System dynamics,” Master’s thesis, Delft University of Technology, 2017.
- [152] Aguiar, G., and Topputo, F., “A technique for designing Earth–Mars low-thrust transfers culminating in ballistic capture,” *7th International Conference on Astrodynamics Tools and Techniques (ICATT)*, Oberpfaffenhofen, Germany, Nov 2018, pp. 1–8.
- [153] Topputo, F., and Zhang, C., “Survey of Direct Transcription for Low-Thrust Space Trajectory Optimization with Applications,” *Abstract and Applied Analysis*, Vol. 1, June 2014, pp. 1–15. doi:10.1155/2014/851720.
- [154] Luo, Z.-F., Topputo, F., Bernelli-Zazzera, F., and Tang, G.-J., “Constructing ballistic capture orbits in the real Solar System model,” *Celestial Mechanics and Dynamical Astronomy*, Vol. 120, No. 4, 2014, pp. 433–450. doi:10.1007/s10569-014-9580-5.
- [155] Acton Jr, C. H., “Ancillary data services of NASA’s navigation and ancillary information facility,” *Planetary and Space Science*, Vol. 44, No. 1, 1996, pp. 65–70. doi:10.1016/0032-0633(95)00107-7.
- [156] Soler Lanagrán, F., “Low-Thrust heliocentric transfer with ballistic capture and orbit circularization for a standalone Mars CubeSat,” Master’s thesis, Politecnico di Milano, 2018.
- [157] Petropoulos, A. E., “Refinements to the Q-law for the low-thrust orbit transfers,” *15th AAS/AIAA Space Flight Mechanics Conference, Copper Mountain, Colorado, United States*, Jan 2005, pp. 1–21.
- [158] Holste, K., Gärtner, W., Zschätzsch, D., Scharmann, S., Köhler, P., Dietz, P., and Klar, P. J., “Performance of an iodine-fueled radio-frequency ion-thruster,” *European Physical Journal D*, Vol. 72, No. 1, 2018, p. 9. doi:10.1140/epjd/e2017-80498-5.
- [159] Dressler, R., Chiu, Y.-H., and Levandier, D., “Propellant alternatives for ion and Hall effect thrusters,” *38th AIAA Aerospace Sciences Meeting and Exhibit, Reno, Nevada, United States*, Jan 2000, p. 602.
- [160] Mani, K. V., Casado, A. S., Franzese, V., Cervone, A., and Topputo, F., “Systems Design of MARIO: Stand-alone 16U CubeSat from Earth to Mars,” *70th International Astronautical Congress, Washington D.C.*, Oct 2019, pp. 1–17.
- [161] Hodges, R. E., Chahat, N., Hoppe, D. J., and Vacchione, J. D., “A Deployable High-Gain Antenna Bound for Mars: Developing a new folded-panel reflectarray for the first CubeSat mission to Mars.” *IEEE Antennas and Propagation Magazine*, Vol. 59, No. 2, 2017, pp. 39–49. doi:10.1109/map.2017.2655561.

- [162] Hodges, R., Lewis, D., Radway, M., Toorian, A., Aguirre, F., Hoppe, D., Shah, B., Gray, A., Rowen, D. W., Welle, R. P., et al., “The ISARA Mission–Flight Demonstration of a High Gain Ka-Band Antenna for 100Mbps Telecom,” *32nd Annual AIAA/USU Conference on Small Satellites, Logan, Utah, United States*, 2018, pp. SSC18–VI–03.
- [163] Mereta, A., and Izzo, D., “Target selection for a small low-thrust mission to near-Earth asteroids,” *Astrodynamics*, Vol. 2, No. 3, 2018, pp. 249–263. doi:10.1007/s42064-018-0024-y.
- [164] Cecen, A., “Calculation, utilization, and inference of spatial statistics in practical spatio-temporal data,” Ph.D. thesis, Georgia Institute of Technology, 2017.
- [165] Agrawal, A., Deshpande, P. D., Cecen, A., Basavarsu, G. P., Choudhary, A. N., and Kalidindi, S. R., “Exploration of data science techniques to predict fatigue strength of steel from composition and processing parameters,” *Integrating Materials and Manufacturing Innovation*, Vol. 3, No. 1, 2014, p. 8. doi:10.1186/2193-9772-3-8.